

# Theoretical and Experimental Satellite Channel Characterisation

Alexios Costouri

Submitted for the degree of Doctor of Philosophy

Heriot-Watt University

EPS/ISSS

February 2020

The copyright in this thesis is owned by the author. Any quotation from the thesis or use of any of the information contained in it must acknowledge this thesis as the source of the quotation or information.



## **Abstract**

The proliferation of very high throughput satellite systems offering Terabit/s of system capacities, puts a large strain on the gateway feeder link requirements. This is leading to the exploitation and use of communication link systems using higher frequencies for data transmission, as it offers a larger bandwidth than the traditional Ka-band channels. Even with the exploitation of the Q/V-band (40/50 GHz), the number of required gateways may be such that the cost of the ground segment exceeds the cost of the satellite. The use of W-band (70/80 GHz) as an additional feeder link frequency band in future very high throughput satellite systems could significantly reduce the cost of the ground segment. This would also offer an opportunity for the user links to migrate to higher frequencies, improving their capacity and helping into decongesting the current occupied channels. Atmospheric impairments, including sky noise, play a major role towards the design of future satellite systems and their mitigation techniques as higher bands magnify these impairments.

Within this thesis, an overview of the current communication satellite systems, propagation campaign heritage and current atmospheric impairment models is shown. Furthermore, the design and development of a geostationary beacon payload for propagation measurements premiering W-band is shown. Ground receivers are also significant towards the collection of propagation measurements. The design, development and implementation of such a receiver at Ka-band is shown. Moreover, beacon measurements at Ka- and Q-band using the Aldo Paraboni payload are processed to reflect excess and total atmospheric fading respectively. Concurrent recordings of the sky noise enable radiometric measurements from the implemented receiver terminals, which can enable sky monitoring. Calibration of the noise channel at Q-band and validation of the fading with that from a beacon power measurement is also shown.

# **Dedication**

*To all my loved ones...*

# Acknowledgments

I would firstly like to express my genuine gratitude towards my supervisor George Goussetis for his support these past few years. I am especially thankful for giving me the opportunity to grow my skills, knowledge and expertise on the field. There have been some difficult times but, his professional approach and mindset has always inspired me to push through. I will forever remember the quote he once told me in the beginning of my journey: “there is no IF I will solve this problem, there is only when”. This has resonated with me and has helped me immensely. Thank you for everything.

The work presented in this thesis has been part of the Heriot-Watt University DTP scholarship which is funded by the Engineering and Physical Sciences Research Council (EPSRC). Therefore, I would like to acknowledge the Heriot-Watt University and the EPSRC for funding me throughout my PhD years.

I would like to thank Savvas Kosmopoulos for sharing his knowledge through the years from a more industrial perspective and the help throughout the ESA project on the development and design of a geostationary payload for propagation measurements. Special thanks to James Nessel and Spiros Ventouras for sharing their knowledge on atmospheric propagation. Also, special thanks to Richard Reeves for his professional input in our work.

I also thank my colleagues in the Microwave Group. They have become my second family in and out of the office as they were always there to support me and listen to my problems. In particular a big shout out to: Rahil Joshi, Victoria Gomez-Guillamon Buendia, Maria Jesus Canavate, Spiros Daskalakis, Constantine Constantinides, Panagiotis Petridis, Jose Garcia Perez, Sadeque Khan, Gergerly Hantos, Salvador Mercader, Adrian Ayastuy, Pascual Hilario, Khaled Aliqab, Christian Alistarh, Simona Sibio, Salvatore Liberto, Romwald Lihakanga, Callum Hodgkinson, Alejandro Baldominos Delgado, Kostas Kossenias, Panagiota Kontou, among others.

Special thanks for their support and wisdom to my dear friends I made in Edinburgh, Theocharis Dionisou, Tasos Zingas, Ben Trevett, Ruben Kruiper, Lucas Kirschbaum,

Alexandros Aristotelous, Kemal Oztoprak, Eva Bergman, Rafael Adorna, Dave Watson, Raf Pollalis, Kostas Anastasakis and all others

Finally and more importantly, I would like to thank my parents, Panicos and Paola, my sister, Stefania and my other half, Chara, for supporting me throughout my journey and always trying to cheer me up.

## Research Thesis Submission

Please note this form should be bound into the submitted thesis.

Name:	Alexios Costouri		
School:	EPS		
Version: (i.e. First, Resubmission, Final)	Final	Degree Sought:	PhD Electrical Engineering

### Declaration

In accordance with the appropriate regulations I hereby submit my thesis and I declare that:

1. The thesis embodies the results of my own work and has been composed by myself
2. Where appropriate, I have made acknowledgement of the work of others
3. The thesis is the correct version for submission and is the same version as any electronic versions submitted\*.
4. My thesis for the award referred to, deposited in the Heriot-Watt University Library, should be made available for loan or photocopying and be available via the Institutional Repository, subject to such conditions as the Librarian may require
5. I understand that as a student of the University I am required to abide by the Regulations of the University and to conform to its discipline.
6. I confirm that the thesis has been verified against plagiarism via an approved plagiarism detection application e.g. Turnitin.

### ONLY for submissions including published works

Please note you are only required to complete the Inclusion of Published Works Form (page 2) if your thesis contains published works)

7. Where the thesis contains published outputs under Regulation 6 (9.1.2) or Regulation 43 (9) these are accompanied by a critical review which accurately describes my contribution to the research and, for multi-author outputs, a signed declaration indicating the contribution of each author (complete)
8. Inclusion of published outputs under Regulation 6 (9.1.2) or Regulation 43 (9) shall not constitute plagiarism.

\* Please note that it is the responsibility of the candidate to ensure that the correct version of the thesis is submitted.

Signature of Candidate:		Date:	12/10/2020
-------------------------	---	-------	------------

### Submission

Submitted By (name in capitals):	ALEXIOS COSTOURI
Signature of Individual Submitting:	
Date Submitted:	12/10/2020

### For Completion in the Student Service Centre (SSC)


Limited Access	Requested	Yes	No	Approved	Yes	No
<i>E-thesis Submitted (mandatory for final theses)</i>						
Received in the SSC by (name in capitals):				Date:		


### Inclusion of Published Works

Please note you are only required to complete the Inclusion of Published Works Form if your thesis contains published works under Regulation 6 (9.1.2)

#### Declaration

This thesis contains one or more multi-author published works. In accordance with Regulation 6 (9.1.2) I hereby declare that the contributions of each author to these publications is as follows:

Citation details	A. Costouri, J. Nessel, and G. Goussetis, "Validation of a Digital Noise Power Integration Technique for Radiometric Clear Sky Attenuation Estimation at Q-Band," <i>Trans. Antennas Propag.</i> , pp. 1–9.
Author 1	Theory, calibration, measurements, validation, writing the article
Author 2	Assistance and guidance through the work
Signature:	
Date:	12/10/2020

Citation details	A. Costouri, G. Goussetis <i>et al.</i> , "European W-Band Propagation Campaign Development," 2018 12 <sup>th</sup> Eur. Conf. Antennas Propagation, EuCAP 2018, pp. 4–7, 2018
Author 1	Design of payload, writing of article
Author 2	Assistance and guidance through the writing
Signature:	
Date:	12/10/2020



# Contents

Chapter 1 .....	1
1 Introduction.....	1
1.1 Communication Satellites and Future Satellite Gateways .....	3
1.2 Propagation Campaign Payload Heritage .....	6
1.3 Atmospheric Propagation Impairments.....	14
1.3.1 Gaseous Attenuation .....	14
1.3.2 Cloud Attenuation.....	15
1.3.3 Rain Attenuation .....	16
1.3.4 Scintillation.....	17
1.3.5 Depolarisation .....	17
1.4 Motivation and Thesis Outline.....	20
1.5 Summary .....	21
References.....	22
Chapter 2.....	28
2 Three-Band Geostationary Satellite Beacon Payload for Propagation Experiments in Europe.....	28
2.1 Introduction .....	28
2.2 Beacon Design Requirements .....	30
2.2.1 Operating Frequencies .....	30
2.2.2 Signal Polarisation .....	31
2.2.3 Coverage Area .....	31
2.2.4 Effective Isotropic Radiated Power (EIRP).....	32
2.2.5 Phase Noise.....	32
2.2.6 Beacon Lifetime.....	33
2.2.7 Mass .....	33

2.2.8	DC Power Consumption .....	33
2.2.9	Telemetry, Tracking and Control (TT&C) Operations.....	33
2.3	Beacon Design.....	33
2.3.1	Up-converter Architecture .....	33
2.3.2	Architecture for Reliability and Redundancy .....	35
2.3.3	Payload Up-conversion Chains.....	36
2.3.4	Ka-band Conversion Chain.....	36
2.3.5	Q-band Conversion Chain.....	40
2.3.6	W-band Conversion Chain.....	43
2.3.7	Simulation Graphs: Output Power, Compression Points and Spectrum.....	44
2.3.8	Gain Stability .....	49
2.3.9	Link Budgets and Margins.....	52
2.3.10	Dual Polarisation.....	55
2.3.11	Phase Noise.....	58
2.3.12	Mass and DC Power Consumption .....	63
2.3.13	TT&C Operations .....	63
2.4	Compliance Matrix.....	64
2.5	Future Work .....	65
2.5.1	Beacon Coverage and Trade-offs.....	65
2.5.2	Availability and Performance of Selected Components .....	66
2.6	Conclusion.....	67
	References.....	69
	Chapter 3.....	71
3	Ground Station for Propagation Measurements at Ka-Band .....	71
3.1	Introduction .....	71
3.2	Beacon Receiver Design .....	72
3.3	Receiver Digital Signal Processing .....	86

3.4	Experimental Results.....	91
3.5	Excess Atmospheric Attenuation .....	95
3.6	Conclusion.....	97
	References.....	98
Chapter 4.....		100
4	Atmospheric Noise and Digital Radiometry at Q-Band .....	100
4.1	Introduction .....	100
4.2	Atmospheric Propagation of an Electromagnetic Wave .....	102
4.2.1	Blackbody and Temperature Relation .....	102
4.2.2	Radiative Transfer Equation .....	104
4.2.3	Description of Signal Attenuation in the Atmosphere.....	107
4.2.4	Noise, Temperature and Signal Absorption.....	110
4.3	Radiometer Calibration .....	114
4.4	SDR Receiver.....	117
4.4.1	System description.....	117
4.4.2	Calibration.....	121
4.5	Experimental Results.....	124
4.6	Discussion and Conclusion .....	131
	References.....	132
Chapter 5.....		136
5	Conclusions and Future Work .....	136
5.1	Thesis Summary and Conclusions .....	136
5.2	Future Work .....	139
	References.....	141

# Table of Figures

Figure 1-1: Potential architecture of a VHTS system .....	2
Figure 1-2: ITALSAT F1 Ka-band payload antenna coverage copied from [41] .....	7
Figure 1-3: ITALSAT F1 Q/V-band payload antenna coverage copied from [41] .....	7
Figure 1-4: ITALSAT F1 Ka-band payload block diagram copied from [41] .....	8
Figure 1-5: ITALSAT F1 Q-band payload block diagram copied from [41] .....	9
Figure 1-6: ITALSAT F1 V-band payload block diagram copied from [41] .....	9
Figure 1-7: OLYMPUS Ka-band payload antenna coverage copied from [48] .....	10
Figure 1-8: OLYMPUS Ku- and Ka-band payload block diagram adapted from [48] .....	10
Figure 1-9: Aldo Paraboni (Alphasat) Ka-band (right) and Q-band (left) payload antenna coverage copied from [51] .....	11
Figure 1-10: Aldo Paraboni (Alphasat) Ka-band and Q-band payload block diagram copied from [51] .....	12
Figure 1-11: Total (blue) and dry air (red) specific gaseous attenuation.....	15
Figure 1-12: Representation of co-polarised and cross-polarised signals. The polarisations can be linear or circular – only linear polarisation is shown for clarity of illustration. ....	18
Figure 2-1: W-band GEO satellite beacon and ground receiver.....	29
Figure 2-2: W-Band coverage when geostationary satellite is at 10° East .....	31
Figure 2-3: Schematic representation of the proposed up-converter. ....	35
Figure 2-4: Schematic representation of the beacon with the two up-converter redundancies and routing to equivalent antennas. ....	36
Figure 2-5 Ka-Band up-conversion chain up to Q-Band power splitter (Single HPA) .....	37
Figure 2-6: Ka-Band driver, ALC coupler and redundancy switch (Single HPA) .....	37
Figure 2-7: Ka-Band Single HPA .....	38
Figure 2-8: Q-Band frequency doubler, filter, driver amplifier and chain branch coupler .....	40
Figure 2-9: Q-Band redundancy switch and single HPA.....	40
Figure 2-10: W-Band up-conversion chain with single HPA.....	43
Figure 2-11: Ka-band Channel Power (Single HPA) .....	45
Figure 2-12: Ka-band Compression Point (Single HPA) .....	45

Figure 2-13: Ka-band Spectrum (Single HPA).....	46
Figure 2-14: Q-band Channel Power (single HPA).....	46
Figure 2-15: Q-band Compression Point (single HPA).....	47
Figure 2-16: Q-band Spectrum (single HPA).....	47
Figure 2-17: W-band channel power (single HPA).....	48
Figure 2-18: W-band compression point (single HPA).....	48
Figure 2-19: W-Band Spectrum (single HPA).....	49
Figure 2-20: ALC Mechanism.....	50
Figure 2-21: Time switched dual polarisation design outline.....	55
Figure 2-22: Polarisation Switch Matrix.....	56
Figure 2-23: Time switched dual polarisation design outline using two HPAs.....	57
Figure 2-24: Dual Frequency Dual Polarisation design outline.....	58
Figure 2-25: PLO-4000 Phase noise envelope copied from [9].....	59
Figure 2-26: LMX2615-SP phase noise at 8.1GHz copied from [11].....	61
Figure 2-27: Spectratime typical phase noise copied from [13].....	62
Figure 3-1: Ka-band front-end block diagram.....	80
Figure 3-2: Alphasat movement as observed from the Chilbolton Observatory.....	82
Figure 3-3: Antenna aluminium base plate.....	82
Figure 3-4: Electrical diagram.....	83
Figure 3-5: Electrical box accommodation (top view).....	84
Figure 3-6: Mounted antennas on the Earl Mountbatten roof.....	85
Figure 3-7: Typical USRP RF front end.....	86
Figure 3-8: Ettus B200 SDR transceiver board copied from [9].....	86
Figure 3-9: Rectangular window and its Fourier transform.....	88
Figure 3-10: 300Hz sampled frequency with spectrum leakage.....	89
Figure 3-11: No spectrum leakage when sampling a signal at 320Hz.....	89
Figure 3-12: Signal spectrum with the use of Hanning window.....	90
Figure 3-13: Signal spectrum with the use of flat-top window.....	90
Figure 3-14: USRP DSP block diagram.....	91
Figure 3-15: Beacon spectrum captured with the use of a Hanning (red) and flat-top (blue) window function.....	92
Figure 3-16: USRP recorded beacon and noise power.....	93
Figure 3-17: Beacon power received comparison with the B200 and NI 5124 card.....	93
Figure 3-18: Noise power recorded comparison with the B200 and NI 5124 card.....	94

Figure 3-19: Beacon signal recovery experiment .....	94
Figure 3-20: Received beacon signal (blue), identified clear sky segments (red) and zero-dB reference level fitted with Fourier series (black) .....	96
Figure 3-21: Approximated excess attenuation .....	96
Figure 4-1: Illustration of airmass.....	107
Figure 4-2: Photograph of the beacon receiver.....	117
Figure 4-3: Beacon receiver RF hardware (top) and DSP (bottom) block diagram .....	119
Figure 4-4: Atmospheric attenuation for July 2016.....	119
Figure 4-5: Decimated IF spectrum with beacon signal present.....	120
Figure 4-6: Digital notch filter response for measuring the noise power of the beacon.....	120
Figure 4-7: Reflector at zenith to accommodate the calibration box during the hot-cold calibration .....	121
Figure 4-8: Noise power recorded during the hot-cold calibration.....	122
Figure 4-9: Hot-Cold calibration plot .....	123
Figure 4-10: Tip curve calibration, corrected-tip and initial-tip in red and blue line respectively. Coefficient of determination ( $R^2$ ) is 0.9965 .....	124
Figure 4-11: Noise power recorded when pointed towards and away from Alphasat beacon .....	125
Figure 4-12: Estimated brightness temperature (blue) with temperature (orange) superimposed top and receiver beacon power (bottom) during a clear sky segment.....	126
Figure 4-13: Atmospheric attenuation for July 2016. In blue the atmospheric attenuation derived through power measurements, in red derived through the noise power measurements and in black different thresholds.....	127
Figure 4-14: Beacon derived and noise derived attenuation difference with all points included (black) and with over 3 dB fading excluded (blue) .....	128
Figure 4-15: CDF of the attenuation difference between the power derived and noise derived attenuation for July 2016 including all points (black) and the shown thresholds (tip-curve calibration coefficients) .....	129
Figure 4-16: CDF of the attenuation difference between the power derived and noise derived attenuation for July 2016 including all points (black) and the shown thresholds (hot-cold calibration coefficients) .....	130

## Table of Tables

Table 1-1: HTS & VHTS launch dates and total throughput.....	5
Table 1-2: Summary of propagation campaign payload specifications.....	13
Table 2-1: Beacon Frequency Plan .....	30
Table 2-2: Beacon Polarisation.....	31
Table 2-3: Beacon EIRP .....	32
Table 2-4: Phase Noise Mask .....	32
Table 2-5: Ka-Band (single HPA) component list, DC Power consumption and mass. (highlighted fields depict assumed values). .....	39
Table 2-6: Q-Band (single HPA) component list, DC Power consumption and mass. (highlighted fields depict assumed values). .....	42
Table 2-7: W-Band (single HPA) component list, DC Power consumption, and mass. (highlighted fields depict assumed values). .....	44
Table 2-8: Ka-Band ALC mechanism components .....	50
Table 2-9: Q-Band ALC mechanism components.....	51
Table 2-10: W-Band ALC mechanism components.....	52
Table 2-11: Ka-band initial link budget and margins achieved from simulations.....	53
Table 2-12: Q-band initial link budget and margins achieved from simulations .....	54
Table 2-13: W-Band initial link budget and margins achieved from simulations.....	54
Table 2-14: PLO-4000 and PLO-5200 phase noise [9], [10]. Highlighted fields are extrapolations from the datasheet. ....	60

Table 2-15: Expected phase noise for the chains. Highlighted fields are extrapolations from the datasheet.....	60
Table 2-16: Spectratime specifications copied from [13].....	62
Table 2-17: Beacon Mass and DC Power Consumption with a DC-DC converter efficiency of 75% .....	63
Table 2-18: Beacon Compliance Matrix.....	64
Table 2-19: Antenna parameters for European & Tropic and European-only coverage .....	66
Table 2-20: EIRP margin with EU payload design and EU & TC coverage antennas.....	66
Table 3-1: Ka-band Aldo Paraboni experimental propagation payload main characteristics .	72
Table 3-2: Skyware Technologies reflector antenna characteristics and XRF3100 LNB main characteristics.....	73
Table 3-3: Ka-band front end component list .....	74
Table 3-4: Cascaded Noise Figure of the Ka-band terminal.....	75
Table 3-5: Parameters for GS distance to satellite and GS elevation and azimuth calculations .....	76
Table 3-6: GS azimuth angle according to the location of the GS in respect to the satellite ..	77
Table 3-7: Link budget.....	79
Table 3-8: Antenna pointing loss .....	81
Table 3-9: Enclosure and electrical components for DC generation .....	83
Table 3-10: Ettus B200 receiver general characteristics.....	87
Table 4-1: Radiometer atmospheric absorption in clear sky throughout clear sky segment .	126
Table 4-2: The CDF of $\leq 0.5$ dB and $\leq 1$ dB for all points and different fading thresholds (tip-curve calibration coefficients).....	129
Table 4-3: The CDF of $\leq 0.5$ dB and $\leq 1$ dB for all points and different fading thresholds (hot-cold calibration coefficients).....	130



# Glossary

ADC – Analog-to-Digital Converter

CDF – Cumulative Distribution Function

CNR – Carrier-to-Noise Ratio

DAQ – Data Acquisition

DFT – Discrete Fourier Transform

DFDP – Dual Frequency Dual Polarisation

DSP – Digital Signal Processing

ECMWF – European Centre for Medium-Range Weather Forecasts

EIRP – Effective Isotropic Radiated Power

ESA – European Space Agency

EU – Europe/European

FFT – Fast Fourier Transform

GEO - Geostationary

HPA – High Power Amplifier

HTS – High Throughput Satellite

IF – Intermediate Frequency

ITU – International Telecommunication Union

ITU-R – International Telecommunication Union Recommendation

LNA – Low Noise Amplifier

LNB – Low Noise Block

LO – Local Oscillator

OMT – Orthogonal Mode Transducer

PIMP – Propagation Impairment Mitigation Techniques

QFN – Quinn-Fernandes Nessel

RAM – Radar Absorbing Material

RBW – Resolution Bandwidth

SDR – Software Defined Radio

SPDT – Single Pole Double Throw

SSPA – Solid State Power Amplifier

TSDP – Time Switched Dual Polarisation

TWT – Travelling-Wave Tube

USRP – Universal Software Radio Peripheral

# List of Publications

## Journal Papers

[J1] S. Ventouras, A. Martellucci, R. Reeves, E. Rumi, F. P. Fontan, F. Machado, V. Pastoriza, A. Rocha, S. Mota, F. Jorge, A. D. Panagopoulos, A. Z. Papafragkakis, C. I. Kourogiorgas, O. Fiser, V. Pek, P. Pesice, M. Grabner, A. Vilhar, A. Kelmendi, A. Hrovat, D. V. Janvier, L. Quibus, G. Goussetis, **A. Costouri**, J. Nessel, “Assessment of spatial and temporal properties of Ka/Q band earth-space radio channel across Europe using Alphasat Aldo Paraboni payload”, *International Journal of Satellite Communications and Networking*, vol. 37, no. 5, pp. 477–501, June 2019

[J2] **A. Costouri**, J. Nessel, and G. Goussetis, “Validation of a Digital Noise Power Integration Technique for Radiometric Clear Sky Attenuation Estimation at Q-Band”, *IEEE Transactions on Antennas and Propagation*, vol. 68, no. 9, pp. 6743–6751, September 2020.

## Conference Papers

[C1] **A. Costouri**, G. Goussetis, S. A. Kosmopoulos, R. Reeves, Ventouras, J. Mayock, S. Chan, P. D. Arapoglou, A. Martellucci, V. Valenta, “European W-Band Propagation Campaign Development”, in *IEEE 12<sup>th</sup> European Conference on Antennas and Propagation (EuCAP 2018)*, April 2018.

# Chapter 1

## 1 Introduction

The number of communication satellites have dramatically increased during the past decade. This is due to the notion of connecting and sharing our experiences and knowledge across the world. It is estimated that there were 1,145 million wired broadband connections in 2019 with a reported 4.1 billion people using the internet [1]. These broadband connections are used for a range of applications such as social media connectivity, music streaming, HD and 4K video streaming to name a few. In particular, the European Commission under the Digital Agenda for Europe from 2020 and onwards has foreseen that households will have internet connections beyond 30 Mbps [2]. Furthermore, 50% of households shall be able to subscribe to connections above 100 Mbps and key infrastructures like hospitals, airports and schools shall have access to connections above 1 Gbps [2] [3]. In most cases these would be serviced by the terrestrial infrastructure. However, it can be assumed that 5% -15%, depending on region, would not be able to be connected via the existing terrestrial infrastructure [4]. In such a case, future very high throughput satellite (VHTS) systems would be a solution.

Currently, most end user satellites operate in the microwave region with frequencies up-to Ku-band while gateway feeder links operate in the mm-wave region (at Ka-band) as well. Since the beginning of the millennium, communication satellites have started to migrate to Ka-band frequencies, beginning with the Spaceway F1 satellite 2005 [5]. The last decade has also seen an increase in Ka-band satellite payloads in an effort to achieve high throughput satellite (HTS) system throughputs. Upcoming VHTS systems such as ViaSat-3 [6], will still utilise Ka-band frequencies to achieve the demand in capacity. In order for the ground station gateways to have an acceptable quality of service, additional gateways will be required which would increase the network cost. An acceptable solution would be the use of higher mm-wave bands such as the Q-, V- and W-band since there is more available bandwidth compared to the existing infrastructure.

A potential architecture of a VHTS system is shown in Figure 1-1. Gateway feeder links in Figure 1-1 utilise V- and W-band for the downlink and uplink respectively and can

offer higher bandwidths than the traditional Ka-band channels. Furthermore, in Figure 1-1 the user link which can include video broadcasting and internet access now utilises the decongested Ka-band channels that are less susceptible to atmospheric impairments. As for the higher frequency gateway feeder links, smart gateway diversity can be utilised to tackle atmospheric impairments.

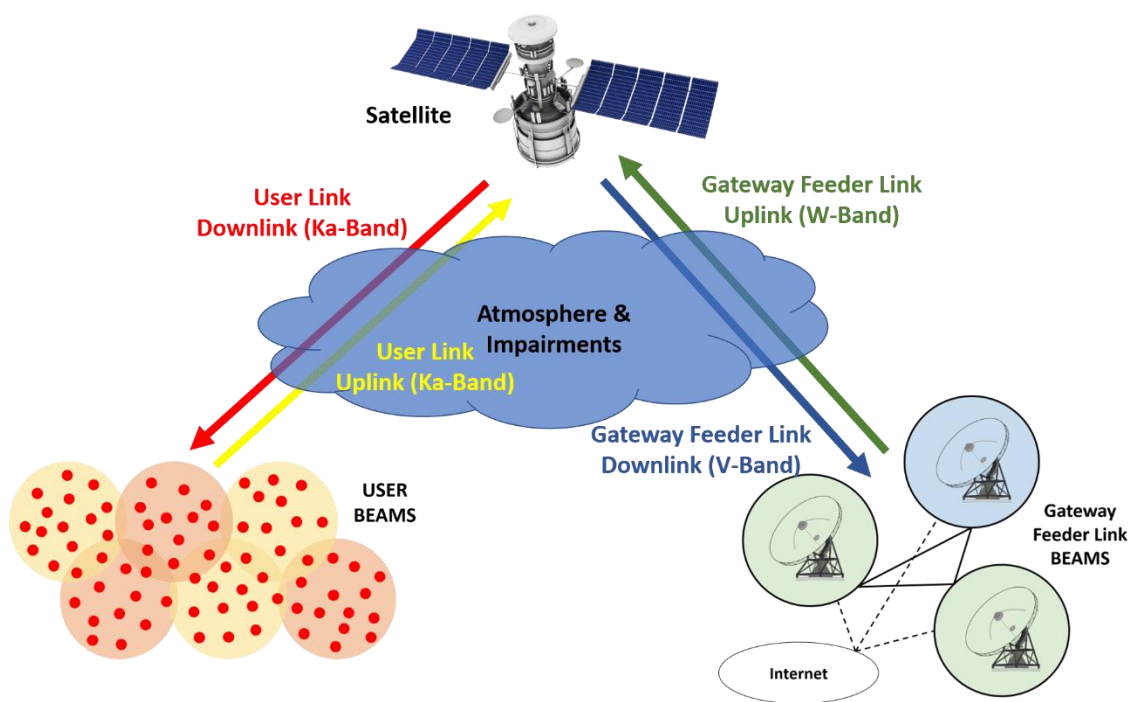


*Figure 1-1: Potential architecture of a VHTS system*

A constraint is that of the electromagnetic wave propagation through the atmosphere at these higher frequencies (Q-, V- W-band). Signal impairments increase with increasing frequency and previous propagation campaign satellites such as the ITALSAT, OLYMPUS and Alphasat have provided useful data for frequencies up to V-band. Furthermore, different regions have seasonal and diurnal variability which could affect the performance and availability of a satellite channel. Therefore, propagation studies especially at higher frequencies like W-band, where the field is still virgin in terms of satellite channel links, need to be conducted ahead of any satellite payload mission. ESA is currently working towards experimentally characterising the atmospheric impairments at W-band with a CubeSat [7] and potentially a geostationary satellite mission [8].

In recent years, traditional radio communication system hardware such as filters, mixers, and modulators have been implemented digitally via software. The use of software

defined radio (SDR), to replace hardware components with software has resulted in a cost effective solution to receivers and transmitters through the use of universal software radio peripheral (USRP) [9] [10]. This has enabled a number of ground terminals using SDR to monitor atmospheric impairments in several European locations such as Greece [11], Italy [12], Spain [13], Portugal [14], Slovenia [15] and Scotland [16]. SDR receivers have also made possible the conversion of these terminals into radiometers, able to monitor the atmosphere [17].

Therefore, to migrate gateway feeder links and end users to mm-waves, there is a need to study and characterise the atmospheric fading to estimate the viability and channel performance. Sections 1.1, 1.2 and 1.3 provide a background on communication satellites and future satellite gateways, propagation campaign payload heritage, and atmospheric propagation impairments respectively. Section 1.4 states the thesis motivation and outline.

## **1.1 Communication Satellites and Future Satellite Gateways**

The last decade has witnessed growth in the number of launches of high throughput satellite (HTS) systems. Moreover, the next generation of very high throughput satellite (VHTS) systems will offer ten times the throughput of current HTS systems. These are currently achieved with the use of the Ka-band frequency band. The demand for high service and quality satellite connection is ever increasing and is also very much cost driven. Currently there is a high cost in the satellite gateway feeder links. The cost could be decreased by reducing the number of gateways and could be achieved with higher bandwidth satellite channels. Gateways could be operated in the Q-, V- and W-band where available uplink and downlink bandwidth is more than 5 GHz which is twice as much as what Ka-band can offer according to the International Telecommunication Union (ITU) [18], [19].

Back in 1962, satellite frequency allocation for communication services across Europe started at C-band, a window of 4-8 GHz, and was primarily used for full-time satellite TV networks or raw satellite feeds [20]. The Telstar satellite relayed through space the first live transatlantic television feed. Telstar at the time had a payload with an uplink at 6 GHz and a downlink at 4 GHz [21]. Currently, satellite communications in Europe utilise

Ku- and Ka-bands with frequency ranges of 12-18 GHz and 18-40 GHz respectively [20]. A factor when selecting the communication band is the regional weather. During rainfall, the atmosphere has higher absorption and scattering, resulting in higher signal fading [22]. Furthermore, atmospheric fading rises with transmissions at shorter wavelengths [22]. Therefore, lower bands are more commonly used in areas with high rainfall in comparison to higher bands since the availability of the channel will be higher.

A question is raised on the use of shorter wavelengths for satellite communications since weather events can cause degradation of the channel. As usual, one of the trade-offs is that between the channel availability and capacity. With higher frequencies such as those in the Ka-band and beyond, more bandwidth is available and therefore higher capacities can be achieved. Currently, we are in the era of HTS systems, which can provide network capacities in the range of 100 Gbps. To achieve such capacities, payloads often deploy antennas that offer narrowly focused beams to achieve higher gains as well as higher bandwidths due to the higher frequency of the payloads.

Presently, Ka-band provides a good compromise in terms of available bandwidth and channel performance at a reasonable cost. In the past decade there has been an increase in HTSs at Ka-band. In 2011 and 2012, the HTS ViaSat-1 [23] and EchoStar XVII [24] were launched, with a total throughput of 140 Gbps and 120 Gbps respectively. This was followed in 2016 by the EchoStar family with XIX [25] which had a total throughput of 200 Gbps while ViaSat-2 [26] was launched a year after with 260 Gbps of total throughput. Eutelsat also launched Ka-Sat with a total throughput of 90 Gbps [27]. Now, the technology is pushing towards VHTS systems able to deliver up to 1Tbps with ViaSat-3 which is planned to be launched between 2021-2022 [6]. The above satellites operate at Ka-band frequencies and are listed in Table 1-1.

User links could be assigned all available Ka-band resources. This would mean that the satellite gateways would need to be either relocated to another coverage zone or utilise another frequency band for the feeder link which could provide sufficient bandwidth. Since the former is often not appropriate, higher frequency feeder links in Q/V-band and beyond need to be exploited.

*Table 1-1: HTS & VHTS launch dates and total throughput*

<b>Satellite</b>	<b>Launch</b>	<b>Total Throughput (Gbps)</b>
Viasat-1	2011	140
EchoStar XVII	2012	120
EchoStar XIX	2016	200
Ka-Sat	2016	90
Viasat-2	2017	260
Viasat-3	2021-2022	1000

Q/V-band, a region at 33-75 GHz in the frequency spectrum, has been considered as a baseline for the next generation systems [28], [29] and the Q/V Lift project is currently working towards the scenario where a Q/V-band feeder link is exploited [4]. In summary, a Q/V-band feeder link (downlink channel at 37.5 – 42.5 GHz and uplink at 47.2 – 50.2 and 50.4 – 52.4 GHz) provides sufficient bandwidth but suffers significantly from atmospheric fading due to adverse weather conditions, and smart gateway diversity concepts need to be deployed [30]–[33]. ESA is currently working towards characterising the atmospheric impairments at W-band(75 – 110 GHz) with a CubeSat [34] and potentially a geostationary (GEO) satellite mission [8], [35].

The exploitation of frequency bands beyond Q/V could offer a substantial capacity increase for the needs of both public and private sector satellite services, and the next step will be to look at W-band [36]–[38] for satellite communications from geostationary and non-geostationary earth orbits.

As mentioned above, the atmospheric losses and the atmospheric noise temperature (due to rain, water clouds and atmospheric gases) experienced at W-band will be more severe than at Ka-band. Nevertheless, an improved link availability can be achieved by proper selection of the ground station site and exploitation of the seasonal and diurnal variability or adopting fade mitigation techniques like site diversity, adaptive coding and modulation, antenna pattern reconfiguration or uplink power control.



Therefore, W-band system design and trade-offs require accurate propagation models and data. Current propagation models such as [39] and ITU-R recommendations [40] have been derived using past experimental satellite propagation campaigns at Ku-, Ka-, Q- and V-band [41]–[43]. Hence their applicability at W-band is in most cases rather limited.

The use of W-band for space systems has been investigated [44] but so far no measurement campaign has been done. Consequently, the possibilities for model development are quite limited and the accuracy of predictions for link budget analysis cannot be assessed. Hence, there is the need to start characterizing the W-band satellite propagation channel.

## **1.2 Propagation Campaign Payload Heritage**

Over the past three decades, there have been three GEO satellite propagation campaigns in Europe. The first campaign started with the ITALSAT F1 payload launched in January 1991 by the Italian Space Agency. The payload had a three-frequency plan with beacons at 20 GHz (Ka-Band), 40 GHz (Q-Band) and 50 GHz (V-Band). As seen from Figure 1-2, the lower band beacon at 20GHz had a coverage of only central Europe with the boresight point of the beam in Italy [41]. The 40 GHz and 50 GHz beacon had a larger coverage of Europe as seen from Figure 1-3 [41]. The polarisation was linear vertical, right hand circular and switched linear polarisation for the 20 GHz, 40 GHz and 50 GHz beacons respectively. The ITALSAT propagation campaign was successful in the sense that the beacons were online until January 2001 [45].

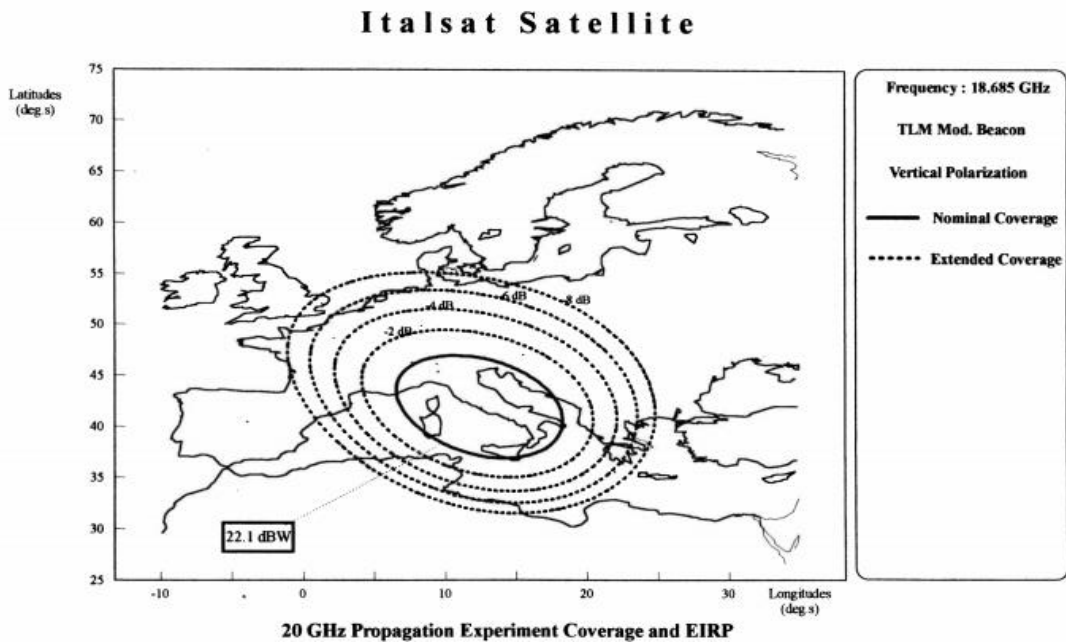


Figure 1-2: ITALSAT F1 Ka-band payload antenna coverage copied from [41]

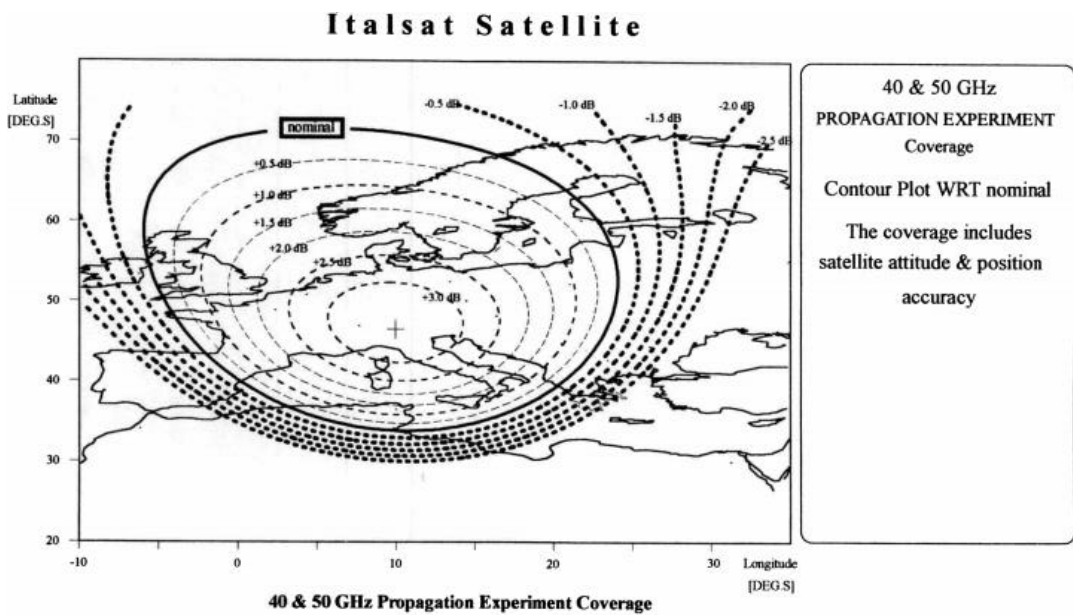


Figure 1-3: ITALSAT F1 Q/V-band payload antenna coverage copied from [41]

The Ka-band modulated beacon is a multiple of a 3737 MHz carrier generator which is multiplied by x5 with a frequency multiplier to form the 18.68 GHz signal. Figure 1-4, Figure 1-5 and Figure 1-6 provide the simplified block diagrams of the Ka-, Q- and W-band upconverters [41], [46]. The millimetre wave beacons have a common local oscillator at 2474.5 MHz. The Q-band uses two x4 frequency multiplier to achieve its 39.59 GHz signal while the V-band deploys a x5 and x4 frequency multipliers to achieve

its 49.49 GHz signal. V-band circular polarisation is achieved with the use of a millimetre wave polariser placed ahead of the antenna as shown in Figure 1-6. The V-band switched polarisation deployed a single pole double throw switch that switched at a rate of 933 Hz. The two outputs of the switch were connected to an orthomode transducer (OMT). An OMT is a three-port waveguide device that is often called a polariser duplexer as one of the ports provides vertical polarisation, the other horizontal polarisation and the third the combination. It is more often used in receiver terminals where the uplink and downlink signals are orthogonally polarised to each other and in this case; it is used to feed the antenna the linear and vertical polarisation at the switching rate as seen in Figure 1-6. The relevant amplifiers, couplers and filters were used in the upconverted chains. Moreover, all chains benefitted from a redundancy chain to mitigate for component failure during the campaign.

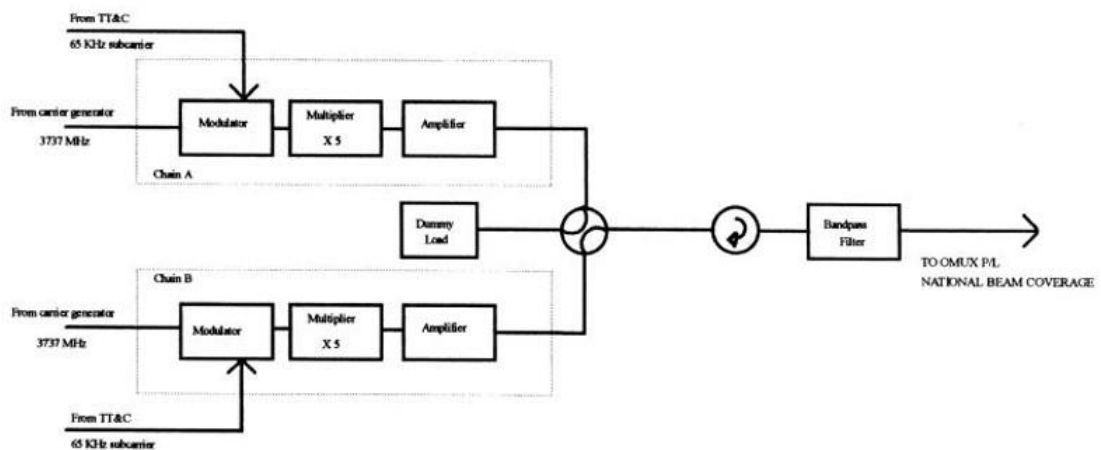


Figure 1-4: ITALSAT F1 Ka-band payload block diagram copied from [41]

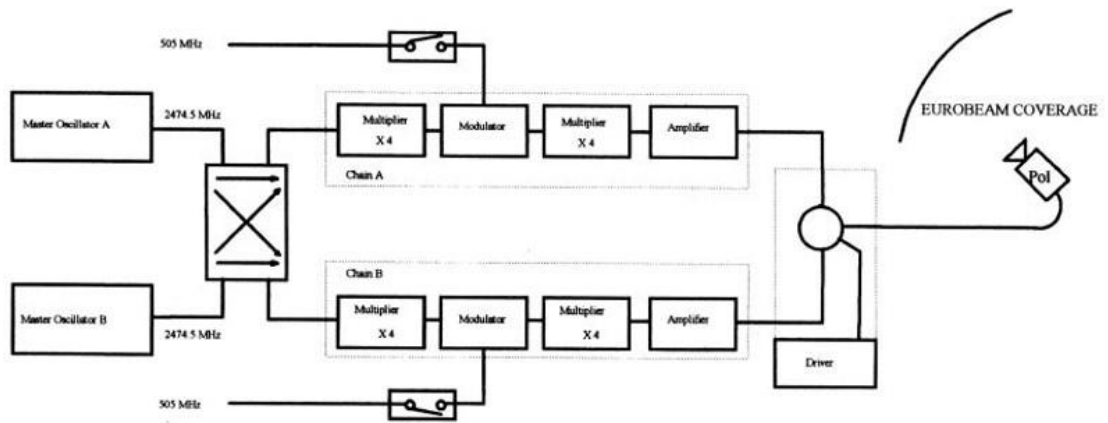


Figure 1-5: ITALSAT F1 Q-band payload block diagram copied from [41]

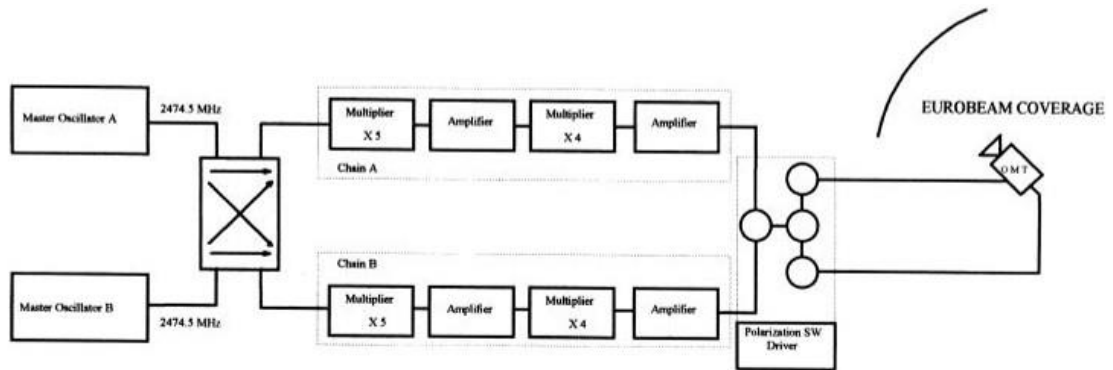


Figure 1-6: ITALSAT F1 V-band payload block diagram copied from [41]

The OLYMPUS propagation payload launched in 1989 in an effort to obtain experimental propagation data in the Ku- and Ka-bands across Europe. The payload had a three-frequency plan with beacons at 12 GHz (Ku-band), 20 GHz (Ka-band) and 30 GHz (Ka-band). As seen from Figure 1-7, the Ka-band beacons had a larger coverage of Europe in comparison to the ITALSAT campaign. The polarisation was linear vertical and switched linear polarisation for the 12 GHz, 30 GHz and 20 GHz beacons respectively. In August 1993 the satellite began spinning and was deemed impossible to recover and was therefore decommissioned and removed from geostationary orbit [47].

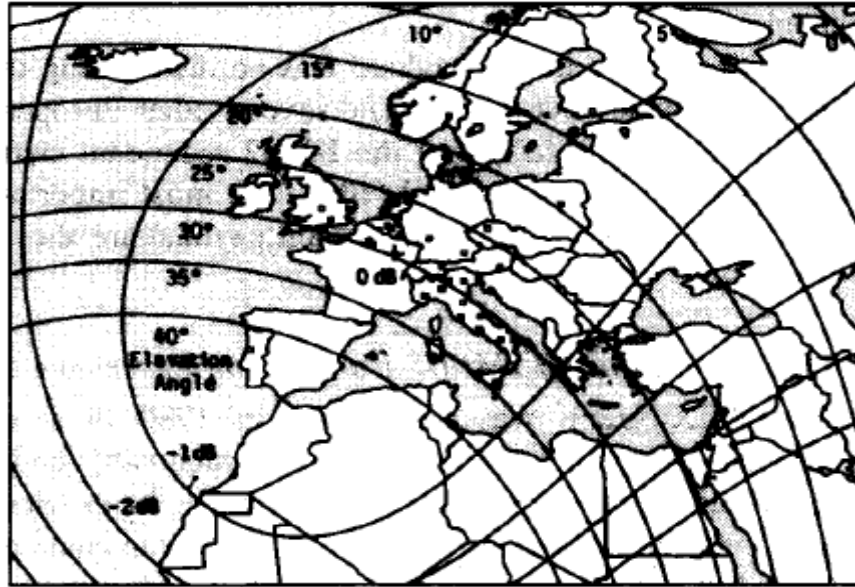


Figure 1-7: OLYMPUS Ka-band payload antenna coverage copied from [48]

All frequencies of the OLYMPUS payload originate from a common crystal oscillator at 48.457 MHz which is multiplied sixfold with a frequency multiplier (290.742 MHz) to branch out at the Ku- and Ka-band up-conversion chains. The Ku-band chain uses a single x43 frequency multiplier to achieve its 12.5 GHz signal. The Ka-bands achieve a common frequency of 9.885 GHz through a x34 frequency multiplier. The 19.77 GHz and 29.66 GHz frequencies are achieved through a x2 and x3 frequency multipliers. The lower Ka-band beacon offered switched vertical and horizontal polarisation at a rate of 933 Hz which was achieved through a similar configuration of switching and an OMT as the ITALSAT V-band payload. The block diagram of the three-frequency payload can be seen in Figure 1-8 [48].

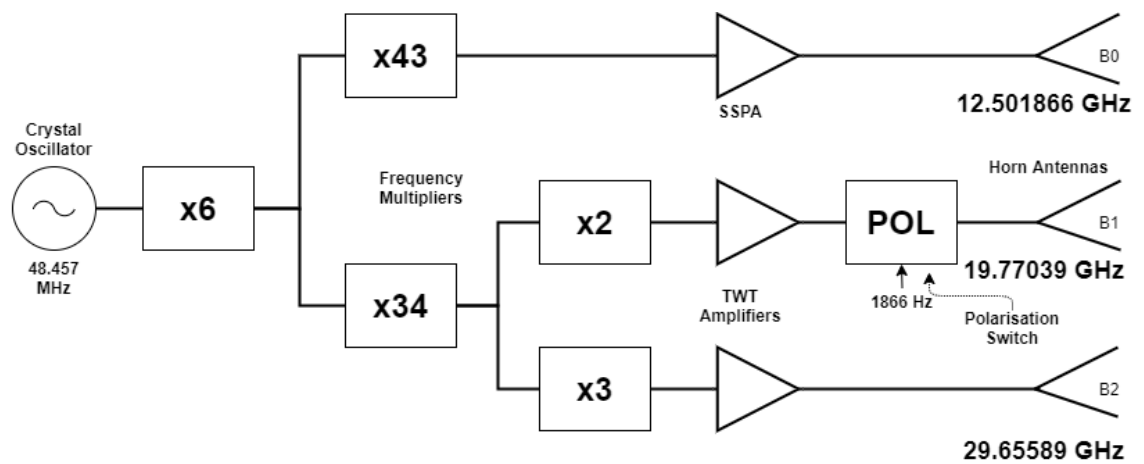
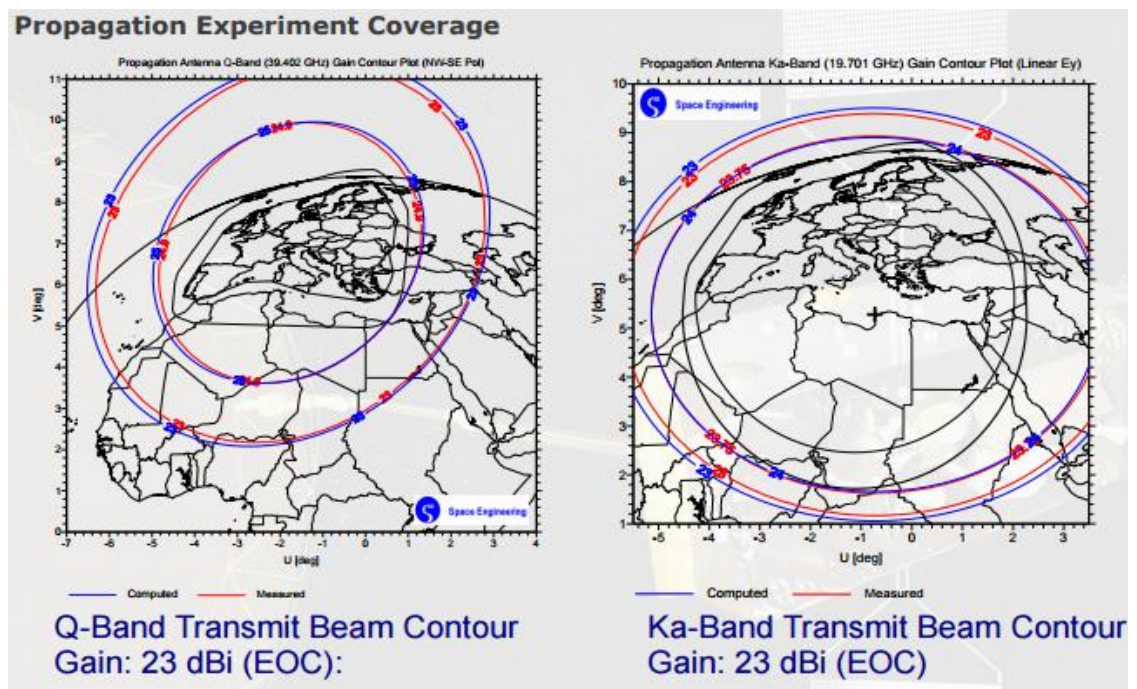


Figure 1-8: OLYMPUS Ku- and Ka-band payload block diagram adapted from [48]

The current and ongoing European propagation satellite payload is that of Alphasat, which was launched in July 2013. The Alphasat TDP#5 payload was later renamed the ‘Aldo Paraboni payload’ in honour of Professor Aldo Paraboni, who promoted the effort from the beginning but sadly passed away before its realisation [49]. The propagation payload offered a two-frequency plan at 19.701 GHz (Ka-Band) and 39.402 GHz. As seen from Figure 1-9, the Ka-band beacon offered coverage over Europe and the Tropics while the Q-band beacon only covered Europe and the Tropics while the Q-band beacon only covered Europe. The polarisation is linear vertical and 45° tilted for the Ka- and Q-band respectively [50].



*Figure 1-9: Aldo Paraboni (Alphasat) Ka-band (right) and Q-band (left) payload antenna coverage copied from [51]*

The Aldo Paraboni payload utilised two oscillators connected to a common master oscillator mixed to form the Ka-band signal at 19.701 GHz. The Q-band payload was branched out through a coupler and a x2 frequency multiplier was used to convert it to 39.402 GHz as seen from Figure 1-10. Both beacons had linear polarisations and therefore no switch or polariser like the previous campaign payloads was used. A redundancy payload was available in case of a component failure. Furthermore, given their critical role in delivering the correct power to the antenna, the high-power amplifiers had a redundancy [51].

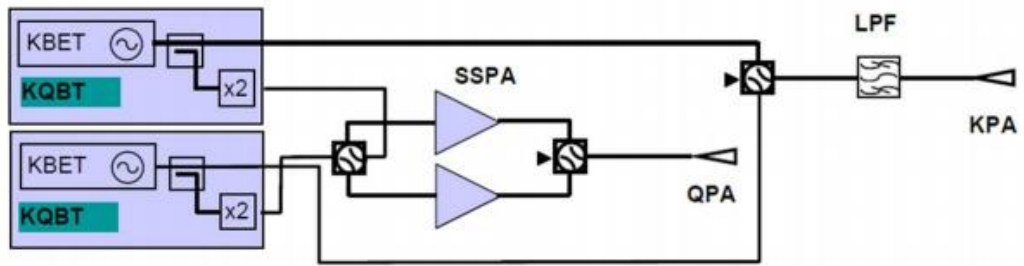


*Figure 1-10: Aldo Paraboni (Alphasat) Ka-band and Q-band payload block diagram copied from [51]*

Table 1-2, summarises the three propagation campaign payloads. It includes information on, frequency, polarisation, coverage, boresight location, Effective Isotropic Radiated Power (EIRP) and EIRP stability.

Table 1-2: Summary of propagation campaign payload specifications

	ITALSAT			OLYMPUS			Aldo Paraboni	
<b>Frequency (GHz)</b>	18.685	39.592	49.49	12.5	19.77	29.66	19.701	39.402
<b>Band</b>	Ka-Band	Q-Band	V-Band	Ku-Band	Ka-Band	Ka-Band	Ka-Band	Q-Band
<b>Polarisation</b>	Linear V	RHCP	Linear H/V	Linear V	Linear H/V	Linear V	Linear V	Linear tilt 45°
<b>Pol. Switching (Hz)</b>	N/A	N/A	933	N/A	933	N/A	N/A	N/A
<b>Boresight Location</b>	Appr. 42°N 12°E (IT)	Appr. 50°N 11°E (DE)		Appr. 46°N 2.8°E (FR)			32.5°N 20°E (LY)	45° N 9°E (IT)
<b>Coverage</b>	Italy	Main Europe		Europe	Europe		Europe and TC	Europe
<b>EIRP (dBm)</b>	55.9	58.8	56.6	43.1	61.7	57.7	49.5	56.5
<b>EIRP Stability 24h (db)</b>	±1.25	±0.55	±0.65	±0.25	±0.4	±0.86	±0.5	±0.5



## 1.3 Atmospheric Propagation Impairments

The following sections look at the first order atmospheric propagation impairments (gaseous attenuation, cloud attenuation, rain attenuation, scintillation and depolarisation) including assessments of the current ITU-R models. The impairments include [52]:

- Gaseous attenuation - An always present, slowly changing, component of total attenuation of the order of few dBs which depends on the elevation angle and the season.
- Cloud attenuation - depending on the elevation angle and type of cloud can contribute significant loss to the total attenuation.
- Rain attenuation - Rain attenuation is the dominant attenuation factor for systems operating at frequencies above 10GHz. In addition, for systems operating at Q/V and W-bands rain can considerably limit their availability and could result in unrealistic fade margin. Thus, the understanding of rain propagation characteristics is required for the link budget and propagation impairment mitigation techniques.
- Scintillation - Caused by rapid fluctuations in the refractive index of the atmosphere. Scintillation effects occur on time scales under ~0.5 seconds and limit the performance of high data rate, complex modulation systems.
- Depolarisation - Signal leakage between polarisations.

### 1.3.1 Gaseous Attenuation

As in the lower frequency Ku- and Ka-bands, atmospheric gases (water vapour and oxygen) affect radio wave propagation in the higher Q/V and W-bands. Figure 1-11 shows the specific gaseous attenuation in the Q/V and W-band frequency ranges in comparison with the lower frequencies. The total specific gaseous attenuation includes the dry air and water vapour specific gaseous attenuation.

The models currently recommended by the ITU-R (Rec. P.676) [53] for the prediction of gaseous attenuation along a slant path rely on solid physical bases and, as such, they are expected to provide reliable estimations at least up to 100 GHz. Since the ITU-R models

have only been validated for frequencies up to 50 GHz, further validation is recommended before their use for system design in W-band.

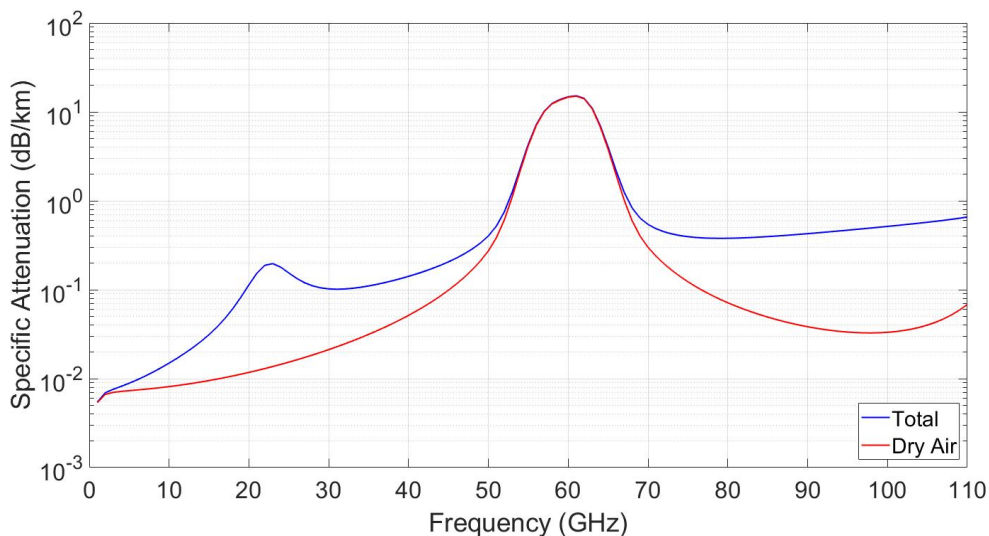


Figure 1-11: Total (blue) and dry air (red) specific gaseous attenuation

### 1.3.2 Cloud Attenuation

Attenuation of electromagnetic radiation by liquid water cloud particles in the atmosphere becomes significant when transmission frequencies exceed 20 GHz. The attenuation increases with frequency, and with decreasing temperature. However, when the particles freeze, the attenuation level falls significantly because the dielectric constant of ice is nearly two orders of magnitude below that of liquid water [52].

Once the size of suspended water droplets in the clouds is smaller than the propagating wavelength, the Rayleigh approximation can be used for the computation of the extinction cross sections and, thus, the cloud attenuation depends only on the liquid water content, on the droplets' temperature in addition to the frequency.

In ITU-R (Rec. P.840) [54], cloud attenuation is calculated through an effective parameter, that is the reduced liquid water total content measured in  $\text{kg/m}^2$  or mm normalised to  $0^\circ\text{C}$ . This parameter is a function of frequency, and its statistics are currently calculated by ITU-R in the 20–50 GHz band (but it can be recalculated in different frequency bands) and distributed through global maps. Cloud attenuation is then

obtained as a function of the reduced liquid water total content, the water permittivity, the frequency and the elevation angle.

### 1.3.3 Rain Attenuation

Rain attenuation is the dominant source of propagation impairment, especially at frequencies above about 20 GHz. The accurate determination of rain specific attenuation,  $\gamma_R$ , is not generally straightforward, requiring complex calculations of the forward scattering amplitudes,  $S(D)$  as a function of rain drop diameter  $D$ , which are then integrated with the rain drop size distribution (DSD),  $N(D)$ , to yield the specific attenuation at a given rainfall rate. Involved in this process is additional information on the fall (terminal) velocity of rain drops, since the drop size distributions in use are not generally self-consistent. That is, they do not, when integrated with the raindrop fall velocity, yield the true rainfall rate, and normalization is generally required.

This procedure can be approximated, however, by the simple power-law relationship:

$$\gamma_R = 4.343 \times 10^{-3} \lambda \int_{D_{min}}^{D_{max}} N(D) \text{Im}[S(D)] dD \approx kR^a \text{ (dB/Km)} \quad (1.1)$$

where  $\lambda$  is the wavelength. The above equation is used to cope with the temporal characteristics of the attenuation, namely to map statistically the rain rate to dB/km. The model for rain specific attenuation in Recommendation P.838-3 [55] is perhaps the most widely used method and is common to practically all models for both slant-path and terrestrial rain attenuation.

Since no experimental measurements are available for Earth-to-satellite links at frequencies above 50 GHz against which the models' performance can be tested, methods developed on solid physical bases should be preferred, because their estimation accuracy is not expected to depend markedly on the frequency. In this scenario, the Stratiform Convective EXponential CELL (SC EXCELL) [56] model represents one of the best candidates because of its physical nature and its very good overall prediction performance.

Empirical methods, whose parameters are usually derived from the comparison with measurements, are less attractive in this context because they are not adequately 'tested'

against measurements above 50 GHz. However, the physical models are based on assumptions and have crucial parameters that have to be adjusted on measurements.

Although the predictions of rain attenuation statistics using the ITU-R model and the SC EXCELL model are similar in the 17-50 GHz range, at W-band there is a significant inconsistency. For example, for a link in Madrid, operating at 81 GHz, vertically polarised and elevation angle of  $39^\circ$  the ITU-R model predicts ~20 dB more attenuation than the SC EXCELL model at 0.01%. This clearly shows that predictions based purely on models cannot be relied upon to accurately predict link performance at W-band.

#### 1.3.4 Scintillation

Scintillations are fast fluctuations of the received signal amplitude with peak-to-peak time intervals spanning a few seconds period and limit the performance of high data rate, complex modulation systems. Moreover, it is worth noting that the dynamics of scintillation may interfere with tracking systems. They are associated with refractive index irregularities produced by tropospheric turbulence and with the wave extinction mechanism caused by rain. The clear air scintillations – which are much more severe at lower elevation angles – may produce degradations in low availability systems [52].

The signal standard deviation, calculated during a stationary period of few minutes, depends on the turbulence structure index, increases with the frequency and with the path length and decreases when the antenna size increases because of aperture averaging.

Scintillation measurements are required also for the lower than W-band frequency bands bearing in mind that the current ITU-R model (Rec. P.618) [57] is valid up to 20 GHz.

#### 1.3.5 Depolarisation

The use of orthogonal polarisations permits, in principle, an increase in spectrum efficiency by the transmission of two independent channels in the same frequency band. In practice there are limitations imposed on this by propagation impairments that give rise to interference between such channels, as well as system impairments such as imperfect antennas. Focusing on the propagation effects, adaptive control of these depolarisation

phenomena demands adequate understanding of the physical mechanisms that cause them.

Two quantities have been introduced in order to study the depolarisation phenomena: cross-polar isolation (XPI) and cross-polar discrimination (XPD). If  $E_{Tx}$  and  $E_{Ty}$  are the transmitted signals in the two orthogonal polarisations  $x$  and  $y$ , generally, the received signals are:  $E_{Rxx}$ ,  $E_{Ryx}$ ,  $E_{Rxy}$ ,  $E_{Ryy}$  where for the receiving signals notation the first index shows the transmitted polarisation and the second index the polarisation of the received signal, as shown in Figure 1-12.

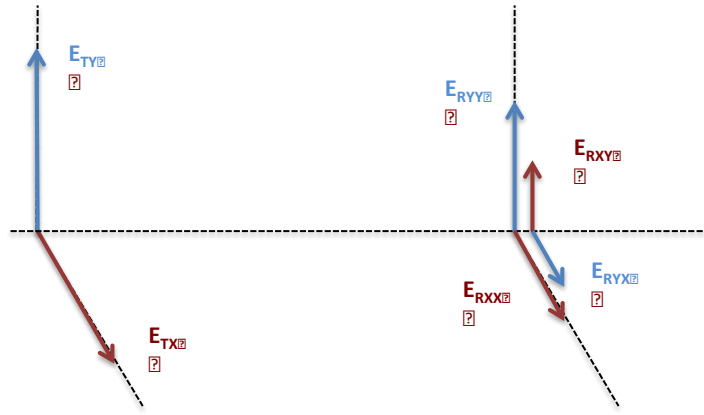


*Figure 1-12: Representation of co-polarised and cross-polarised signals. The polarisations can be linear or circular – only linear polarisation is shown for clarity of illustration.*

The horizontal,  $CPA_x$ , and vertical,  $CPA_y$ , co-polar attenuation (CPA) in dB is the logarithmic ratio of the received electric field to the transmitted electric field of the equivalent polarisation.

$$CPA_x = -20 \log_{10} \left| \frac{E_{Rxx}}{E_{Tx}} \right| \quad (1.2a)$$

$$CPA_y = -20 \log_{10} \left| \frac{E_{Ryy}}{E_{Ty}} \right| \quad (1.2b)$$

The horizontal,  $XPD_x$ , and vertical,  $XPD_y$ , cross-polar discrimination in dB is the logarithmic ratio of the orthogonal received electric fields.

$$XPD_x = 20 \log_{10} \left| \frac{E_{Rxx}}{E_{Rxy}} \right| \quad (1.3a)$$

$$XPD_Y = 20 \log_{10} \left| \frac{E_{RYY}}{E_{RYX}} \right| \quad (1.3b)$$

The horizontal,  $XPI_X$ , cross-polar isolation in dB is the logarithmic ratio of the received electric field in the  $x$ -plane to the received electric field in the  $y$ -plane. The vertical,  $XPI_Y$ , cross-polar isolation in dB is the logarithmic ratio of the received electric field in the  $y$ -plane to the received electric field in the  $x$ -plane.

$$XPI_X = 20 \log_{10} \left| \frac{E_{RXX}}{E_{RYX}} \right| \quad (1.4a)$$

$$XPI_Y = 20 \log_{10} \left| \frac{E_{RYY}}{E_{RXY}} \right| \quad (1.4b)$$

where, the total received electric fields  $E_{RX}$  and  $E_{RY}$  are:

$$E_{RX} = E_{RXX} + E_{RYX} \quad (1.5a)$$

$$E_{RY} = E_{RXY} + E_{RYY} \quad (1.5b)$$

The two signal components used to determine XPI are received on the same polarisation whereas for XPD on orthogonal polarisations. The majority of existing propagation databases and consequently the prediction models refer to XPD – mono-polarised transmissions can provide measurements only of XPD. However, for the design of dual polarised communication systems, XPI is of interest. In this context, for propagation through rain, XPI has been shown theoretically to be equivalent to XPD if certain raindrop symmetry criteria are met. Furthermore, measurements at 19 GHz using the COMSTAR satellites confirmed this conclusion [58]. However, there have been limited depolarisation measurements in Europe at Ka and Q/V-band.

The tropospheric particles that can contribute to depolarisation along a slant path are raindrops (non-spherical), melting particles and ice crystals. For rain, the simultaneous presence of attenuation in the co-polar channel has led to the development of models which derive the XPD from the CPA, the statistics of which have been more widely explored in the ITU-R Rec. P.618 [57]. However, there are difficulties in situations where there is significant ice depolarisation present on the path, regardless of the presence or absence of rain.

Currently the ITU-R Rec. P.618-13 [57] accounts for the additional effects of ice via an empirical correction term. The empirical nature of the correction means it is appropriate for geographic regions for which the data used in deriving it were measured, but there is

no clear way to extend this to other regions and account for climatic variability. Also, the current XPD model (ITU-R P.618-13) effectively treats the effects of ice depolarisation as a rain-attenuation effect. At the higher frequency bands this is a source of significant error in the mean XPD value for low rain conditions, which represent a major proportion of the time.

Currently there is no support in the ITU-R models for XPD above 55 GHz. This factor ought to be addressed to allow for more accurate system planning for possible future use of W-band for systems that demand huge bandwidths.

## **1.4 Motivation and Thesis Outline**

The motivation of the thesis is to highlight the importance of propagation studies and their impact on the design of future VHTS systems and the migration of gateway feeder links and end users to mm-waves. The central aim of the thesis is the development and characterisation of satellite channels. In particular, the design of a satellite payload, the design and implementation of a ground receiver and the study of atmospheric noise and fading of the channel. This thesis describes, through five chapters (including this one), the achievement of this aim.

Chapter 2 presents the requirements and design simulations of a geostationary satellite payload for propagation measurements at Ka-band (19 GHz), Q-band (38 GHz) and W-band (76 GHz). A discussion on various design trade-offs is shown along with future work that needs to be done in order to kickstart such a campaign.

Chapter 3 presents the design and implementation of a Ka-band receiver at 19.701 GHz for propagation measurements. The link budget is presented along with the hardware selection and digital signal processing. The recorded data of the receiver are also presented along with methodology for calculating excess channel fading.

Chapter 4 presents the theory and implementation of a digital radiometer that can monitor atmospheric noise and fading at Q-band (39.402 GHz). The experimental setup and calibration are presented along with its validation.

Chapter 5 presents a summary of the work carried out in the thesis along with conclusions and future work.

## 1.5 Summary

In summary, there is a clear interest in migrating to higher frequencies such as W-band to meet the growing demand in satellite systems for commercial applications. Furthermore, previous and ongoing propagation campaigns were able to model atmospheric impairments through experimental satellite payloads but are limited up to V-band. Characterisation and validation of the current models up to W-band requires a new satellite propagation payload. Previous propagation payloads have been considered in an effort to gain knowledge on how to design a payload at W-band. Also, the first order atmospheric impairments, which includes gaseous, cloud and rain attenuation, scintillation and depolarisation are described. Their current ITU-R models and shortcoming in terms of their validity for channel estimations at W-band was assessed. In particular, gaseous attenuation estimations for W-band are not expected to decrease substantially. Cloud and rain attenuation models have been modelled up to 50 GHz. As for scintillation, the model available is up to 20 GHz and the depolarisation model has no support above 55 GHz.



## References

- [1] J. Clement, "Number of fixed broadband internet subscriptions worldwide 2005-2019," 2020. <https://www.statista.com/statistics/268673/number-of-broadband-internet-subscriptions/>.
- [2] Communication from the Commission to the European Parliament, "Connectivity for a Competitive Digital Single Market - Towards a European Gigabit Society," 2016. doi: 10.1017/CBO9781107415324.004.
- [3] Communication from the Commission, "A strategy for smart, sustainable and inclusive growth," 2010.
- [4] M. Bergmann *et al.*, "Q/V-band feeder links and flexible bandwidth assignment in future very high throughput satellite (VHTS) communication systems," in *23rd KA and Broadband Communications*, 2017.
- [5] SPACEREF, "DIRECTV's Spaceway F1 Satellite Launches New Era in High-Definition Programming; Next Generation Satellite Will Initiate Historic Expansion of DIRECTV," 2005. <http://www.spaceref.com/news/viewpr.html?pid=16748>.
- [6] ViaSat, "Going Global." <https://www.viasat.com/news/going-global>.
- [7] J. Flavio *et al.*, "A New Earth-LEO Propagation Campaign at Q and W-band," *2018 9th Adv. Satell. Multimed. Syst. Conf. 15th Signal Process. Sp. Commun. Work. ASMS/SPSC 2018*, pp. 1–6, 2018, doi: 10.1109/ASMS-SPSC.2018.8510750.
- [8] ESA-ESTEC, "Statement of Work: W-Band Technology Developments Towards First Beacon- Based Propagation Campaign."
- [9] M. Dillinger, K. Madani, and N. Alonistioti, *Software Defined Radio: Architectures, Systems and Functions*. Wiley, 2003.
- [10] "GNU Radio Opens an Unseen World," 2006. <https://www.wired.com/2006/06/gnu->

radio-opens-an-unseen-world/.

- [11] A. Z. Papafragkakis, N. K. Lyras, C. I. Kourogiorgas, and A. D. Panagopoulos, "Propagation measurements campaign in Athens with ALPHASAT at Ka-band using Software Defined Radio technologies," *Proc. 2015 Int. Conf. Electromagn. Adv. Appl. ICEAA 2015*, pp. 634–637, 2015, doi: 10.1109/ICEAA.2015.7297194.
- [12] M. Zemba, J. Nessel, C. Riva, L. Luini, and G. Goussetis, "NASA's alphasat propagation terminals: Milan, Italy, and Edinburgh, Scotland," *Int. J. Satell. Commun. Netw.*, vol. 37, no. 5, pp. 502–512, 2019.
- [13] F. Machado, E. Vilar, F. P. Fontán, V. Pastoriza, and P. Mariño, "Easy-to-build satellite beacon receiver for propagation experimentation at millimeter bands," *Radioengineering*, vol. 23, no. 1, pp. 154–164, 2014.
- [14] A. Rocha, S. Mota, and F. Jorge, "Propagation campaign at Q-band and Ka-band using the Alphasat and Ka-Sat satellites," in *12nd European Conference on Antennas and Propagation (EuCAP 2018)*, 2018, pp. 904–5.
- [15] S. Mrak, A. Hrovat, M. Vidmar, and A. Vilhar, "A discrete-components millimeter-wave satellite beacon receiver for Q-band propagation experiment," *Int. J. Satell. Commun. Netw.*, vol. 36, no. 4, pp. 372–382, 2018, doi: 10.1002/sat.1240.
- [16] J. Nessel, N. Glenn, M. Zemba, and N. Glenn, "Design and Preliminary Results from Edinburgh , UK , Alphasat Q-band Propagation Terminal," in *22nd Ka and Broadband Communications Conference, Cleveland, Ohio*, 2016.
- [17] A. Costouri, J. Nessel, and G. Goussetis, "Validation of a Digital Noise Power Integration Technique for Radiometric Clear Sky Attenuation Estimation at Q-Band," *Trans. Antennas Propag.*, pp. 1–9.
- [18] H. Fenech, S. A. A. Hirsch, and V. Soumholphakdy, "VHTS Systems : Requirements and Evolution," in *11th European Conference on Antennas and Propagation (EuCAP 2017)*, 2017, pp. 2409–2412.
- [19] International Telecommunication Union, "Radio Regulations: Articles," vol. 1, 2016, doi: 10.1016/B978-0-12-394583-9.00020-X.

- [20] ESA, "Satellite frequency bands." [https://www.esa.int/Applications/Telecommunications\\_Integrated\\_Applications/Satellite\\_frequency\\_bands](https://www.esa.int/Applications/Telecommunications_Integrated_Applications/Satellite_frequency_bands).
- [21] Don I. Dalgleish, *An Introduction to Satellite Communications*. 1989.
- [22] J. E. Allnut, *Satellite-to-Ground Radiowave Propagation*, 2nd Editio. IET, 2011.
- [23] Eutelsat, "Eutelsat Communications Via Ka-Sat," 2017. [http://www.eutelsat.com/files/contributed/news/media\\_library/brochures/ka-sat-professional-services.pdf](http://www.eutelsat.com/files/contributed/news/media_library/brochures/ka-sat-professional-services.pdf).
- [24] Hughes, "Hughes High-Throughput Satellite Constellation - ECHOSTAR XVII." <https://www.hughes.com/technologies/hughes-high-throughput-satellite-constellation/echostar-xvii>.
- [25] Hughes, "Hughes High-Throughput Satellite Constellation - EchoStar XIX," [Online]. Available: <https://www.hughes.com/technologies/hughes-high-throughput-satellite-constellation/echostar-xix>.
- [26] ViaSat, "VIASAT-2 AT A GLANCE." [https://www.viasat.com/sites/default/files/media/documents/770853\\_vs-2\\_2019\\_infographic\\_009\\_lores.pdf](https://www.viasat.com/sites/default/files/media/documents/770853_vs-2_2019_infographic_009_lores.pdf).
- [27] Eutelsat Broadband, "EUTELSAT COMMUNICATIONS VIA KA-SAT: GLOBAL COMMUNICATION SOLUTIONS FOR ANY SITUATION." <https://de.eutelsat.com/files/live/sites/eutelsatv2/files/contributed/products/pdf/Eutelsat-Broadband.pdf>.
- [28] J. V. Evans and A. Dissanayake, "PROSPECTS FOR COMMERCIAL SATELLITE SERVICES AT Q- AND V-BANDS," *Proc. IEEE Mil. Commun. Conf.*, vol. 1, pp. 1–7, 1998.
- [29] P. Angeletti, F. Coromina, F. Deborgies, R. De Gaudenzi, A. Ginesi, and A. Vernucci, "SATCOMS 2020 R&D challenges: Part I: Broadband fixed communications," *IET Conf. Publ.*, no. 552 CP, 2009, doi: 10.1049/cp.2009.1238.
- [30] A. Kyrgiazos, B. G. Evans, and P. Thompson, "On the Gateway diversity for high throughput broadband satellite systems," *IEEE Trans. Wirel. Commun.*, vol. 13, no. 10, pp. 5411–5426, 2014, doi: 10.1109/TWC.2014.2339217.

- [31] N. Jeannin, L. Castanet, J. Radzik, B. Michel, and B. Evans, "Smart gateways for terabit/s satellite," *Int. J. Satell. Commun. Netw.*, no. January, pp. 93–106, 2014, doi: 10.1002/sat.
- [32] J. Lemorton *et al.*, "Development and validation of time-series synthesizers of rain attenuation for Ka-band and Q/V-band satellite communication systems," *Int. J. Satell. Commun. Netw.*, no. October, pp. 575–601, 2007, doi: 10.1002/sat.
- [33] T. Rossi *et al.*, "Experimental assessment of optimal ACM parameters in Q/V-band satellite communication," *IEEE Aerosp. Conf. Proc.*, vol. 2016-June, pp. 1–10, 2016, doi: 10.1109/AERO.2016.7500774.
- [34] M. Schmidt, J. Säily, T. Tikka, L. Cupido, M. Rösch, and B. Schoch, "Architecture of a Cubesat based W-band channel measurements system," *Ka Broadband Commun. Conf.*, 2018.
- [35] A. Costouri *et al.*, "European W-Band Propagation Campaign Development," in *12th European Conference on Antennas and Propagation (EuCAP 2018)*, 2018.
- [36] R. Acosta *et al.*, "W / V-Band RF Propagation Experiment Design," vol. 3127, 2019.
- [37] A. K. Weaver-Madsen, "A Technology Payload System for Exploration of the W- and V-band Spectrum," in *20th Ka and Broadband Communications, Navigation and Earth Observation Conference, Salerno, Italy*, 2014.
- [38] A. Jebiril, M. Lucente, M. Ruggieri, and T. Rossi, "WAVE- A new satellite mission in W-band," *IEEE Aerosp. Conf. Proc.*, vol. 2005, no. 1, pp. 870–879, 2005, doi: 10.1109/AERO.2005.1559378.
- [39] D. Vanhoenacker-Janvier *et al.*, "Characterization and modeling of propagation effects in 20-50 GHz band," *11th Ka Broadband Commun. Conf.*, no. 1, pp. 195–202, 2005.
- [40] International Telecommunication Union, "REC-P, Radiowave Propagation." .
- [41] ASI, "ITALSAT Propagation Experiment User Guide." 1994.
- [42] ESA, "OLYMPUS USER GUIDE, Propagation Package." 1989.
- [43] A. Martellucci, J. R. Castro, P. Sivac, and E. Benzi, "The Alphasat Aldo Paraboni scientific

- experiment: An overview of the activities of the European Space Agency,” *2016 10th Eur. Conf. Antennas Propagation, EuCAP 2016*, pp. 1–4, 2016, doi: 10.1109/EuCAP.2016.7482019.
- [44] J. A. Nessel, R. J. Acosta, and F. A. Miranda, “Preliminary experiments for the assessment of V/W-band links for space-earth communications,” *IEEE Antennas Propag. Soc. AP-S Int. Symp.*, pp. 1616–1617, 2013, doi: 10.1109/APS.2013.6711467.
- [45] ASI, “Coordinamento Esperimento di Propagazione Italsat (CEPIT).” <http://ieiit-cnr.dei.polimi.it/cptpage/>.
- [46] A. Sbardellati and O. Alberti, “The 20, 40, 50 GHz Propagation Beacon,” *Riv. Tech. Selenia*, vol. 3, no. 4, 1990.
- [47] ESA, “N° 40–1993: OLYMPUS: End of mission,” 1993. [https://www.esa.int/Newsroom/Press\\_Releases/OLYMPUS\\_End\\_of\\_mission](https://www.esa.int/Newsroom/Press_Releases/OLYMPUS_End_of_mission).
- [48] B. R. Arresser-Rastburg and G. Brussaard, “Propagation Research in Europe Using the OLYMPUS Satellite,” *Proc. IEEE*, vol. 81, no. 6, pp. 865–875, 1993, doi: 10.1109/5.257700.
- [49] ESA, “Alphasat payload honours Aldo Paraboni,” 2013. [https://www.esa.int/Applications/Telecommunications\\_Integrated\\_Applications/Alphasat/Alphasat\\_payload\\_honours\\_Aldo\\_Paraboni](https://www.esa.int/Applications/Telecommunications_Integrated_Applications/Alphasat/Alphasat_payload_honours_Aldo_Paraboni).
- [50] T. Rossi *et al.*, “Satellite communication and propagation experiments through the alphasat Q/V band aldo paraboni technology demonstration payload,” *IEEE Aerosp. Electron. Syst. Mag.*, vol. 31, no. 3, pp. 18–27, 2016, doi: 10.1109/MAES.2016.150220.
- [51] ESA, “Alphasat Hosted Payloads Workshop,” no. June. 2011.
- [52] J. E. Allnut, *Satellite-to-Ground Radiowave propagation*. 2011.
- [53] ITU-R, “Attenuation by atmospheric gases and related effects Series Radiowave propagation,” *Recomm. ITU-R P.676-12*, 2019, [Online]. Available: [https://www.itu.int/dms\\_pubrec/itu-r/rec/p/R-REC-P.676-12-201908-!!!PDF-E.pdf](https://www.itu.int/dms_pubrec/itu-r/rec/p/R-REC-P.676-12-201908-!!!PDF-E.pdf).
- [54] ITU-R, “Attenuation due to clouds and fog,” *Reccomendation ITU-R P.840-8*, pp. 1–6,

2019.

- [55] ITU-R, "Specific attenuation model for rain," *Rec. ITU-R P.838-3*, pp. 1–8, 2005.
- [56] C. Capsoni, L. Luini, A. Paraboni, C. Riva, and A. Martellucci, "A new prediction model of rain attenuation that separately accounts for stratiform and convective rain," *IEEE Trans. Antennas Propag.*, vol. 57, no. 1, pp. 196–204, 2009, doi: 10.1109/TAP.2008.2009698.
- [57] ITU-R, "Propagation data and prediction methods required for the design of Earth-space telecommunication systems," *Recomm. ITU-R P.618-13*, vol. 12, pp. 1–24, 2015.
- [58] H. W. Arnold and D. C. Cox, "Dependence of Depolarization on Incident Polarization for 19-GHz Satellite Signals," *Bell Syst. Tech. J.*, vol. 57, no. 9, pp. 3267–3276, 1978, doi: 10.1002/j.1538-7305.1978.tb02203.x.

## Chapter 2

# 2 Three-Band Geostationary Satellite Beacon Payload for Propagation Experiments in Europe

### 2.1 Introduction

Propagation experiments and subsequent studies have been performed to measure, characterize and model to some extent the propagation effects on earth-space paths globally [1]–[4]. These efforts have been directed towards the requirements of professional communications (e.g. broadcasting), predicting parameters such as link availability over a year or a worst month [5]. Previously, Europe has benefited from two major propagation experiments, the ESA OLYMPUS satellite and the Italian ITALSAT F1 satellite at Ku/Ka and Q/V-bands respectively. Lately, the ongoing Alphasat TDP5 payload at Ka/Q-band has allowed for an extensive network of propagation terminals across Europe concurrently measuring the propagation effects. This has allowed for the collection of relevant propagation data in these frequency bands [6]. These studies have been fundamental in providing the basic knowledge on the physical aspects governing the radio-wave propagation in slant path. An example of the comparative levels of attenuation experienced at Ku-, Ka- and Q/V frequency band as measured in southern England during the OLYMPUS and ITALSAT propagation campaigns can be found in [6].

Undesired propagation effects are magnified at high frequencies. For instance, one of the main problems of the exploitation of W-band is radio wave propagation through the atmosphere of the Earth and the fundamental lack of understanding of these effects, even in clear sky conditions, with regards to proper system design and fade mitigation.

The first order propagation impairments at W-band are gaseous, cloud and rain attenuation, scintillation, depolarisation and atmospheric noise. Gaseous attenuation is always present. Cloud attenuation is more significant than at Ka-band and increases as the elevation decreases. Studies have shown [7] that cloud attenuation with respect to the intensity of the attenuation and its duration depends on the type of cloud (e.g. stratiform,

convective) and consequently on the season (more convective cloud in the summer) and the geographic region (more stratiform cloud in the north of Europe compared with the south of Europe). Rain attenuation is the dominant loss mechanism which depends on the climatic region and of course the type of rain (e.g. stratiform, convective). For a given availability, rain attenuation can lead to unrealistic margin requirements and make the deployment of propagation impairment mitigation techniques compulsory. Scintillation is caused by rapid fluctuations in the refractive index of the atmosphere. Scintillation effects occur on time scales under  $\sim 0.5$  seconds and limit the performance of high data rate and complex modulation systems. Depolarisation for frequency reuse systems is important to characterise signal leakage between polarisations of the same signal via simultaneous co-polarisation and cross-polarisation measurements. These are commonly caused by non-spherical raindrops and ice crystals in the troposphere. Atmospheric noise must be considered for calculation of the down-link carrier to noise ratio.

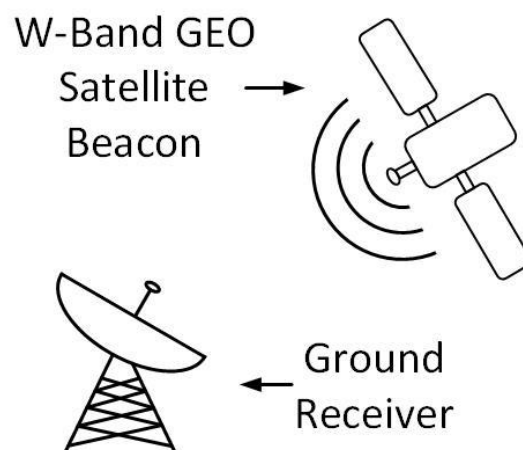


*Figure 2-1: W-band GEO satellite beacon and ground receiver.*

To perform the study, a geostationary (GEO) satellite at W-band (76 GHz) with European coverage and a ground receiver are required as shown in Figure 2-1. With the launch of a GEO satellite campaign at W-band, multiple ground terminals can operate across Europe and study the propagation impairments. ESA issued a tender as a first step of realising such a campaign under the title: “W-Band Technology Developments Towards First Beacon-Based Propagation Campaign” and in 2016 the consortium consisted of RAL-Space, Heriot-Watt University and ViperRF. RAL-Space was responsible for the project management, and design and simulation of the ground receivers. Heriot-Watt University was responsible for the design and simulation of the satellite payload. ViperRF



was responsible for the design, manufacturing and testing of the W-band MMICs (LNA and HPA). During the study, technological constraints and future work were also identified and reported. The chapter demonstrates Heriot-Watt University work during the development of the satellite payload. In particular, the design and simulation of the payload up-converter chains, and future work to be done ahead of the campaign.

The remainder of the chapter is organised as follows. Section 2.2 outlines the beacon design requirements. Section 2.3 presents the beacon design including upconverter simulations and analysis. Section 2.4 presents the compliance matrix of the beacon payload. Section 2.5 presents future work that needs to be addressed ahead of the campaign. Finally, conclusions are presented in Section 2.6.

## 2.2 Beacon Design Requirements

The design of the beacon payload was based on ESA requirements.

### 2.2.1 Operating Frequencies

The beacon shall be able to transmit a continuous wave (CW) at the following frequencies:

*Table 2-1: Beacon Frequency Plan*

Frequency	Band
19 GHz	Ka-Band
38 GHz	Q-Band
76 GHz	W-Band

### 2.2.2 Signal Polarisation

The beacon shall have the following polarisation:

*Table 2-2: Beacon Polarisation*

Frequency	Band	Proposed Polarisation
19 GHz	Ka-Band	Linear Polarised
38 GHz	Q-Band	Linear Polarised
76 GHz	W-Band	Circular Polarised

### 2.2.3 Coverage Area

The beacon coverage will include the whole of Europe. Figure 2-2 represents the W-Band coverage according to the 10°E GEO location. It is noted that European & Tropical coverage had been considered with penalties on the margin, mass and DC power consumption.

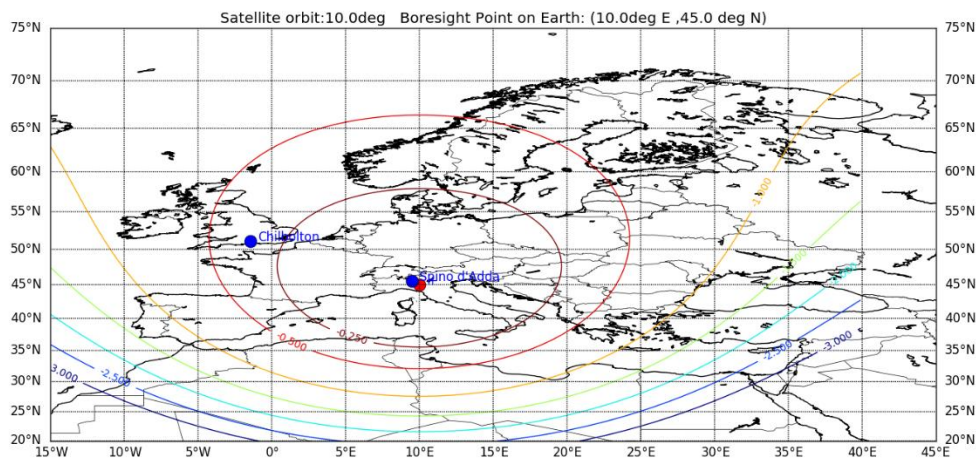


*Figure 2-2: W-Band coverage when geostationary satellite is at 10° East*

#### 2.2.4 Effective Isotropic Radiated Power (EIRP)

The EIRP in dBm is calculated following (3.1).

$$EIRP = P_{TX} - L_{feed} + G_{ant} \text{ (dBm)} \quad (3.1)$$

where  $P_{TX}$  is the power output in dBm of the transmitter chain ahead of the antenna,  $L_{feed}$  are feed losses in dB and  $G_{ant}$  is the antenna gain in dBi. The minimum beacon EIRPs are as per Table 2-3.

*Table 2-3: Beacon EIRP*

Frequency	Band	EIRP (dBm)
19 GHz	Ka-Band	59.4
38 GHz	Q-Band	58.9
76 GHz	W-Band	52.3

#### 2.2.5 Phase Noise

The beacon shall have a minimum phase noise mask as specified in Table 2-4.

*Table 2-4: Phase Noise Mask*

Freq offset (Hz)	Ka band (dBc)	Q band (dBc)	W band (dBc)
10	-30	-22	-14
100	-50	-42	-34
1k	-60	-52	-44
10k	-70	-62	-54
100k	-90	-82	-74
>100k	-90	-82	-74

### 2.2.6 Beacon Lifetime

The lifetime shall be a minimum of 5 years for evaluated reliability better than 95%.

### 2.2.7 Mass

The total beacon mass shall be less than 50 kg.

### 2.2.8 DC Power Consumption

The total DC power consumption shall be less than 150W.

### 2.2.9 Telemetry, Tracking and Control (TT&C) Operations

The beacon shall benefit from TT&C support for equipment configuration and redundancy switching

## 2.3 Beacon Design

Within this section the up-converter architecture, payload redundancies, achieved EIRP and EIRP margins, phase noise, mass, DC power consumption and TT&C operations of the payload are shown.

### 2.3.1 Up-converter Architecture

A schematic representation of the proposed beacon is shown in Figure 2-3. The Ka-band, 19 GHz signal is produced using a mixer and two phase locked dielectric resonator oscillators at 1.5 GHz and 17.5 GHz. The output from the mixing stage,  $f_{RF}$ , was calculated using equation (2.1):

$$f_{RF} = f_{IF} + f_{LO} \quad (2.1)$$

where  $f_{IF}$  and  $f_{LO}$  represent the intermediate (1.5 GHz) and local oscillator (17.5 GHz) frequency respectively. The oscillators used are locked with an ultra-stable and low noise master oscillator.

A waveguide band pass filter is used to filter harmonic products from the mixing stage. A 2-way splitter is used to branch the beacon to the Q-band section where a frequency doubler is deployed along with a waveguide band pass filter. The architecture is once again branched out to the W-band chain via a coupler, where a frequency doubler generates the 76 GHz signal and a waveguide passband filter filters unwanted harmonics and spurious. Furthermore, a waveguide polariser provides the W-band section's circular polarisation. The appropriate driver amplifiers and high power amplifiers (HPA) are used for each frequency chain in order to achieve the desired EIRP. In each frequency chain, two HPAs are connected to single pole double throw (SPDT) switches (SKa1SKa2, SQ1-2 and SW1-2) and only one of the two is active during operation while the other is a redundancy.

In the baseline solution presented here, the Ka-Band signal is produced using a mixer and two oscillators operating at 1.5 GHz and 17.5 GHz respectively. This is to provide some flexibility in terms of the frequency generation, e.g. considering the dual frequency dual polarisation solution presented in Section 3.3.6. If this solution is not adopted, it is probably simpler to substitute this assembly with single source at 19 GHz.

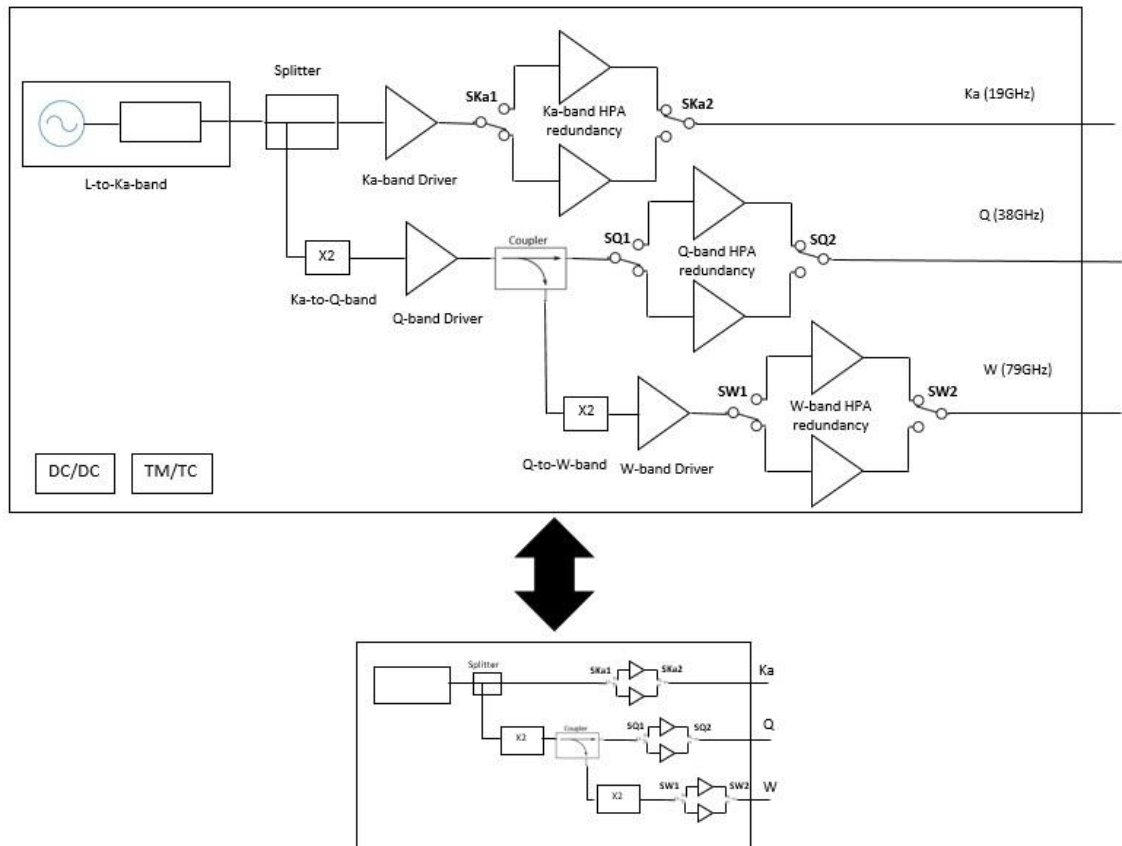
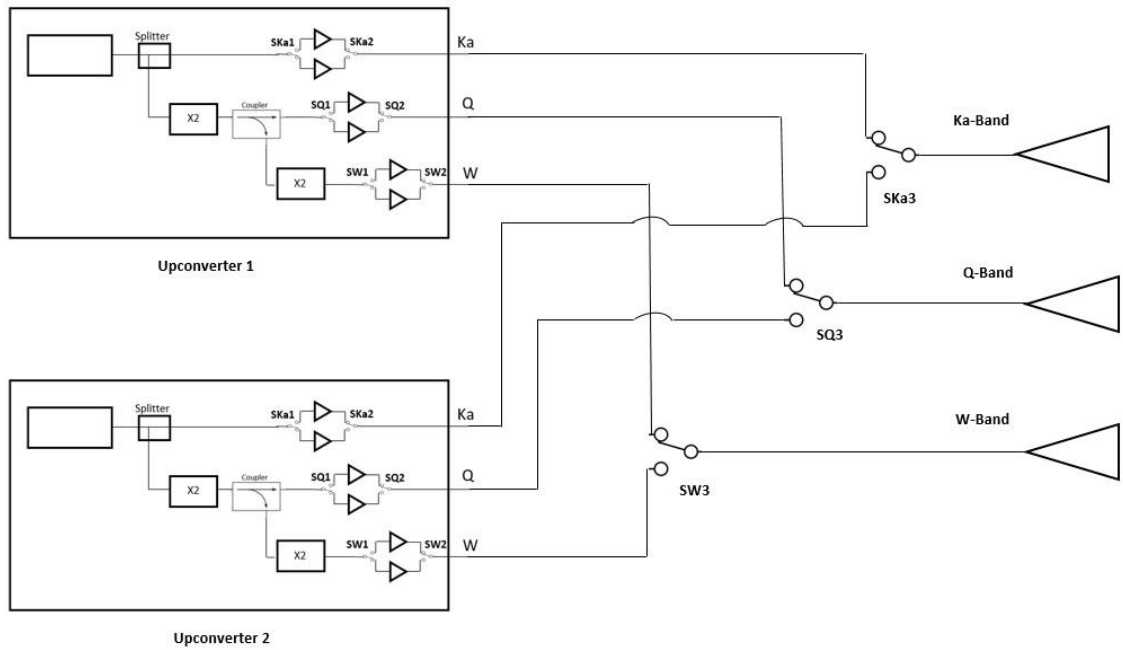


Figure 2-3: Schematic representation of the proposed up-converter.

### 2.3.2 Architecture for Reliability and Redundancy

The satellite beacon benefits from two up-converter redundancies allowing for a total of 64 configuration paths. The two up-converter chains are connected to the equivalent antenna with the use of SPDT switches (Ska3, SQ3, SW3). This would guarantee the 5 year and 95% reliability of the beacon payload. In Figure 2-4, the described architecture of the up-converter with the HPA redundancies and up-converter redundancy is shown.



*Figure 2-4: Schematic representation of the beacon with the two up-converter redundancies and routing to equivalent antennas.*

### 2.3.3 Payload Up-conversion Chains

Within this section, the simulated architectures for the three-frequency beacon with European only coverage is presented. Furthermore, graphs of the simulated channel power, compression and spectrum are presented along with a list of components and link budget margins. The ADS SystemVue software by Keysight was used during the simulation of the payload up-converter chains.

### 2.3.4 Ka-band Conversion Chain

Figure 2-5 shows the two oscillators (at 1.5 GHz and 17.5 GHz) and mixer in order to produce the RF signal at 19 GHz (Ka-band), the 500 MHz bandwidth bandpass filter and the splitter that leads to the Q-band chain.

Figure 2-6 includes an OMMIC driver amplifier along with a coupler for the automatic level control (ALC) mechanism and the HPAs redundancy switch. Figure 2-7 includes an HPA by Analog Devices along with its packaging losses.

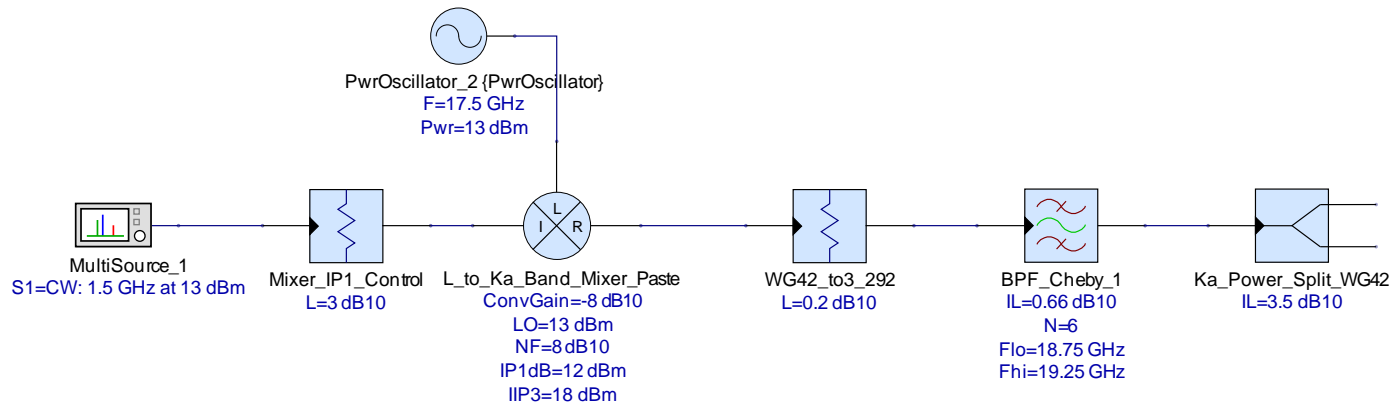


Figure 2-5 Ka-Band up-conversion chain up to Q-Band power splitter (Single HPA)

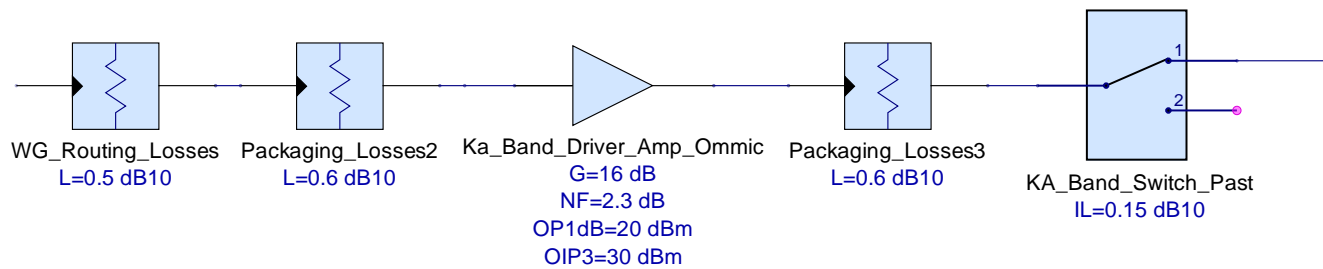


Figure 2-6: Ka-Band driver, ALC coupler and redundancy switch (Single HPA)



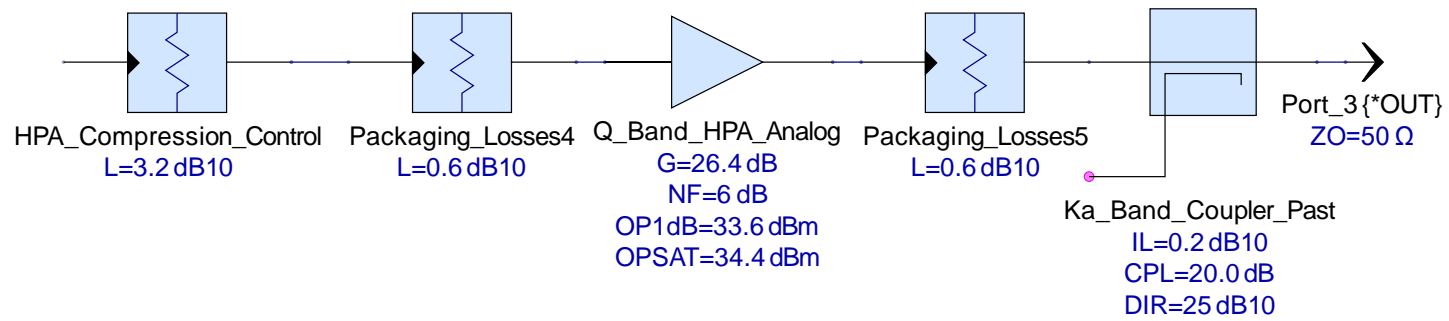


Figure 2-7: Ka-Band Single HPA

It is noted that a number of attenuators are used in Figure 2-5, Figure 2-6 and Figure 2-7. This is to account for ohmic losses associated with [8]:

WG-to-Coaxial Transition: 0.2 dB

Coaxial-to-microstrip: 0.15 dB

Microstrip losses: 0.10 dB

Microstrip – MMIC bonding: 0.15 dB

Total losses at the RF input and output: 0.6 dB

Table 2-5 is a list of the Ka-Band components used along with their DC power consumption, source voltage, mass and power dissipation. The total DC power consumption is 30 W while the mass is 3 kg, excluding the ALC mechanism variable attenuator, variable gain amplifier and power detector (discussed in Section 2.3.4).

*Table 2-5: Ka-Band (single HPA) component list, DC Power consumption and mass. (highlighted fields depict assumed values).*

Supplier	Category	Model	DC Power Consumption (W)	Mass (gr.)
Spectratime	Ref. Oscillator	iSpace+ MO	3.5	220
Microwave Dynamics	Oscillators	PLO-5200	4.8(2.4 each)	160
Pasternack	Mixer	PE86X1004	n/a	36.3
Millitech	BPF	Custom	n/a	120
Pasternack	Coupler	PE-W42CP002-20	n/a	250
Pasternack	Magic Tee	PEWMT1006	n/a	78
OMMIC	Driver Amp.	CGY2141UH/C1	0.9	150
Analog Devices	HPA	HMC6981LS6	20.6	400 (200gr. each)
Pasternack	Switch	PEWGS6006	18.72 (9.36)	1449 (483gr. each)
Millitech	Horn Antenna	Custom	n/a	60
Assumed Value		<b>Total:</b>	29.8	2923.3

### 2.3.5 Q-band Conversion Chain

Figure 2-8 shows a Pasternack frequency doubler along with routing and waveguide to coaxial losses, a 500 MHz bandwidth bandpass filter, an OMMIC driver (along with its packaging losses), the coupler for the ALC mechanism and the coupler that leads to the W-band chain. Figure 2-9 shows the HPAs redundancy switch along with the splitters and the ERZIA HPA with the coaxial to waveguide losses.

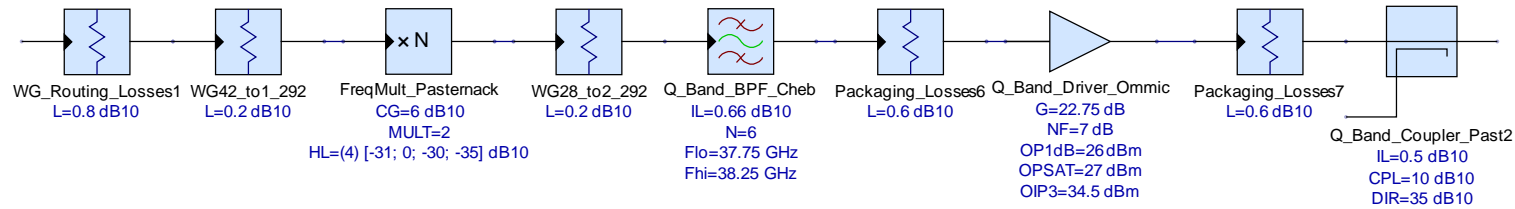


Figure 2-8: Q-Band frequency doubler, filter, driver amplifier and chain branch coupler

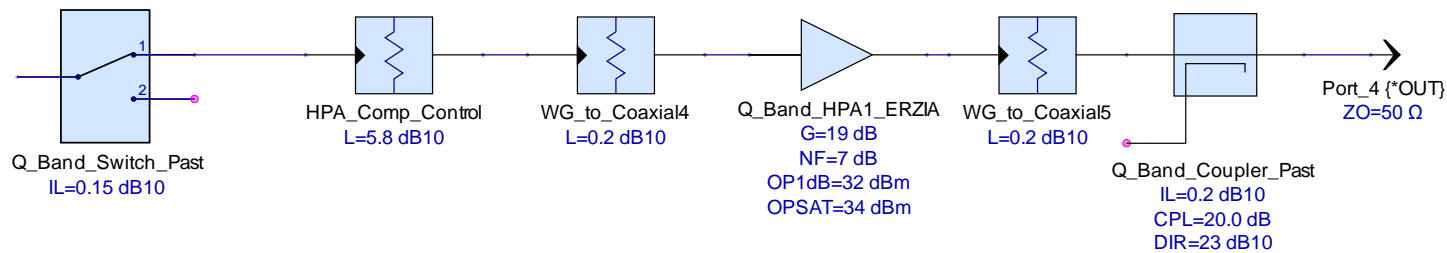


Figure 2-9: Q-Band redundancy switch and single HPA

A number of attenuators can be observed in Figure 2-8 and Figure 2-9. These attenuators have been put in place to simulate the transition losses from waveguide to 2.92mm (Female)/2.4mm (Female)/SMA (Female) as well as packaging losses, which have been modelled according to [8]. Furthermore, the attenuators immediately after the magic tee (splitting the 19 GHz and 38 GHz signal) have been placed in order to simulate waveguide routing losses. The attenuators placed at the RF input of the HPA serve as routing losses as well as, controlling the operating point of the amplifier.

The modelled losses during the simulation were the following [8]:

WG42-to-Coaxial Transition (2.92mm): 0.2 dB

Coaxial-to-microstrip: 0.15 dB

Microstrip losses: 0.10 dB

Microstrip – MMIC bonding: 0.15 dB

Total losses at RF input and output: 0.6 dB

Table 2-6 is a list of the Q-band components used along with their DC power consumption, input voltage, mass and power dissipation. The total DC power consumption is at 22 W while the mass is at 2.8 kg, excluding the ALC mechanism variable attenuator, variable gain amplifier and power detector.

Table 2-6: Q-Band (single HPA) component list, DC Power consumption and mass.  
(highlighted fields depict assumed values).

Supplier	Category	Model	DC Power Consumption (W)	Mass (gr.)
Pasternack	Freq. Multiplier	PE88XX2002	0.35	40
Millitech	BPF	Custom	n/a	80
OMMIC	Driver Amp.	CGY2130UH/C1	3.915	150
Pasternack	Coupler	PE-W28CP003-20	n/a	200
Pasternack	Coupler	PE-W28CP003-10	n/a	200
ERZIA	HPA	ERZ-HPA-3000-4000-32	17	400 (200gr. each)
Pasternack	Switch	PEWGS6002	16.54 (8.28W each)	1362 (454gr. each)
Millitech	Horn Antenna	Custom	n/a	60
Assumed Value		<b>Total:</b>	21.265	2712

### 2.3.6 W-band Conversion Chain

Figure 2-10 contains a UMS frequency doubler along with some routing and packaging losses, a 500 MHz bandwidth bandpass filter, the coupler for the ALC mechanism, the HPAs redundancy switches, the ViperRF HPA and the polariser for a circular polarisation.

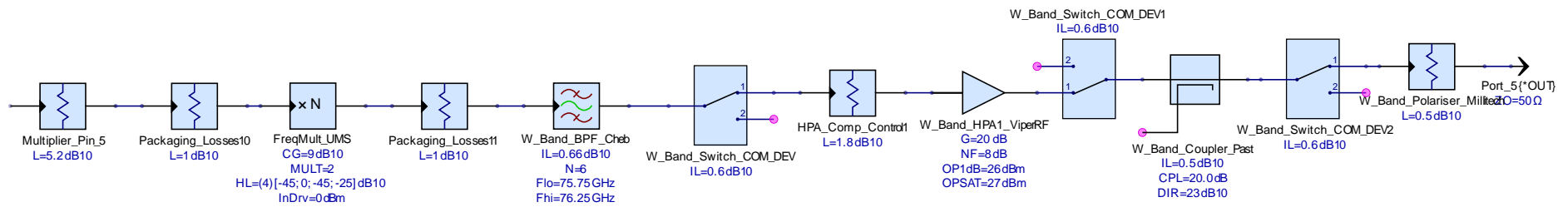


Figure 2-10: W-Band up-conversion chain with single HPA

A number of attenuators can be observed in Figure 2-10. These attenuators have been put in place to simulate packaging losses for the UMS frequency doubler, which is available in die form. At 76 GHz the packaging losses have been simulated as 1 dB at the RF input and output port. Furthermore, in order to simulate the frequency doubler as realistically as possible, an attenuator was placed in order to reduce the power at the RF input port and achieve an RF power output of 13 dBm which is a typical value. This attenuator can also be thought as routing losses.

Table 2-7 is a list of the W-band components used along with their DC power consumption, input voltage, mass and power dissipation. The total DC power consumption is 13W while the mass is 1.3 kg, excluding the ALC mechanism variable attenuator, variable gain amplifier and power detector (see also Section 3.3.4).

*Table 2-7: W-Band (single HPA) component list, DC Power consumption, and mass. (highlighted fields depict assumed values).*

Supplier	Category	Model	DC Power Consumption (W)	Mass (gr.)
UMS	Freq. Multiplier	CHU2277	1.8	60
Millitech	BPF	Custom	n/a	50
Pasternack	Coupler	PE-W12CP003-20	n/a	120
ViperRF	HPA	Custom	5	200 (100gr. each)
COM DEV	Switch	Custom	N/A	120 (40gr. each)
Millitech	Polariser	POL-12-R1251	n/a	50
Millitech	Horn Antenna	Custom	n/a	50
Assumed Value		<b>Total:</b>	6.8	640

### 2.3.7 Simulation Graphs: Output Power, Compression Points and Spectrum

The total upconverter gain,  $G_{Fout}$ , of each frequency chain was calculated using (2.2):

$$G_{Fout} = G_{out1} + \dots + G_{outN} \quad (2.2)$$

where  $G_{outN}$ , is the gain of each stage and subscript  $N$  is the number of total components in the upconverter chain.

The compression point, of the non-linear devices such as mixers and amplifiers is depicted in the y-axis of Figure 2-12, Figure 2-15 and Figure 2-18. For example, in Figure 2-12 the driver amplifier, node 12, is operating at a compression point of 0.135 dB.

### 2.3.7.1 Ka-band Conversion Chain

The simulated channel power of the Ka-band chain is 31.8 dBm, as shown in Figure 2-11.

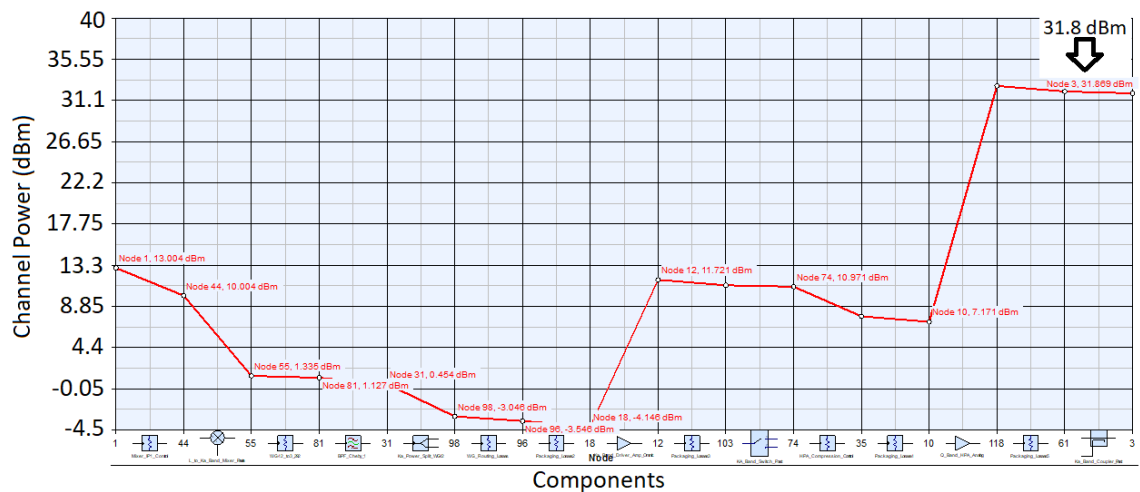


Figure 2-11: Ka-band Channel Power (Single HPA)

The simulated compression point of the Ka-band HPA is 1 dB as can be seen from Figure 2-12.

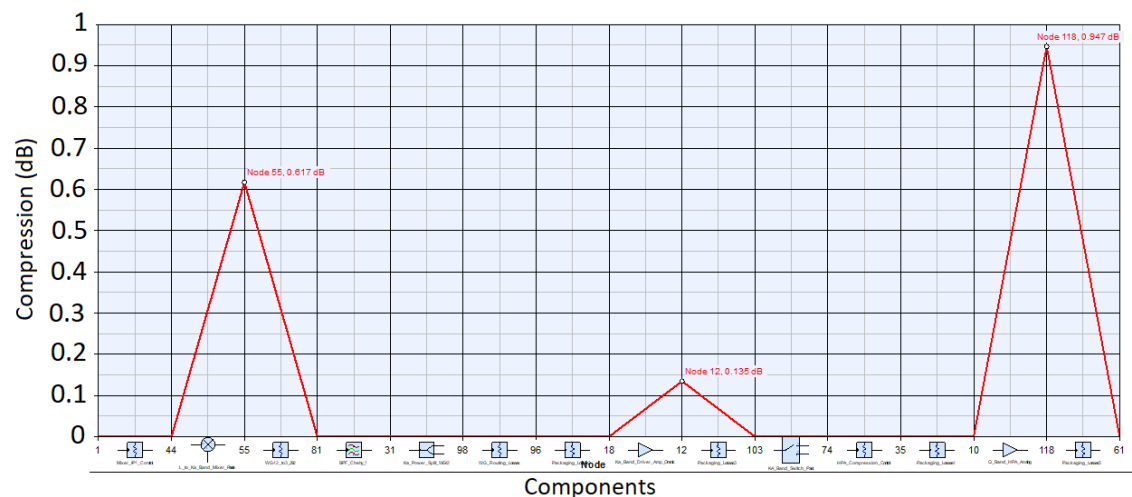


Figure 2-12: Ka-band Compression Point (Single HPA)

Figure 2-13 is the simulated output spectrum of the Ka-band conversion chain.



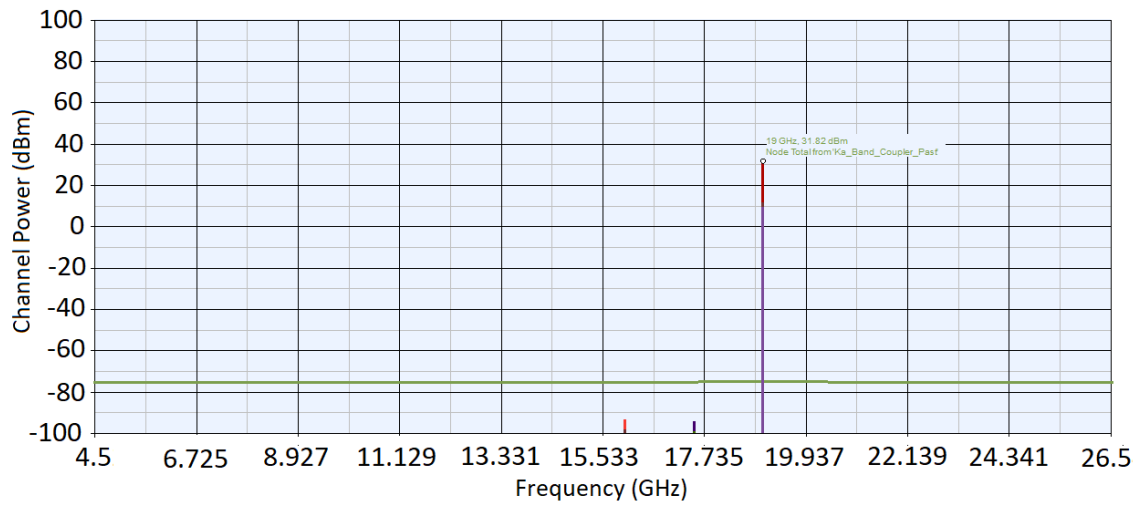


Figure 2-13: Ka-band Spectrum (Single HPA)

### 2.3.7.2 Q-band Conversion Chain

The simulated channel power of the Q-band chain is 31.8 dBm, as can be seen in Figure 2-14.

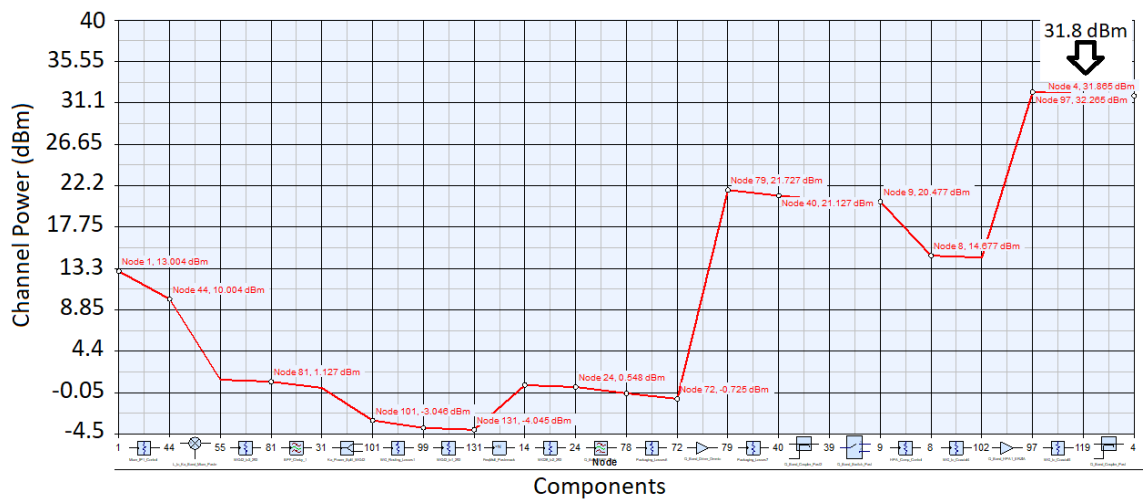


Figure 2-14: Q-band Channel Power (single HPA)

The simulated compression point of the Q-band HPA is 1.3 dB as can be seen from Figure 2-15.

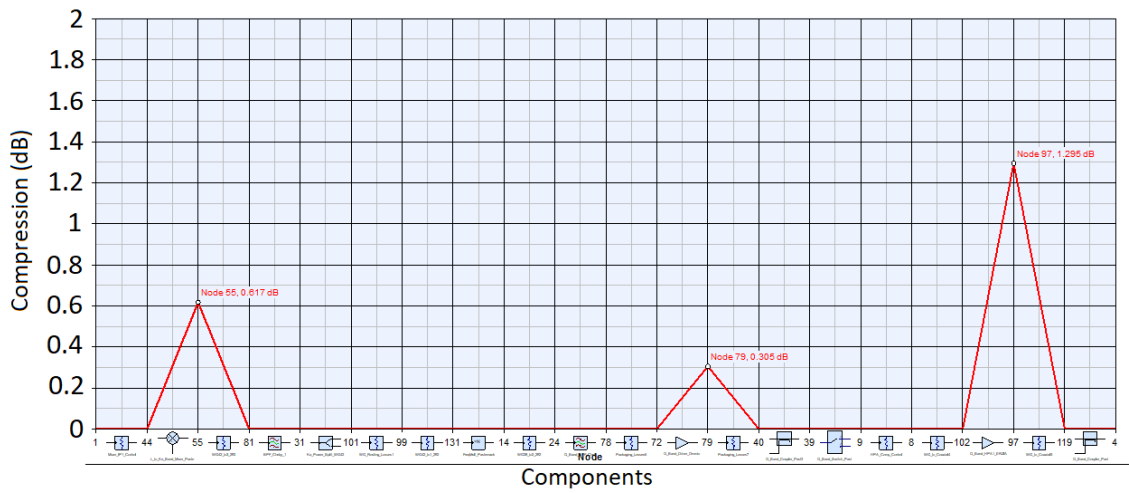


Figure 2-15: Q-band Compression Point (single HPA)

Figure 2-16 is the simulated output spectrum of the Q-band conversion chain.

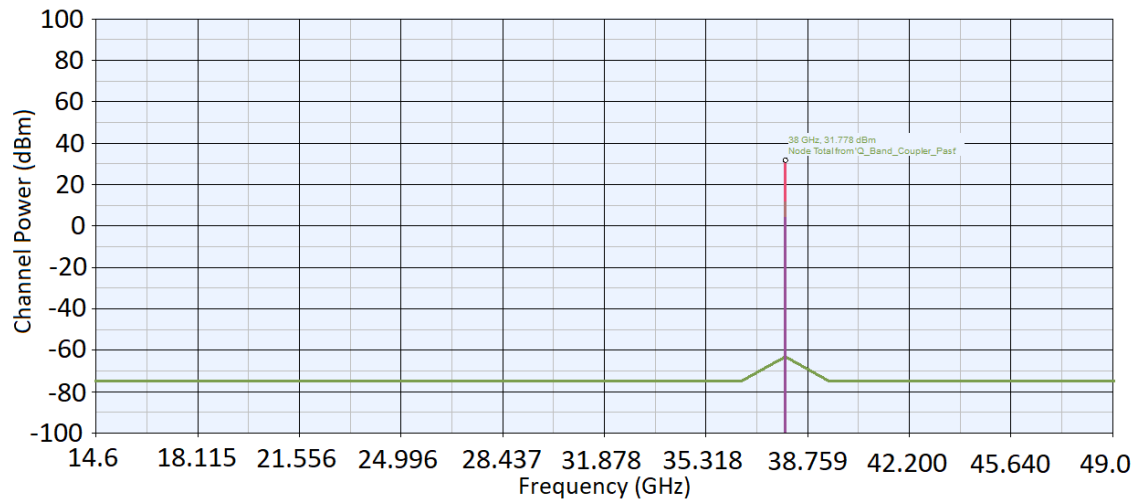


Figure 2-16: Q-band Spectrum (single HPA)

### 2.3.7.3 W-band Conversion Chain

The simulated channel power of the W-band chain is 24.7 dBm, as can be seen from Figure 2-17.

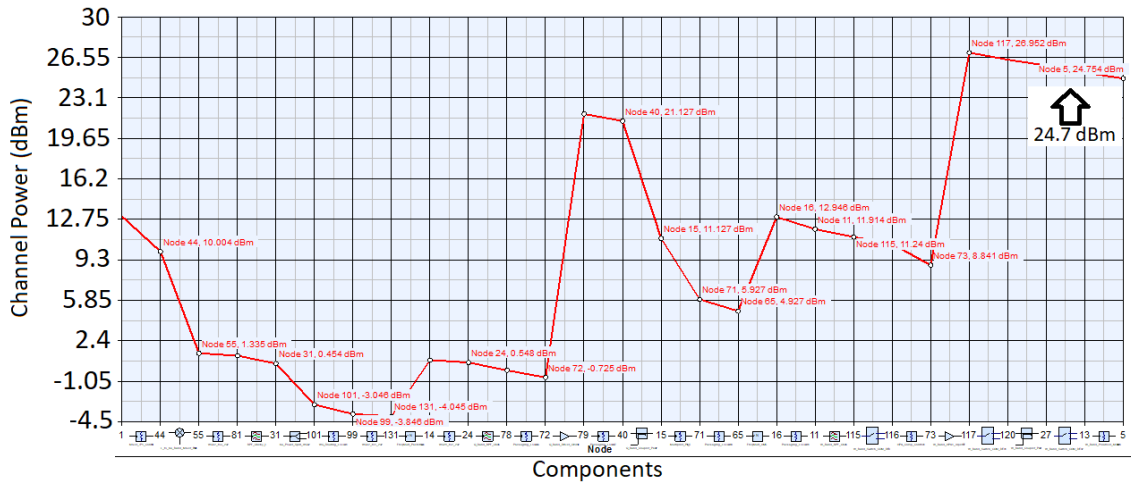


Figure 2-17: W-band channel power (single HPA)

The simulated compression point of the custom W-band HPA is 2 dB as can be seen from Figure 2-18.

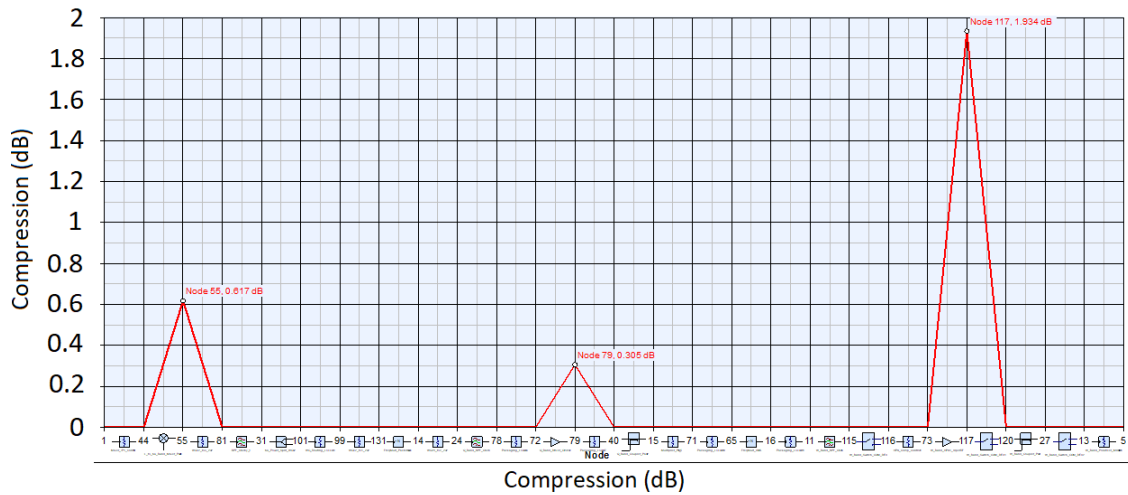


Figure 2-18: W-band compression point (single HPA)

Figure 2-19 is the simulated output spectrum of the W-band conversion chain.

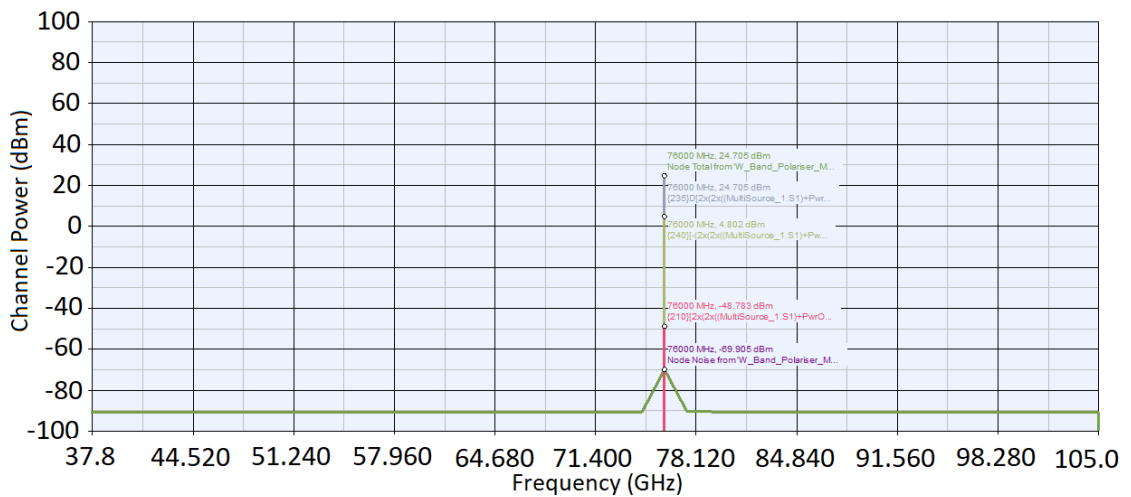


Figure 2-19: W-Band Spectrum (single HPA)

### 2.3.8 Gain Stability

A common practise for RF power fluctuations is the use of an ALC or AGC (automatic gain control). The simplest form of an ALC is shown in Figure 2-20. An ALC functions with a feedback loop where the RF power from the driver amplifier is measured and the ALC loop then controls the variable attenuator and variable gain amplifier (VGA). Through this feedback loop, the RF power output is kept constant. The same concept can be applied to the HPA but the implications faced are the high power that the mechanism has to deal with. Therefore, one approach is to apply the ALC mechanism prior to the HPA. In this case the HPA's drain voltage is monitored and readjusted in order to compensate for any temperature drifts.

However, if the final amplification stage operates at a higher compression point, then adjusting the drain voltage will control the gain in a non-linear manner. Moreover, if the final stage internally involves several amplification stages, then there are additional inaccuracies in the loop. In these cases, it is also possible to sample the output signal strength at the output of the final stage and feed that into a control loop in order to stabilise the gain. This is the approach proposed here, which will require sampling and power sensing at the output of the final HPA stage. It is noted that this approach will impose some additional but small penalty on the final RF power due to the presence of the coupler.

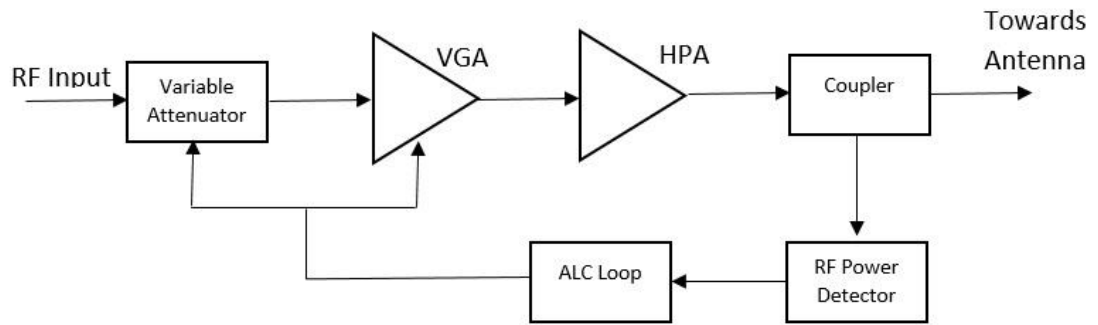


Figure 2-20: ALC Mechanism

As shown from the earlier sections, the coupler shown in Figure 2-20 is incorporated into the simulation designs for the different frequency chains (Figure 2-6, Figure 2-9 and Figure 2-10). The missing components for a complete ALC mechanism are the detectors, variable attenuators and variable gain amplifiers which are presented in the following sub-sections. The rest of this section discusses options for these components across the three bands of interest.

### 2.3.8.1 Ka-band

For the Ka-Band, the following components in Table 2-8 are available on the market:

Table 2-8: Ka-Band ALC mechanism components

Supplier	Type	Model	Dynamic Range (dB)	DC Power (Watts)	Voltage Source (V)
UMS	Detector	CHE1270a98F	30	0.4	4.5
Pasternack	Variable Atte.	PE70A1017	26	0.15	-5 and 5 and -2.9 to 0
Analog	VGA	HMC997LC4	14	1	5 and -2 to 0

The components on Table 2-8 can be used for constructing the ALC mechanism. Only the variable attenuator from Pasternack is space qualified while the detector and VGA are

GaAs devices that can be space qualified in the future. An alternative option for the variable attenuator is the CHT4690-QAG from UMS which is also utilises a GaAs MMIC design.

#### 2.3.8.2 Q-band

For the Q-Band, the following components in Table 2-9 are available on the market:

*Table 2-9: Q-Band ALC mechanism components*

<b>Supplier</b>	<b>Type</b>	<b>Model</b>	<b>Dynamic Range (dB)</b>	<b>DC Power (Watts)</b>	<b>Voltage Source (V)</b>
UMS	Detector	CHE1270a98F	30	0.4	4.5
UMS	Variable Atte.	CHT4699-QDG	30	N/A	-5 to 0
OMMIC	Driver	CGY2141UH/C1	N/A	0.8	5

For the Q-Band, a VGA was not identified. Since the UMS variable attenuator has a dynamic range of 30 dB, another OMMIC driver amplifier can be added in order to counter the attenuation. The detector and variable attenuator from UMS are GaAs devices that can be space qualified in the future.

### 2.3.8.3 W-Band

For the W-Band, the following components in Table 2-10 are available on the market:

*Table 2-10: W-Band ALC mechanism components*

Supplier	Type	Model	Dynamic Range (dB)	DC Power (Watts)	Voltage Source (V)
Analog Devices	Detector	HMC7447	24	Passive	n/a
Gotmicc	Variable Atte.	gSSS015	25	N/A	-1.2 to 0
Analog Devices	VGA	HMC8120	15	1	4 and -5 to -1

The components are not space qualified but since they are GaAs devices, they can be space qualified in the future. An alternative option for the detector is the Gotmicc gDPZ0011 B and a VCA series Millitech variable attenuator can also be used

### 2.3.9 Link Budgets and Margins

The link budgets and margins achieved by the Ka-, Q- and W-band chains are presented in Table 2-11, Table 2-12 and Table 2-13 respectively. The baseline values have been provided for a ground station located in Chilbolton, UK with a dynamic range of >30 dB for all frequencies. The current feed losses which include 2 SPDT electromechanical switches for the Ka- and Q-band chains are quoted by Pasternack. Furthermore, a best-case scenario for the beacon coverage included some of the Tropics. Due to power consumption and mass restrictions, a European only coverage was more feasible. Therefore, the Millitech quoted antennas have a smaller beam width but higher gain.

Table 2-11 reports an EIRP margin of 1.25 dB for the Ka-Band solution. Table 2-12 reports an EIRP margin of 1.6 dB for the Ka-band solution.

Table 2-13 reports an EIRP margin of 1.1 dB for the W-band solution.

Table 2-11: Ka-band initial link budget and margins achieved from simulations

	DD05 - Link Budget		Values from the design process	
TX Frequency	19 GHz		19 GHz	
PA Output Power	33 dBm		31.8 dBm	Channel power achieved
Feed Loss	1 dB	PA redundancy switch plus routing.	0.65	0.3 dB switch IL and another 0.35 dB for routing
TX antenna Gain and 3 dB beam width Coverage	27.4 dBi 7.89° (EU & TC)	14cm diameter 70% Illumination efficiency	29.5 dBi 6.14° (EU)	18 cm diameter 70% illumination efficiency
EIRP on boresight	59.4dBm		60.65 dBm	Achieved EIRP on boresight
Margin			<b>1.25 dB</b>	1.05 dB Margin with Isolator (0.2 dB)



Table 2-12: Q-band initial link budget and margins achieved from simulations

	DD05 - Link Budget		Values from the design process	
TX Frequency	38 GHz		38 GHz	
PA Output Power	33 dBm		31.8 dBm	Channel power achieved
Feed Loss	1.5 dB	PA redundancy switch plus routing.	0.8	0.3 dB switch IL and another 0.5 dB for routing
TX antenna Gain and 3 dB beam width Coverage	27.4 dBi 7.89° (EU & TC)	7cm diameter 70% Illumination efficiency	29.5 dBi 6.14° (EU)	9 cm diameter 70% Illumination efficiency
EIRP on boresight	58.9dBm		60.5 dBm	Achieved EIRP on boresight
Margin			<b>1.6 dB</b>	1.35 dB Margin with Isolator (0.25 dB)

Table 2-13: W-Band initial link budget and margins achieved from simulations

	DD05 - Link Budget		Values from the design process	
TX Frequency	76 GHz		76 GHz	
PA Output Power	27 dBm		24.7 dBm	Output at the Polariser
Feed Loss	2.3 dB	1.3 dB for switch & 1 dB for OMT loss	0.8	0.8 dB routing (No OMT used)
TX antenna Gain and 3 dB beam width Coverage	27.6 dBi 7.67° (EU & TC)	3.6cm diameter 70% Illumination efficiency	29.5 dBi 6.14° (EU)	4.5 cm diameter 70% Illumination efficiency
EIRP on boresight	52.3 dBm		53.4 dBm	Achieved EIRP on boresight
Margin			<b>1.1 dB</b>	0.6 dB Margin with Isolator (0.5 dB)

### 2.3.10 Dual Polarisation

The baseline polarisation solution states linear polarisation for the Ka- and Q-band and circular polarisation for the W-band. The architecture presented has accounted for the W-band circular polarisation (with the use of a waveguide polariser). In this section two polarisation schemes providing dual-polarisation for the W-band are investigated. In particular, section 2.3.10.1 deals with time switched dual linear polarisation while section 2.3.10.2 deals with the dual frequency dual linear polarisation.

#### 2.3.10.1 Time Switched Dual Polarisation (TSDP)

The design architecture for a TSDP scheme is shown in Figure 2-21. The difference between the circular polarisation and the dual linear (W-Band) is the use of another switch and an Orthogonal Mode Transducer (OMT) replacing the polariser. One aspect that should be taken into account is the switch that will be used in order to achieve this dual linear polarisation. The switch will be put under a considerable “stress” since it will require for a period of 5 years to switch  $> 6 \times 10^9$  and  $> 1.6 \times 10^9$  for a 40 Hz and 10 Hz switching rate respectively.

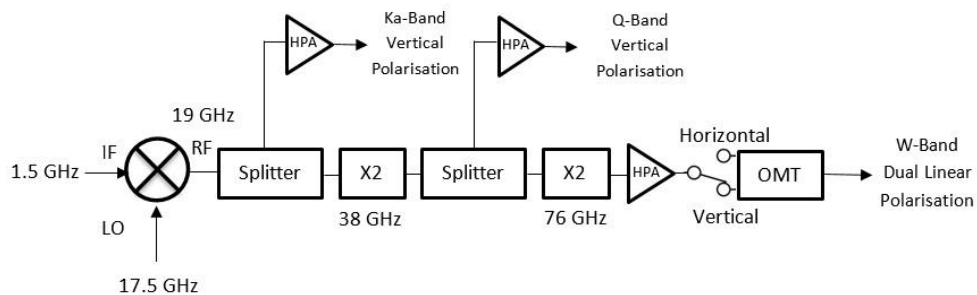
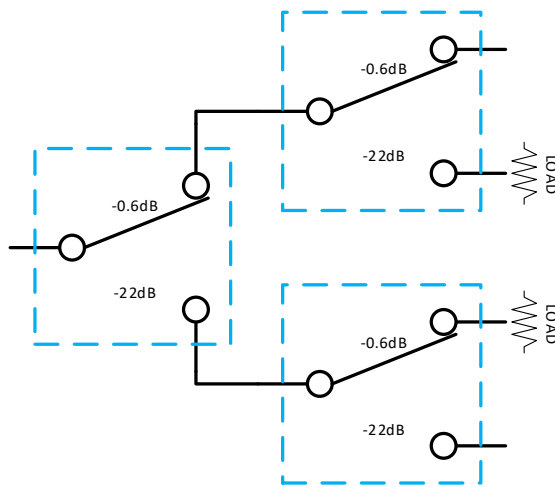


Figure 2-21: Time switched dual polarisation design outline

The current design uses a ferrite switch (at W-band) from COMDEV which provided an engineering model with quoted insertion losses of 0.6 dB over the temperature range, a minimum isolation of 22 dB, capable of handling a 2 W continuous wave power. A single switch will not provide the required  $> 35$  dB polarisation isolation so a set of three switches will be required. The outputs of the first switch drive the inputs of the other two

switches as shown in Figure 2-22. This produces 44 dB isolation at the cost of increased insertion loss.



*Figure 2-22: Polarisation Switch Matrix*

It is noted that ferrite technology appears advantageous for the time switched dual polarisation solution in terms of insertion loss (and possibly power) compared to PIN diodes and number of cycles compared to electromechanical switches.

In particular, it is noted that Pasternack provides high quality space qualified electromechanical switching technologies (which are proposed for the redundancy switching at Ka- and Q-band). They have excellent insertion losses (maximum value 0.15 dB) compared to ferrite (e.g. 0.6 dB quoted by COMDEV for W-band) and PIN diode (indicatively at 4 dB at lower frequencies) technologies. Pasternack does not supply an electromechanical switch at 76 GHz but even if it did, the lifetime of electromechanical switches is relatively low (250,000 cycles) and the switching speed is relatively slow (compared to ferrite and pin diode technologies). Alternatively, switches based on PIN diodes offer fast switching speed and high lifetime reliability. The downsides of the PIN diode switch are its power handling (usually around 0.5 W) and its insertion losses (> 4 dB typically at Q-Band). Using a PIN diode switch would degrade the EIRP drastically, having an impact on the dynamic range (degradation of S/N ratio). Therefore, the most viable option for the moment is ferrite switch technology. Further clarification is needed

from COM DEV in order to determine the lifetime and switching speed of the ferrite switch. It is noted that switched polarisation places significant challenges on the ground segment in relation to synchronisation requirements.

A suggestion from ESA was placing the switch ahead of the HPA as in Figure 2-23. The advantage of such a design is that the insertion losses introduced from a switch will not affect the EIRP margin. The disadvantage is the use of two HPAs in order to transmit on both horizontal and vertical polarisations. This can introduce uncertainties in the power levels transmitted for each polarisation. Additionally, this approach will impact the DC power budget, as well as the cost, mass and volume.

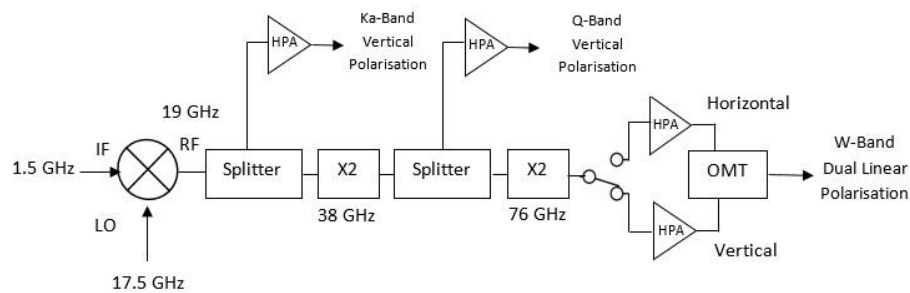


Figure 2-23: Time switched dual polarisation design outline using two HPAs

### 2.3.10.2 Dual Frequency Dual Polarisation (DFDP)

The DFDP scheme utilises dual up-conversion chains and requires a mixing stage at each chain. The difference between the previous architectures is the use of an OMT instead of a polariser and the use of both up-converters to transmit the dual linear polarisation. The two input ports of the OMT will be each connected to one of the up-converted chains, producing a simultaneous dual linear polarisation at the W-band. This will require one oscillator to be tuned at 17.5 GHz while the other oscillators are to be tuned at 1.5 GHz and 1.499,999 GHz respectively (1 MHz apart). The outline architecture of a DFDP is shown in Figure 2-24.

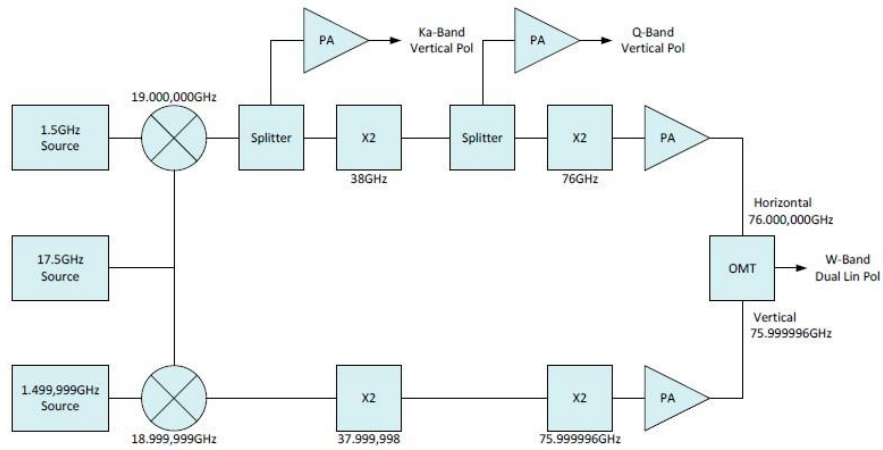


Figure 2-24: Dual Frequency Dual Polarisation design outline

The advantages of this polarisation scheme are that it will not require any synchronisation at the ground station and the switching limitations discussed previously will not be an issue as no switching takes place. All these come at the cost of DC power budget since both up-conversion chains need to be active to produce the dual linear polarisation at W-Band. In order to save on additional hardware, this design can accommodate the main HPA on one polarisation and the redundant HPA on the other polarisation. In this case there will be no switch for the additional HPA, as the two will be combined at the OMT and can operate independently. This would then eliminate the requirement for a high power, low loss switch at W-band for HPA redundancy.

### 2.3.11 Phase Noise

An oscillator is a crucial component in terms of the phase noise of the system. There are different oscillators on the market and some of them have internal references while others have external references. A good frequency reference should provide low phase noise as well as low frequency drift. Furthermore, the reference oscillator frequency will also determine the tuning ability.

The main contributor to phase noise in a system comes from the oscillators. There are other components that can also contribute to system phase noise, such as amplifiers and frequency multipliers. Amplifiers tend to have low phase noise, therefore their impact on the system is negligible. On the other hand, frequency multipliers always degrade phase

noise by a theoretical  $20 \log(N)$ , where  $N$  is the multiplication factor. During the calculations, the phase noise degradation from a frequency doubler has been modelled at a total of 8 dB; consisting of the sum of 6 dB and 2 dB being the theoretical ( $20 \log(2)$ ) and added margin.

Microwave Dynamics (MD) produces very competitive space qualified oscillators, offering a wide range of space qualified products. The two main oscillators proposed here are the PLO-4000 and PLO-5200. Both produce signals up to 40 GHz (50 GHz for the PLO-4000) and have an external reference. The PLO-4000 can accept a reference input frequency of 5 MHz or 10 MHz while the PLO-5200 can accept a reference signal of any frequency up to 250 MHz.

The PLO-4000 phase noise envelope from the datasheet is shown in Figure 2-25. As can be seen, when generating a signal at 22 GHz the phase noise is about -73 dBc/Hz and -83 dBc/Hz for the 1 kHz and 10 kHz offsets [9].

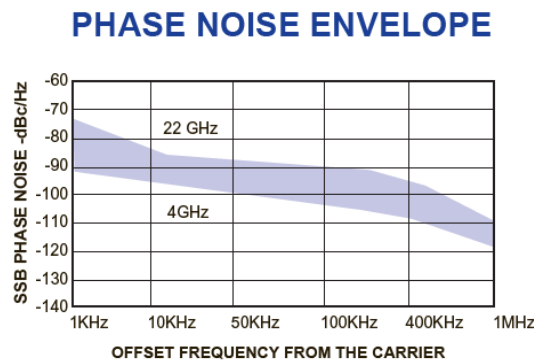


Figure 2-25: PLO-4000 Phase noise envelope copied from [9]

The PLO-5200 datasheet does not provide a graph with the phase noise envelope, just the phase noise -85 dBc/Hz at the 10 kHz offset. Table 2-14 reports the phase noise of the PLO-5200 and PLO-4000 at 4 GHz and at 22 GHz [10].

The highlighted fields in Table 2-14 are extrapolations since this information is not explicitly provided in the datasheets. The phase noise quoted in Table 2-14 for the PLO-5200 is assumed to follow the same trend as that of the PLO-4000. The extrapolation is based on an assumption that phase noise degrades by 10 dB from the 100 Hz up to the 100 kHz offset while, 20 dB of degradation is noticed from 100 Hz to 10 Hz, 100 kHz and 1 MHz – following the pattern of PLO-4000.

Table 2-14: PLO-4000 and PLO-5200 phase noise [9], [10]. Highlighted fields are extrapolations from the datasheet.

	PLO-4000		PLO-5200
Freq. Offset (Hz)	Phase Noise @4GHz	Phase Noise @22GHz	Phase Noise
10	-60	-40	-40
100	-80	-60	-60
1 k	-91	-73	-73
10 k	-95	-83	-85
100 k	-103	-90	-90
>100 k	-118	-109	-109

It should be noted that for generating a frequency of 19 GHz, the phase noise will be improved when compared to the value at 22 GHz provided in the datasheet. This can be seen from Figure 2-25 where the plotted phase noise envelope is reproduced from the datasheet. The 22 GHz and 4 GHz phase noise is noted as the worst case scenario since a 1.5 GHz and a 17.5 GHz signal are needed to generate the 19 GHz RF signal.

Table 2-15: Expected phase noise for the chains. Highlighted fields are extrapolations from the datasheet.

Freq. Offset (Hz)	Ka-Band Expected Phase Noise	Q-Band Expected Phase Noise	W-Band Expected Phase Noise
10	-40	-32	-24
100	-60	-52	-44
1 k	-73	-65	-57
10 k	-83	-75	-67
100 k	-90	-82	-74
>100 k	-109	-101	-93

The expected phase noise of the chains is reported in Table 2-15. The phase noise at the different offsets has a comfortable margin except the 100 kHz and 1 MHz offsets. As mentioned above, these are the worst-case scenarios using the quoted phase noise for 22 GHz and 4 GHz with a degradation of 8 dB per chain.

Another consideration for oscillators would be the space qualified synthesizer LMX2615-SP by Texas Instruments, released in June 2018. It can provide 40 MHz to 15 GHz output frequency and could be used as the L-band oscillator at 1.5 GHz. Figure 2-26 provides the phase noise for an 8.1 GHz sine wave with a power output of 4.9 dBm [11]. It provides better phase noise than the MD PLO series oscillators. Furthermore, the synthesizer can be programmed to provide fine frequency steps of 1 Hz [11]. This would be beneficial in the case of the dual frequency dual polarisation scheme.

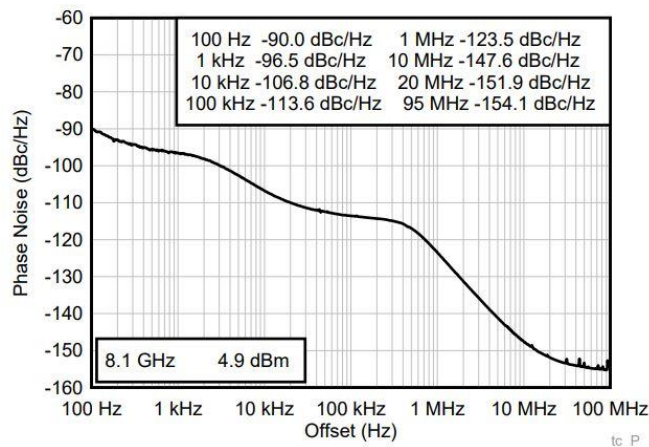


Figure 2-26: LMX2615-SP phase noise at 8.1GHz, copied from [11]

For the reference oscillator, MD offers the OCXO-200. It can provide a frequency of 100 MHz with a stability of  $\pm 5$  ppm [12]. Spectratime also provides a space qualified OCXO master oscillator that can provide a 10MHz signal with a 0.1 ppm stability per day [13]. Table 2-16 provides some of the specifications of the Spectratime master oscillator and [13] the typical phase noise. Based on the improved stability, the proposition is to use the Spectratime reference oscillator.



Table 2-16: Spectratime specifications copied from [13]

Type		MO4D-SC	
Parameter	Value		
Dimensions	44 x 54 x 57 (44) mm		
Output signal frequency	10 MHz*		
Frequency long term stability, 1st year	$< \pm 3 \times 10^{-8}$ / year		
Average ageing per day after 1 month	$< \pm 1 \times 10^{-10}$ / day		
Frequency long term stability, years after	$< \pm 1 \times 10^{-8}$ / year		
Frequency short term stability(0.1-10 s)	LN $< 5 \times 10^{-13}$	Std $< 3 \times 10^{-12}$	
Frequency stability over full temp. range	$< \pm 1 \times 10^{-9}$		
Frequency adjustment	$> \pm 1.5$ Hz		
SSB phase noise assuming 10MHz carrier in dBc/Hz	LN	Std	
	1 Hz	$< -105$	$< -100$
	10 Hz	$< -135^*$	$< -130^*$
	100 Hz	$< -145$	$< -140$
	1000 Hz	$< -155$	$< -150$
	10000 Hz	$< -160$	$< -155$
* Subject to export control (end user statement required)			
Output signal level	4,5 dBm $\pm$ 1dBm		
Output impedance	50 $\Omega$ $\pm$ 20%		
Harmonics	-30 dBc		
Spurious signals	-120 dBc		
Power consumption during warm-up	8 W		
Nominal power consumption	3.5 W		
Maximum power consumption in operation	5.5 W		
Volume	$< 0.15$ dm <sup>3</sup>		
Power supply	12 - 18 V		
Warm-up time (accuracy $< \pm 2 \times 10^{-8}$ at 25°C)	20 minutes		
Mass (stainless steel cover)	220 gr		

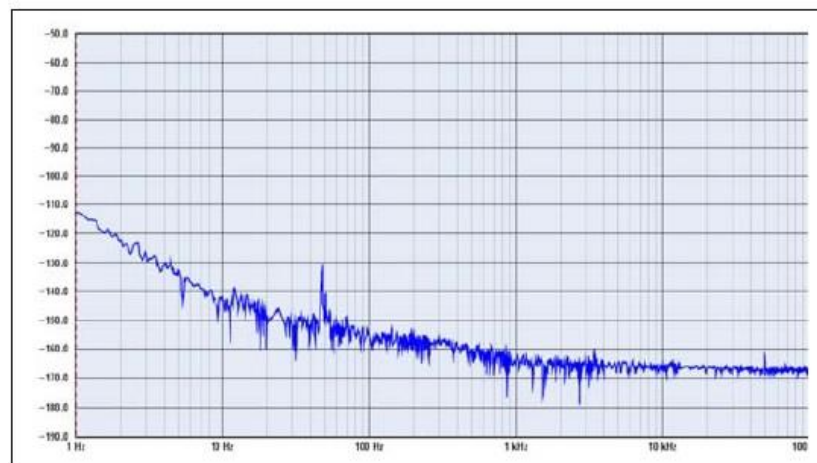


Figure 2-27: Spectratime typical phase noise copied from [13]

### 2.3.12 Mass and DC Power Consumption

The beacon has a total of 64 configurations and the worst-case scenario in terms of total DC power consumption is ~ 100W (~80W best case), assuming a DC-DC converter efficiency of 75%. During this configuration, both up-converter chains are active with one providing the Ka-band signal and the other the higher Q- and W-band signal. In Table 2-17 the breakdown of the DC power consumption per band is provided which takes into account the frequency generation as well. A breakdown of the total mass, including both up-converters and antennas, is shown in Table 2-17.

*Table 2-17: Beacon Mass and DC Power Consumption with a DC-DC converter efficiency of 75%*

	<b>Mass (Kg)</b>	<b>DC Power Consumption (W)</b>
<b>Ka-Band</b>	3.4	41.5
<b>Q-Band</b>	2.8	30.1
<b>W-Band</b>	1.4	27.8
<b>Miscellaneous</b>	4	-
<b>Two Up-converter Redundancy</b>	<b>21.7</b>	<b>99.4</b>

### 2.3.13 TT&C Operations

The TT&C function for the payload is likely to be serviced by the TT&C of the spacecraft. There are off the shelf options for this. Thales Alenia Space (TAS) TT&C was used for the Alphasat campaign and still offers a TT&C at X-band which is also compatible with ESA TTC standards for scientific missions (ECSS-E-50-05A). Other companies that provide TT&C are ViaSat at S-Band and MDA.

The TAS TT&C transponder has two independent modules assembled as a single equipment (Receiver and Transmitter) and a lead time of 12 months. The mass of the transponder is 3.6 kg and it has a power consumption of 25 W (RX: < 10 W, TX: < 15 W). It presents a favourable solution for the payload.

## 2.4 Compliance Matrix

The beacon payload compliance matrix is shown in Table 2-18.

Table 2-18: Beacon Compliance Matrix

		Requirements	Proposed Payload
<b>Operational Frequencies</b>	Ka-Band	19 GHz	19 GHz
	Q-Band	38 GHz	38 GHz
	W-Band	76 GHz	76 GHz
<b>Coverage</b>	Ka-Band	EU	EU
	Q-Band	EU	EU
	W-Band	EU	EU
<b>EIRP on Boresight</b>	Ka-Band	59.4 dBm	60.65 dBm
	Q-Band	58.9 dBm	60.50 dBm
	W-Band	52.3 dBm	53.40 dBm
<b>Polarisation</b>	Ka-Band	Linear	Linear
	Q-Band	Linear	Linear
	W-Band	Circular	Circular
<b>Phase Noise @10Hz Offset</b>	Ka-Band	-30 dBc	-40 dBc
	Q-Band	-22 dBc	-32 dBc
	W-Band	-14 dBc	-24 dBc
<b>Beacon Lifetime</b>	Overall	5 years – 95% reliability	× 2 redundancy
<b>DC Power Consumption (worst case)</b>	Overall	150 W	100 W
<b>Mass</b>	Overall	50 kg	22 kg

## 2.5 Future Work

Within this section, the beacon coverage and trade-offs are discussed as the considerations that need to be taken in account before moving forward to a finalised beacon design. Furthermore, considerations on the availability and development of certain proposed components for the beacon are discussed.

### 2.5.1 Beacon Coverage and Trade-offs

During the design process of the three-frequency beacon payload two coverages were taken into account: European and Tropical, and European-only coverage. The payload design that includes the Tropics is not compliant in terms of the overall DC power consumption that comes at 157 W as opposed to the 100 W of the European-only coverage (noting that the requirement was set at 150 W).

Furthermore, the two coverages offer different mass and cost estimates (in terms of RF component hardware). The proposed coverage that includes the Tropics has an estimated mass and cost of 25.5 kg and €2.2M respectively. On the other hand, the European-only coverage has an estimated mass and cost of 21.7 kg and €2M respectively. The increase in cost and mass in the Tropics coverage is attributed to the fact that the antenna's half power beam width is larger and therefore has a lower gain. In order to achieve the specified boresight EIRP and make up on the lower gain as opposed to the European-only coverage, a power combiner of two HPAs is used to achieve a higher power output. The difference of 1.9 dB in the antenna gain of the European-only coverage relaxes the output power required to achieve the specified EIRP. A summary of the two antenna parameters for the two coverages is shown in Table 2-19.

As indicated in the propagation experiment section, a dynamic range of  $> 30$  dB in the ground receivers is not of high importance, especially to telecommunication companies. A more relaxed dynamic range can be translated to a lower EIRP specification. The achievable EIRP that was specified based on a link budget with  $> 30$  dB of dynamic range can be achieved with a lower cost, mass, DC power consumption for the European coverage only. For a European & Tropics coverage the antenna gain is lower (by 1.9 dB compared to EU only antennas) and the power consumption of the payload is not

compliant due to the use of power combiners to achieve the required output power and therefore EIRP. With a more relaxed EIRP, the lower gain antennas with higher beam width and Tropic coverage could be used with the existing European only payload. The penalties in EIRP would be 0.85 dB, 0.5 dB and 0.8 dB for the Ka, Q and W-band respectively as shown in Table 2-20.

*Table 2-19: Antenna parameters for European & Tropic and European-only coverage*

	<b>Band</b>	<b>Antenna Diameter (cm)</b>	<b>HPBW</b>	<b>Boresight Gain (dBi)</b>
<b>EU &amp; TC Coverage</b>	Ka-Band	14	7.89°	27.4
	Q-Band	7	7.89°	27.4
	W-Band	4	7.67°	27.6
<b>EU Only Coverage</b>	Ka-Band	18	6.14°	29.5
	Q-Band	9	6.14°	29.5
	W-Band	4.5	6.14°	29.5

*Table 2-20: EIRP margin with EU payload design and EU & TC coverage antennas*

		<b>Power at Antenna (dBm)</b>	<b>Achieved EIRP on boresight (dBm)</b>	<b>Margin (dB)</b>
EU payload design with EU & TC Coverage	Ka-Band	31.15	58.55	<b>-0.85</b>
	Q-Band	31.0	58.4	<b>-0.5</b>
	W-Band	23.9	51.5	<b>-0.8</b>

## 2.5.2 Availability and Performance of Selected Components

Through the development of the GEO payload beacon several considerations were made when selecting components. One of the considerations was to be space qualified but this has not always been possible. The non-space qualified components, which include variable gain amplifiers, attenuators and detectors are all GaAs devices. GaAs based technology is space qualifiable and therefore, these devices would need to be qualified ahead of the mission.

Furthermore, some components (amplifiers, frequency multipliers, detectors and variable attenuators) chosen during the design of the payload need to be packaged as they are just the bare die (losses during the design have been taken into account for such components).

According to the statement of work, dependencies on non-ESA member states for components should be identified. A priority to ESA member state suppliers was given throughout the development but this was not always possible. Several active (e.g. oscillators, amplifiers, frequency multipliers) and passive (e.g. filters, splitters, couplers, polariser, antennas) components were selected from the USA companies (Microwave Dynamics, Pasternack, Millitech, Qorvo). Furthermore, some components, including filters, antennas and redundancy switches have to be custom made. There are available quotes from Millitech for the filters and antennas but development, manufacturing, testing and qualification could be done from RAL Space (UK) and/or Thomas Keating Ltd (UK) for the antennas.

Potential contributions from the parallel development in the ARTES 5.1 activity on the LEO W-band beacon campaign could be made. According to [14], the payload consists of a Q- and W-band at 37.5 GHz and 75 GHz. Components that could benefit the GEO W-band beacon development are the local oscillator, band pass filters, frequency multipliers, couplers and switches. Furthermore, the design of the payload relies mainly on components designed from Fraunhofer IAF. Such developments will improve European know-how and competitiveness.

## **2.6 Conclusion**

A three-frequency satellite payload design at Ka-, Q- and W-band for propagation measurements has been shown. The antenna specifications currently cover only Europe but with a trade-off in EIRP the Tropics can also be included. The simulated EIRP on

boresight is reported at 60.65 dBm, 60.50 dBm and 53.40 dBm for the Ka-, Q- and W-band equivalently. The lower bands will operate with a linear polarisation and W-band with a circular polarisation. The payload offers 64 configuration paths with the DC power consumption at 100 W in the worst-case routing scenario. Furthermore, the expected weight of the payload along with all the redundancies is expected around 22 kg.

It is noted from the Section 3.5 that there is future work to be done for such a payload to be realised, especially with the use of European-only suppliers. Ahead of the campaign, several components would require packaging while others are not yet available in the European market and would require development.

As discussed in Chapter 2, the current ITU-R models on the atmospheric impairments are not yet validated at W-band. A future GEO campaign at W-band would greatly benefit the ITU-R propagation models and would strengthen our understanding of the satellite link at this frequency band.

## References

- [1] B. R. Arbesser-rastburg, S. Member, and A. Paraboni, "European Research on Ka-Band Slant Path Propagation," in *Proceedings of the IEEE*, 1997, vol. 85, no. 6, pp. 843–852.
- [2] D. Cox and H. Arnold, "Results from the 19- and 28-GHz COMSTAR satellite propagation experiments at Crawford Hill," *Proc. IEEE*, vol. 70, no. 5, pp. 458–488, 1982.
- [3] F. Davarian, "Ka-band Propagation Research Using ACTS," *Int. J. Satell. Commun.*, vol. 14, pp. 267–282, 1996.
- [4] H. Fukuchi, T. Kozu, N. Kenji, J. Awaka, H. Inomata, and Y. Otsu, "Centimeter Wave Propagation Experiments Using the Beacon Signals of CS and BSE Satellites," *IEEE Trans. Antennas Propag.*, vol. AP-31, no. 4, pp. 603–613, 1983.
- [5] H. Fenech, A. Tomatis, S. Amos, J. S. Merino, and V. Soumpholphakdy, "An Operator's Perspective on Propagation," in *8th European Conference on Antennas and Propagation (EuCAP 2014)*, 2014, pp. 3349–3352.
- [6] S. Ventouras, S. A. Callaghan, and C. L. Wrench, "Long-term statistics of tropospheric attenuation from the Ka / U band ITALSAT satellite experiment in the United Kingdom," *Radio Sci.*, vol. 41, pp. 1–19, 2006.
- [7] S. Ventouras, C. L. Wrench, and D. H. Long, "Investigation of the effects of rain and cloud on ehf satcom links," in *8th URSI Commission F Triennial Open Symp., Portugal*, 1998, pp. 284–287.
- [8] ESA, "Losses according to Q-Band SSPA – Predevelopment Design Report," 2007.
- [9] Microwave Dynamics, "External Ref 10 MHz PLDRO (PLO-4000)," 2006. <http://microwave-dynamics.com/wp-content/uploads/2016/05/PLO-4000-1.pdf>.
- [10] Microwave Dynamics, "PLO-5000 / 5200 Series," 2015. <http://microwave-dynamics.com/wp-content/uploads/2016/05/PLO-5000.pdf>.



- [11] Texas Instruments, “LMX2615-SP Space Grade 40-MHz to 15-GHz Wideband Synthesizer With Phase Synchronization and JESD204B Support,” 2020. <https://www.ti.com/lit/ds/symlink/lmx2615-sp.pdf?ts=1590918974592>.
- [12] Microwave Dynamics, “Oven Crystal Oscillator (OCXO-200),” 2016. <http://microwavedynamics.com/wp-content/uploads/2016/05/OXCO-200-1.pdf>.
- [13] Spectratime, “Crystal-Based Master Oscillator - MO4D-SC,” 2017. [https://www.orolia.com/sites/default/files/document-files/iSpace\\_CMO\\_short\\_Spec.pdf](https://www.orolia.com/sites/default/files/document-files/iSpace_CMO_short_Spec.pdf).
- [14] J. Flavio *et al.*, “A New Earth-LEO Propagation Campaign at Q and W-band,” *9th Adv. Satell. Multimed. Syst. Conf. 15th Signal Process. Sp. Commun. Work.*, pp. 1–6, 2018, doi: 10.1109/ASMS-SPSC.2018.8510750.

## Chapter 3

# 3 Ground Station for Propagation Measurements at Ka-Band

### 3.1 Introduction

The increasing demand for higher bandwidth satellite communication applications has led to a growing interest in the millimetre-wave bands. Furthermore, the increasing services using satellite links and the congestion of lower frequency bands such as the Ku-band, has led to the use of higher frequency bands [1]. In particular, there is a notion towards the move of gateway feeder links at frequencies bands such as Q/V and beyond and the release of Ka-band for user links [2]. However, with higher frequencies there are higher propagation impairments.

Ka-band offers a good compromise in terms of available bandwidth and channel performance at a reasonable cost. An example of a high-throughput satellite (HTS) systems that take advantage of this compromise includes the ViaSat-2 [3] which operate at Ka-band. Previous ITU-R propagation models have benefitted from the ongoing Alphasat signals for scientific experiments. ESA initiated in 2015 a dedicated project for large-scale measurement campaigns using the Alphasat Aldo Paraboni payload at Ka/Q-band (ASALASCA). The main objective of the ASALASCA experiment is to collect Ka/Q-band experimental data to support the development of new or improved models for the spatial and temporal correlation of the radio channel. The output statistics of the experiment will be submitted to the ITU-R Study Group 3 “Radiowave Propagation” for radio regulatory activities.

Due to technological advances, classic radio receivers that relied mostly on RF hardware are now accomplished through software (e.g. filters). Therefore, there is a trend towards propagation terminals in which software defined radio (SDR) is used. This reduces the RF hardware complexity and in turn the cost. This shift towards SDR has led to the drastic increase of propagation terminals able to provide experimental datasets for the site [1].

In the summer of 2016, Heriot-Watt University in collaboration with NASA Glenn Research Centre installed an operational SDR propagation terminal at Q-band tracking Alphasat. This is the lowest elevation angle propagation terminal in the ASALASCA experiment, and the addition of a Ka-band terminal followed in the summer of 2018.

In this chapter, the design and implementation of an SDR Ka-band terminal along with the recorded data and processing is shown. The remainder of the chapter is organised as follows. Section 3.2 presents the beacon receiver design. Section 3.3 presents the receiver digital signal processing. Section 3.4 shows the recorded beacon signal. Section 3.5 presents the process of obtaining the excess atmospheric attenuation from the recorded data. Finally, conclusions are presented in Section 3.6.

## 3.2 Beacon Receiver Design

The Aldo Paraboni propagation experiment payload is currently in service with two coherent beacons at Ka-band (19.701 GHz) and at Q-band (39.402 GHz). The main characteristics of the Ka-band continuous wave signal are shown in Table 3-1.

*Table 3-1: Ka-band Aldo Paraboni experimental propagation payload main characteristics*

<b>Frequency</b>	19.701 GHz
<b>Polarisation</b>	Linear Vertical
<b>Antenna Boresight</b>	32.5°N, 20°E
<b>EIRP</b>	49.5 dBm

Through a collaboration with Skyware Technologies, a leader in advanced satellite RF electronics, we were given a Low Noise Block (LNB) and an offset reflector antenna. An LNB refers to an RF receiver which down-converts the received signal. An example of components found in an LNB includes a low noise amplifier, filters, mixer and oscillator. The key characteristics of the reflector antenna and LNB are shown in Table 3-2

Table 3-2: Skyware Technologies reflector antenna characteristics and XRF3100 LNB main characteristics

<b>Antenna Diameter</b>	74cm	
<b>Antenna Efficiency</b>	~ 60%	
<b>Antenna Gain</b>	41.6 dBi (measured)	
	<b>Min.</b>	<b>Max.</b>
<b>RF Input Freq.</b>	17.8 GHz	20.2 GHz
<b>IF Output Freq.</b>	0.95 GHz	2.15 GHz
<b>Local Oscillator Freq.</b>	18.25 GHz	
<b>Total Noise Figure</b>	1.3 dB (typical)	
<b>Conversion Gain</b>	56 dB (typical)	
<b>IF Output Impedance</b>	75 Ohms	
<b>Output Connector</b>	F-Type (Male)	
<b>Supply Voltage</b>	24V DC via IF output port	
<b>Power Consumption</b>	5.4 W	

From the specifications in Table 3-2 it can be seen that more component would need to be included in order to have an operating ground terminal able to capture the receiving signal. For instance, the LNB has an output characteristic impedance of 75 Ohms. The particular LNB is usually used for satellite television, which works with a characteristic impedance of 75 Ohms. Furthermore, all equipment and components in the laboratory operate with a characteristic impedance of 50 Ohms. Therefore, a matching pad is needed to transform the impedance from 75 to 50 Ohms. Also, the LNB is powered through the intermediate frequency (IF) output port which means that the DC voltage and IF signal need to be separated. This can be achieved with a bias tee which uses an inductor attached to the DC port and a capacitor on the Radio Frequency (RF) signal port. An RF amplifier to boost the IF signal was also taken in account. Finally, an RF splitter is considered. One of the ports would be connected directly to the SDR hardware while the other to NASA's hardware.

It should be noted that the down-converted IF signal,  $f_{IF}$ , is at 1.451 GHz and was calculated from equation (3.1):

$$f_{IF} = f_{RF} - f_{LO} \quad (3.1)$$

where  $f_{RF}$  is the Aldo Paraboni signal frequency at 19.701 GHz and  $f_{LO}$  is the LNB's local oscillator frequency, which is specified at 18.25 GHz.

Suitable RF components at the IF frequency were selected and the entire Ka-band front end components are listed in Table 3-3.

*Table 3-3: Ka-band front end component list*

<b>Component</b>	<b>Manufacturer &amp; Part No.</b>	<b>Notes</b>	<b>Power Requirements</b>
<b>Reflector Antenna</b>	Skyware Technologies	Gain: 41.6 dBi @19 GHz	-
<b>LNB</b>	Skyware Technologies XRF3100	Gain: 56 dB Noise Figure: 1.3 dB	24 V @ 225 mA
<b>Cable (75Ω)</b>	IntelliConnect LMR-400-75	Insertion Losses: 5.6 dB (35 m)	-
<b>Matching Pad</b>	Mini-Circuits Z7550R-FMSF+	Insertion Losses: 5.82 dB	-
<b>Bias-Tee</b>	Mini-Circuits Z3BT-2R15G+	Insertion Losses: 1.8 dB	-
<b>IF Amp</b>	Mini-Circuits ZX60-2522MA+	Gain: 25 dB Noise Figure: 2.6 dB	5V @ 94 mA
<b>Power Splitter</b>	Mini-Circuits ZN2PD2-14W+	Insertion Losses: 3.25 dB (total) Isolation: 35 dB	-
<b>Total DC Power:</b>			<b>5.87 W</b>

The cascading noise factor,  $F_{sys}$ , can be calculated using the Friis equation as [4]:

$$F_{sys} = F_1 + \frac{F_2 - 1}{G_1} + \frac{F_3 - 1}{G_1 G_2} + \frac{F_4 - 1}{G_1 G_2 G_3} + \frac{F_5 - 1}{G_1 G_2 G_3 G_4} + \dots \quad (3.2)$$

where,  $F_1, F_2, F_3, \dots$  are the linear noise factors of the first, second, third and so forth component. Likewise,  $G_1, G_2, G_3, \dots$  are the linear gains of the associated component. In the case of insertion losses instead of gain,  $G_1, G_2, G_3, \dots$  are replaced with the linear value of the insertion losses of the component.

The final cascaded system noise figure,  $NF_{Rxsys}$ , in dB which is used in the link budget is calculated as [4]:

$$NF_{Rxsys} = 10 \log F_{sys} \text{ (dB)} \quad (3.3)$$

The component equivalent gain and noise figure (NF) are listed in Table 3-4 where the final cascaded system noise figure,  $NF_{Rxsys}$ , is calculated according to (4.2) and (4.3).  $NF_{Rxsys}$  is 1.3 dB which is the same as the LNB noise figure. This is due to the low noise and high gain of the LNB. Examining the Friis noise equation highlights the importance of the first components in a receiver chain, which is usually a low noise amplifier. Ideally, for a low system noise figure one would opt for a low noise, high gain amplifier.

*Table 3-4: Cascaded Noise Figure of the Ka-band terminal*

	<b>LNB</b>	<b>Cable</b>	<b>Matching Pad</b>	<b>Bias Tee</b>	<b>IF Amp</b>	<b>Splitter</b>
Component data (from datasheet)						
<b>Gain (dB)</b>	56	-5.6	-5.82	-1.8	25	-3.25
<b>NF (dB)</b>	1.3	5.6	5.82	1.8	2.6	3.25
Linear						
<b>Gain (linear)</b>	398107	0.275423	0.261818	0.66069	316.228	0.47315
<b>F (linear)</b>	1.34896	3.630780	3.819443	1.51356	1.81970 1	2.11348 9
Total cascaded gain (product of linear gains)						
<b>Gain (linear)</b>	398107	109647.8	28707.8	18967.0	5997911	2837919
Running total (cascaded) F (use Friis Formula)						
<b>F (linear)</b>	1.34896	1.348969	1.348995	1.34902	1.34906	1.34906
Cascaded gain and noise figure (converted to dB)						
<b><math>NF_{Rxsys}</math> (dB)</b>	1.3	1.300021	1.300104	1.30016	1.30030	1.30030
<b><math>G_{sys}</math> (dB)</b>	56	50.4	44.58	42.78	67.78	64.53

To be able to track deep atmospheric fading the receiver carrier-to-noise ratio target was set to a minimum of 30 dB. Before the purchase and implementation of the listed components, a link budget is carried out to calculate the receiver carrier-to-noise ratio.

The link budget was then drafted in order to calculate the carrier-to-noise ratio of the receiver. Within the link budget there are calculations on the ground station distance from the satellite to later calculate free space path losses (FSPL), satellite EIRP, receiver antenna gain, uplink losses and receiver noise floor calculations. The link budget for the receiving Aldo Paraboni Ka-band signal at Heriot-Watt University is shown in Table 3-7. The calculated carrier-to-noise ratio is 41.4 dB. The user inputs in Table 3-7 are highlighted in blue.

The ground station, GS, distance to the satellite is calculated from:

$$GS \text{ distance to Sat.} = \sqrt{R^2 + (R + h)^2 - 2R(R + h) \cos(g)} \quad (\text{km}) \quad (3.4)$$

where, the different parameters of (4.4) are listed in Table 3-5.

*Table 3-5: Parameters for GS distance to satellite and GS elevation and azimuth calculations*

R (Km)	Earth's Radius (6378 km)
h (km)	Satellite Altitude (35787 km)
(R + h) (km)	Satellite Radius (42165 km)
Cos(g)	= cos(q)cos(t)
q (°)	Ground station latitude
t (°)	Ground station longitude – Satellite longitude

The GS elevation angle is calculated using:

$$GS \text{ Elevation Angle} = \tan^{-1} \left( \frac{\cos(q) \cos(t) - 0.151}{\sqrt{1 - \cos^2(q) \cos^2(t)}} \right) \quad (3.5)$$

The GS azimuth angle is calculated according to the ground station location,  $q$ , and the difference between the GS and satellite longitude. This is listed in Table 3-6.

Table 3-6: GS azimuth angle according to the location of the GS in respect to the satellite

$q$ (°)	$t$ (°)	GS Azimuth Angle (°)
Negative	Negative	Az (cal)
Negative	Positive	$360^\circ - \text{Az (cal)}$
Positive	Negative	$180^\circ + \text{Az (cal)}$
Positive	Positive	$180^\circ - \text{Az (cal)}$

Where,  $Az$  (cal) is calculated as:

$$Az (cal) = \tan^{-1} \left( \frac{\tan(t)}{\sin(q)} \right) \quad (3.6)$$

The wavelength,  $\lambda$ , in meters of the incoming signal is calculated from:

$$\lambda = \frac{c}{f} \quad (\text{m}) \quad (3.7)$$

where,  $c$ , is the speed of light in vacuum ( $3 \times 10^8 \text{ ms}^{-1}$ ) and  $f$  is the frequency in Hz.

To calculate the antenna gain,  $G$ , the link budget calculator requires the input of the antenna diameter, antenna efficiency and intercepting wavelength. This is shown in (4.8) [5]:

$$G = 10 \log_{10} \left( \eta \left( \frac{\pi D}{\lambda} \right)^2 \right) \quad (\text{dBi}) \quad (3.8)$$

where  $\eta$  is the antenna efficiency,  $D$  is the antenna diameter and  $\lambda$  is the wavelength.

The FSPL is calculated as [6]:

$$FSPL = 20 \log \left( \frac{4\pi d}{\lambda} \right)^2 \quad (\text{dB}) \quad (3.9)$$

where,  $d$ , is the GS distance to satellite calculated in (3.5) and  $\lambda$  is the wavelength.

With the above information, the receiver signal strength,  $C$ , can be calculated using [6]:

$$Rx \text{ Signal Strength} = C = EIRP + G_{Rx} - FSPL - L_{fr} - L_r - A_{atm} \quad (\text{dBm}) \quad (3.10)$$



where, the *EIRP* of the Aldo Paraboni Ka-band signal is known (49.5 dBm),  $G_{Rx}$  is the antenna gain calculated with (4.8),  $L_{fr}$ ,  $L_r$  and  $A_{atm}$  are the antenna feed, antenna de-pointing and gaseous attenuation losses respectively. Essentially, (3.10) is the carrier power received in the terminal.

The noise of the receiver is then required to calculate the carrier-to-noise ratio. The theoretical thermal noise floor density,  $NF_{ther}$ , can be calculated with [4]:

$$NF_{ther} = 10 \log(kT_o B) + 30 \text{ (dBm/Hz)} \quad (3.11)$$

where,  $k$  is Boltzmann's constant at  $1.38 \times 10^{-23} \text{ JK}^{-1}$ ,  $T_o$  is the reference temperature in Kelvin at 290 K and  $B$  is the bandwidth. Therefore, the theoretical thermal noise floor density is -174 dBm/Hz as calculated below.

$$NF_{ther} = 10 \log(1.38 \times 10^{-23} \times 290 \times 1) + 30 = -174 \text{ dBm/Hz}$$

The system temperature,  $T_{sys}$ , can be calculated as:

$$T_{sys} = NT_{sky} + T_{Rxsys} \text{ (K)} \quad (3.12)$$

where,  $NT_{sky}$  is the sky noise temperature during a clear sky. For Ka-band, it is typically assumed at 70K [7].  $T_{Rxsys}$  is the cascaded system noise figure,  $NF_{Rxsys}$ , converted to a temperature in kelvin relative to room temperature, with  $T_o$ , assumed at 290K [8].

$$T_{Rxsys} = T_o \left( 10^{\frac{NF_{Rxsys}}{10}} - 1 \right) \text{ (K)} \quad (3.13)$$

Therefore, the final noise figure,  $NF_{sys}$ , in dB can be calculated as [8]:

$$NF_{sys} = 10 \log \left( \frac{T_{sys}}{T_o} + 1 \right) \text{ (dB)} \quad (3.14)$$

The receiver noise floor density,  $N_o$ , can then be calculated as:

$$Rx \text{ Noise Floor Density} = N_o = NF_{ther} + NF_{sys} + \text{ (dBm/Hz)} \quad (3.15)$$

The receiver noise floor,  $N$ , is calculated from:

$$Rx \text{ Noise Floor} = N = N_o + 10 \log(RBW) \text{ (dBm)} \quad (3.16)$$

where,  $RBW$  is the resolution bandwidth of the receiver. The resolution bandwidth refers to the samples per second that the signal is captured and integrated.

The carrier-to-noise ratio,  $CNR$ , is therefore calculated using:

$$CNR = C - N \text{ (dB)} \quad (3.17)$$

Table 3-7: Link budget

<b>Downlink</b>		
<b>Satellite</b>		
Satellite Position (°)	25.00	
<b>Ground Station</b>		
Latitude (°)	55.91	
Longitude (°)	-3.32	
L (LongES-LongSat)	-28.32	
Dis. GS to Satellite (Km)	39410.43	
GS Azimuth angle (°)	146.95	
GS Elevation angle (°)	21.49	
<b>Downlink Frequency</b>		
Frequency (GHz)	19.70	
$\lambda$ (m)	0.02	<b>Wavelength</b>
<b>Rx Antenna par.</b>		
D (m)	0.74	<b>Rx Antenna Diameter</b>
$\eta$ (%)	60.00	<b>Rx Antenna Efficiency</b>
G (dBi)	41.46	<b>RX Antenna Gain</b>
<b>Losses</b>		
Lfr (dB)	0.20	<b>RX Antenna Feed Losses</b>
Lr(dB)	0.10	<b>RX Antenna De-pointing Losses</b>
Aatm(dB)	1.00	<b>Gaseous Attenuation at Ka-band</b>
FSPL(dB)	210.24	<b>Downlink Free Space Path Loss</b>
<b>Downlink parameters</b>		
EIRP(dBm)	49.50	<b>Ptx+Gtx-Losses</b>
Rx Signal Strength (dBm)	-120.59	<b>Power Received at satellite</b>
Sky Noise Temperature (K)	70.00	<b>Sky Noise Temp. during clear sky <math>NT_{sky}</math></b>
Rx System NF (dB)	1.30	<b>Receiver System Noise Figure (Friis) <math>NF_{Rxsys}</math></b>
System NF (dB)	2.01	<b>Final System Noise Figure of receiver <math>NF_{sys}</math></b>
Rx Noise Density (dBm/Hz)	-171.99	<b>No</b>
Resolution BW (Hz)	10.00	<b>10 samples per second</b>
Rx Noise Floor (dBm)	-161.99	<b>Noise floor of receiver</b>
Rx CNR (dB)	41.40	<b>Carrier-to-Noise Ratio</b>

Figure 3-1 shows the Ka-band front-end block diagram. The input power at the LNB is at -120.6 dBm. The expected power of the Ka-band continuous wave signal to be received is at -56 dBm, with the noise floor at -81 dBm.

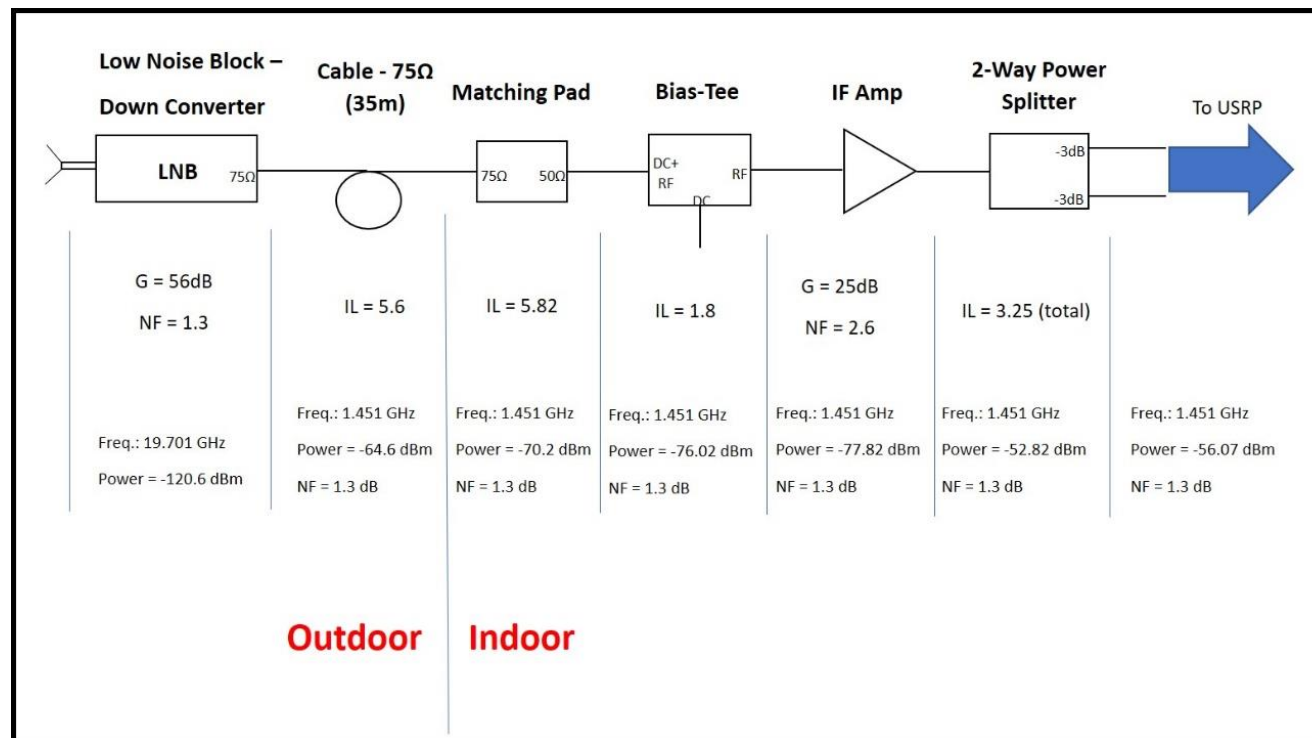


Figure 3-1: Ka-band front-end block diagram

Through the link budget calculation, the designed front end would be able to receive the Aldo Paraboni Ka-band signal with a CNR of > 30 dB at 10 samples per second. The Alphasat satellite is in geosynchronous orbit, however, its observed position from the GS is expected to vary slightly over time as a result of the satellite's inherent inability to maintain stable orbital inclination angles. These variations are predicted deterministically and are available in the form of Orbit Ephemeris Messages (OEM) files. The current deployed Q-band front-end is equipped with an open-loop tracking system (QPT 200 positioner with stepper motors) and uses OEM tracking files provided by POLIMI to track these orbital changes. Figure 3-2 shows the elevation variation of the Alphasat satellite as viewed from Heriot-Watt University. The variation observed is of the order of  $\pm 4.8^\circ$ . Pointing losses,  $L_r$ , can be calculated from:

$$L_r = 12 \left( \frac{a_\tau}{HPBW} \right)^2 \text{ (dB)} \quad (3.18)$$

where  $a_\tau$  is the offset angle and  $HPBW$  is the 3 dB (half power) beamwidth which can be calculated with respect to the antenna diameter,  $D$  and wavelength,  $\lambda$  as [5]:

$$HPBW = \frac{70\lambda}{D} \text{ (degrees)} \quad (3.19)$$

Table 3-8 shows the pointing losses for the Ka-band and Q-band antennas in the case of pointing errors of  $0.5^\circ$  to  $3.5^\circ$ . In the extreme case of a pointing error of  $3.0^\circ$  the Ka-band pointing losses would be 52 dB resulting in the loss of the signal since the CNR is quoted at 41 dB. In any case, additional losses due to antenna pointing errors would result in inaccurate data which would require post processing to correct.

*Table 3-8: Antenna pointing loss*

Band	Antenna Diameter (m)	Wave-length (mm)	HPBW	$a_\tau = 0.5^\circ$	$a_\tau = 1.0^\circ$	$a_\tau = 2.0^\circ$	$a_\tau = 3.0^\circ$	$a_\tau = 3.5^\circ$
				Pointing loss (dB)	Pointing loss (dB)	Pointing loss (dB)	Pointing loss (dB)	Pointing loss (dB)
Q-Band	0.6	7.61	0.89	3.80	15.21	60.83	136.88	186.30
Ka-Band	0.74	15.23	1.44	1.45	5.78	23.13	52.05	70.85

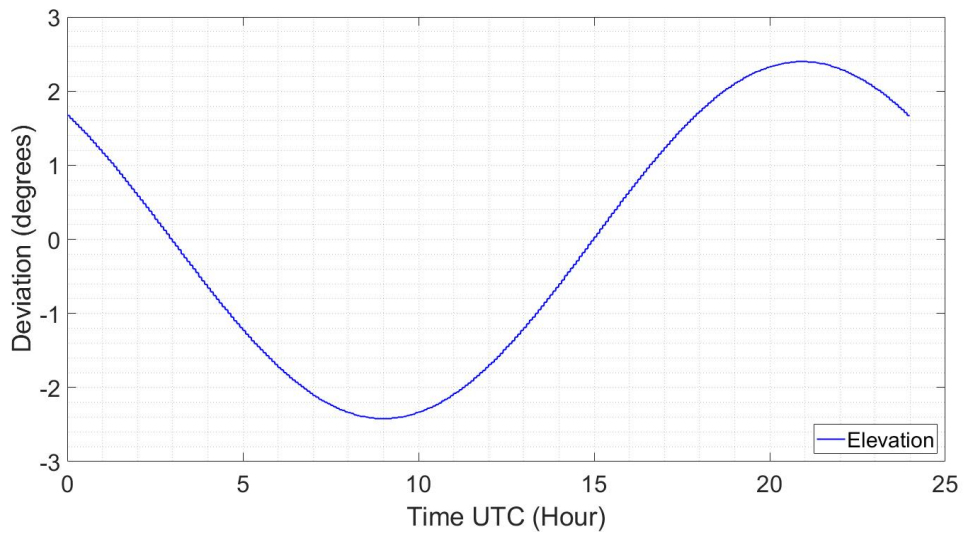


Figure 3-2: Alphasat movement as observed from the Chilbolton Observatory

Due to the high pointing losses, the Ka-band antenna should be mounted on a positioner. A cost-effective solution would be for the Ka- and Q-band antennas to share the current positioner. In order to do this, a new aluminium plate was designed using AutoCad software and manufactured in the university mechanical workshop. Figure 3-3, shows the designed base plate and the allocation of the Ka- and Q-band antennas.

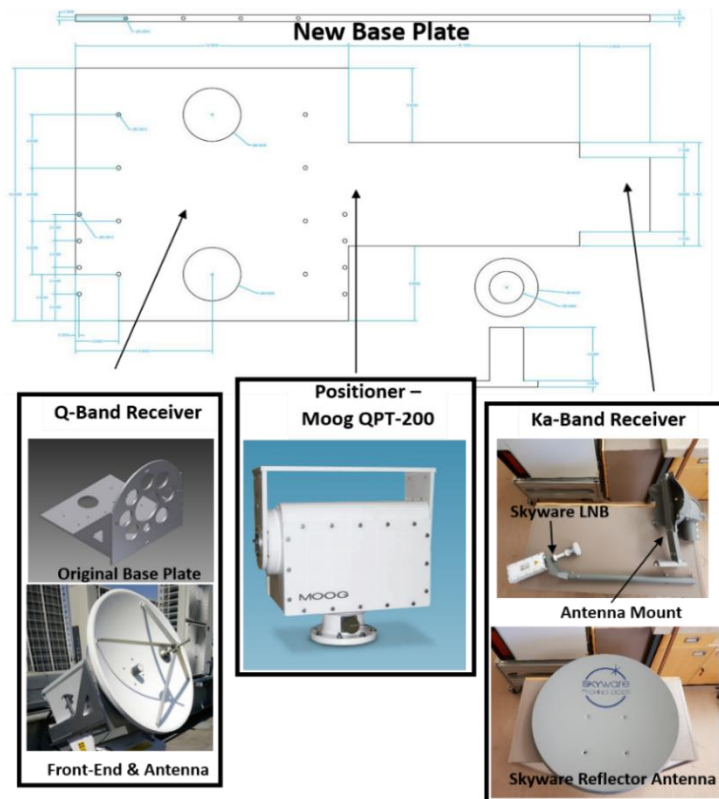
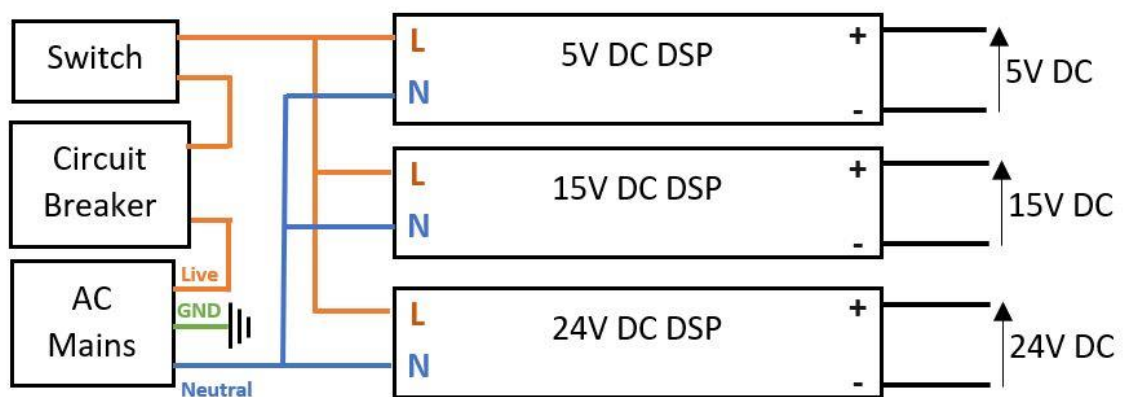


Figure 3-3: Antenna aluminium base plate

After the mechanical accommodation, the design and implementation of the Ka-band front-end electrical accommodation was considered next. As per Table 3-3, the LNB and IF amplifier require voltages of 20V and 5V respectively. As mentioned earlier, the Ka-band signal will be split between the current design and a NASA terminal. The NASA terminal further down-converts the LNB 1.451 GHz signal to 5 MHz with the use of a mixer and an external oscillator which require a 5 V supply. Furthermore, an amplifier was added to the Q-band down-converted 5 MHz signal which requires a 15 V supply. A decision was made to accommodate the external oscillator and amplifier in the same electrical box. Table 3-9 lists the electrical components used to generate the 5-, 15- and 20-Volts DC. Figure 3-4 shows the electrical design diagram for the DC voltage generation.

*Table 3-9: Enclosure and electrical components for DC generation*

Component	Manufacturer	Part Number	Comments
Enclosure	Fiboz	TA342912T	344x289x117.4mm
DSP DIN Power Supply	TDK-Lambda	DSP-10-5	5V,1.5A
DSP DIN Power Supply	TDK-Lambda	DSP-10-15	15V,0.67A
DSP DIN Power Supply	TDK-Lambda	DSP-10-24	24V,0.24A
Circuit Breaker	TE Connectivity	W58-XB1A4A-3	250VAC,3A
IEC Connector	Qualtek Electronics	858-10/015	250VAC,10A
Switch	RS PRO	419-744	250VAC
Indicator Light	Dialight	559-0202-007F	5V,10mA
Indicator Light	CAMDENBOSS	IND515205-1440	15V,40mA
Indicator Light	RS PRO	206-867	24V,20mA



*Figure 3-4: Electrical diagram*

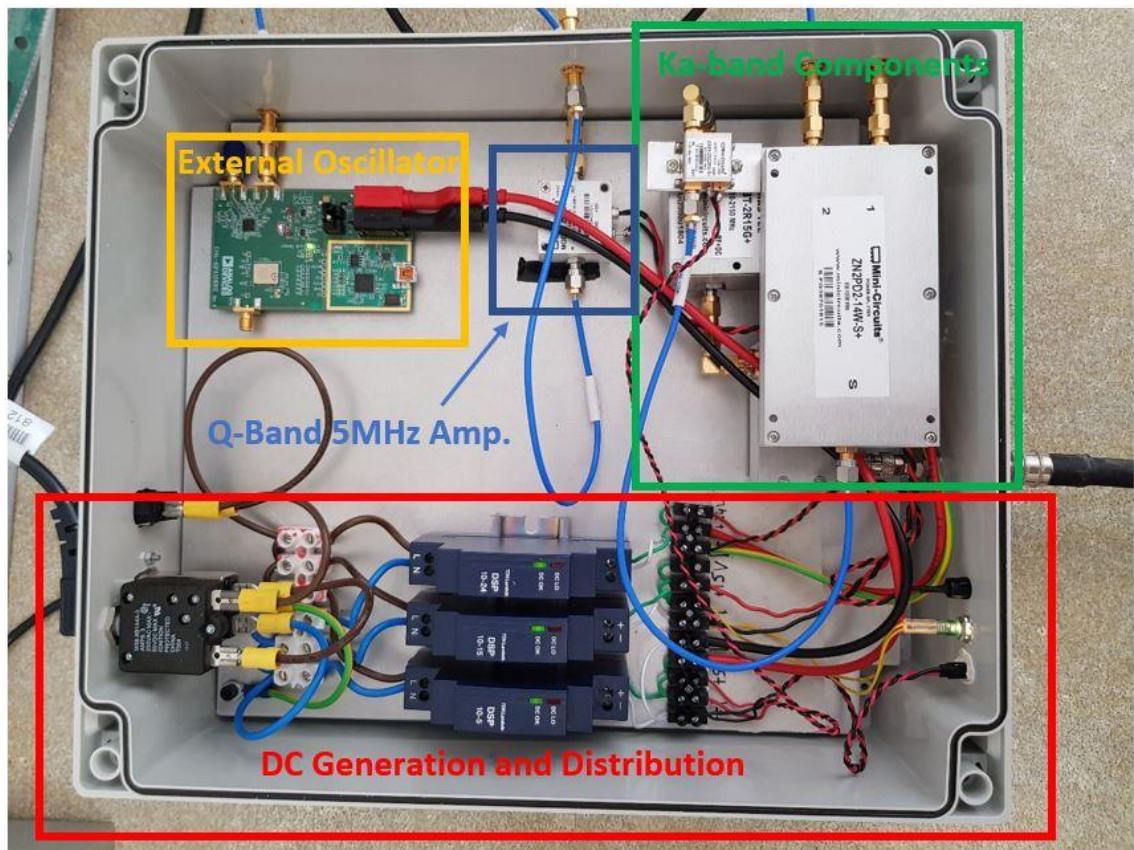


Figure 3-5: Electrical box accommodation (top view)

Figure 3-5 shows the completed electrical box. In the bottom of the enclosure there is an aluminum plate that is connected to “earth” ground and also acts as a heatsink for the placed components. On the top left of the enclosure, there is the external oscillator for the NASA terminal second down-conversion box. On the top middle of the enclosure, there is the Q-band IF amplifier. On the top right of the enclosure, there are the additional components listed in Table 3-3. On the bottom half of the enclosure, there is the DC generation and distribution with the components listed in Table 3-9.

Figure 3-6 shows the installed antennas on the roof of the Earl Mountbatten Building in Heriot-Watt University.



*Figure 3-6: Mounted antennas on the Earl Mountbatten roof*

With the implementation and operation of the Ka-band a flaw in the design was discovered. The Mini-Circuits matching pad was overheating. A temporary solution was placing a heatsink on the top and bottom of the matching pad. Overheating was occurring because the matching pad was designed with a resistive network to achieve the transition in matching. The resistors in use were surface mount and upon closer inspection of the datasheet the Mini-Circuits matching pad had a maximum DC power handling of 0.25W. This is almost 22 times lower than DC power that was feeding the LNB (at 5.4W). Therefore, an in-house matching taper (pad) was manufactured to replace the existing one.



### 3.3 Receiver Digital Signal Processing

A universal software radio peripheral (USRP) usually has an RF front end. The front end of such a receiver consists of a low noise amplifier (LNA), mixer and oscillator as shown in Fig. 2. The LNA usually has a tuneable gain, while the local oscillator provided with the USRP can be connected to a more stable master oscillator (e.g. 10 MHz master oscillator) and is also tuneable. Therefore, by selecting an appropriate frequency for the local oscillator to be tuned, one can sample the signal at baseband. The selected USRP was the the Ettus B200. This is shown in Figure 3-8 and some of its receiver specifications are listed in Table 3-10 [9].

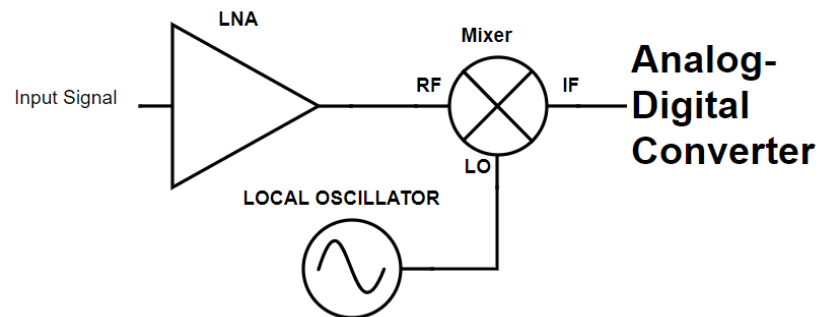


Figure 3-7: Typical USRP RF front end

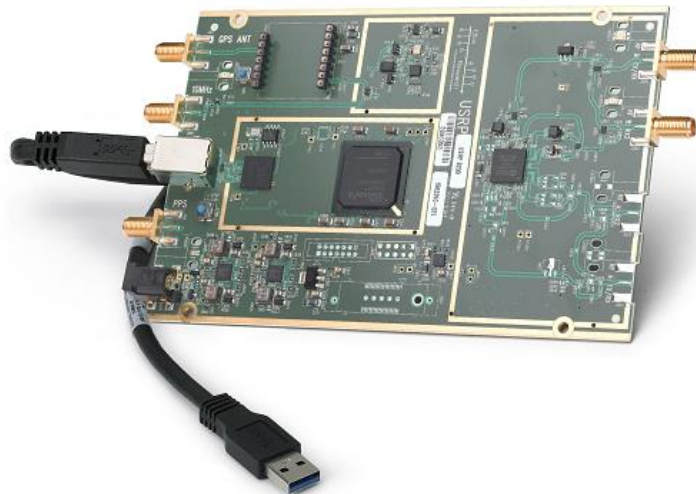


Figure 3-8: Ettus B200 SDR transceiver board copied from [9]

Table 3-10: Ettus B200 receiver general characteristics

<b>Input Freq. Range</b>	70 MHz – 6 GHz
<b>ADC Sample Rate (max)</b>	61.44 MS/s
<b>ADC Resolution</b>	12 bits
<b>Interface</b>	USB 3.0
<b>DC Input</b>	6V

The signal to be processed is a discrete time signal. A discrete Fourier transform (DFT) is employed to translate our sampled signal from the time domain to the frequency domain. The fast Fourier transform (FFT) is a common implementation of the DFT, which is computationally more efficient but, for all purposes other than numerical efficiency, the two are synonymous.

The discrete-time sequence that is sampled can be manipulated on a computer and an advantage of the DFT is that it involves a summation instead of an integral, which is easier to implement. For a given data vector  $w[k]$  of length  $N$  where  $n = 0, 1, 2, 3 \dots, N - 1$  the DFT is defined as:

$$W[n] = \sum_{k=0}^{N-1} w[k] e^{-j\left(\frac{2\pi}{N}\right)nk} \quad (3.20)$$

The inverse, IDFT is defined as

$$w[k] = \frac{1}{N} \sum_{n=0}^{N-1} W[n] e^{j\left(\frac{2\pi}{N}\right)nk} \quad (3.21)$$

The DFT is used to translate from the time domain to the frequency domain and the IDFT performs the inverse transformation (from frequency to time).

When computing the DFT of a discrete signal, a window is always applied. When not specified, a rectangular window of length  $N$  is applied on the data vector Figure 3-9 depicts this rectangular window and its Fourier Transform.

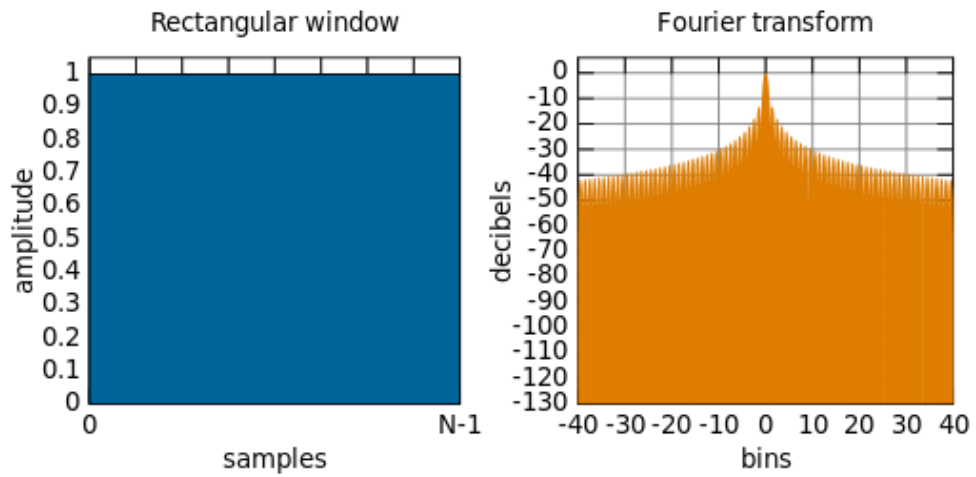


Figure 3-9: Rectangular window and its Fourier transform

When measuring the spectrum, we encounter spectral leakage. Spectral leakage is the result of an assumption in the FFT algorithm that the time record is exactly repeated throughout all time and that signals contained in a time record are thus periodic at intervals that correspond to the length of the time record. If the time record has a nonintegral number of cycles, this assumption is violated and spectral leakage occurs.

At this point, it is useful to introduce the resolution bandwidth, RBW, which refers to the size of the frequency bins. The RBW is the sampling rate  $F_s$  divided by the length  $N$  of the FFT or window function to be used (these are always the same) as shown in equation (3.22):

$$RBW = \frac{F_s}{N} \text{ (Hz)} \quad (3.22)$$

An example follows that shows spectral leakage. Spectral leakage will occur when the frequency sampled is not a multiple of the resolution bandwidth. Having a sampling rate,  $F_s = 65536 \text{ Hz}$  and an FFT length  $N = 2^{11} = 2048$  yields a RBW of 32 Hz. Sampling a signal with a frequency of  $f = 300 \text{ Hz}$  which is not an integer multiple of the RBW will have spectral leakage and the spectrum will be spread across adjacent bins as in Figure 3-10.

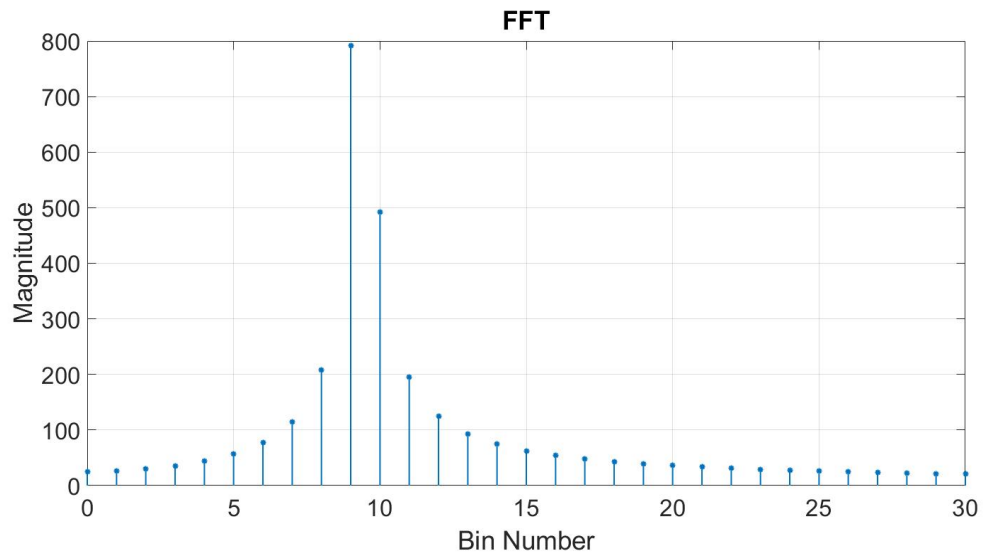


Figure 3-10: 300Hz sampled frequency with spectrum leakage

On the other hand, sampling a frequency of 294 Hz which is a multiple of the RBW will yield no spectral leakage as shown in Figure 3-11.

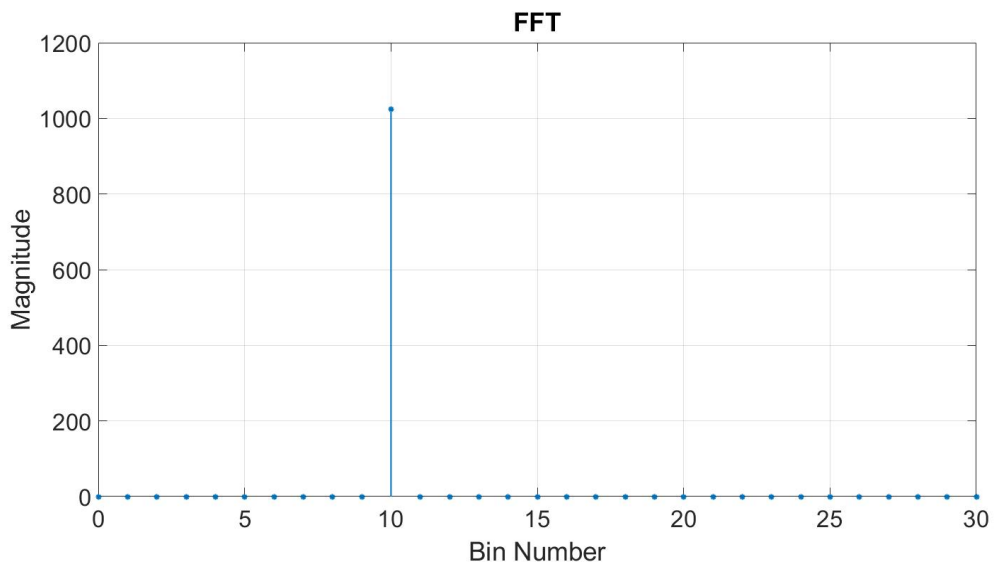


Figure 3-11: No spectrum leakage when sampling a signal at 320Hz

To minimise the effects of spectral leakage, different windows can be applied. The most common is the Hanning window for general usage and the flat-top window for accurate amplitude readings. Using the flat-top window ensures a maximum amplitude error of less than 0.01% [10]. This window broadens the resolution bandwidth (according to the window), resulting in the spreading of the signal to adjacent bins. The Hanning and flat-top windows have an increasing bandwidth factor,  $B_f$ , of 1.5 and 3.43 respectively [10]. These translate to an equivalent windowed resolution bandwidth,  $RBW_{win}$ , of 15 Hz

(Hanning) and 34.3 Hz (flat-top) assuming a RBW of 10 Hz. Furthermore, these would degrade the noise floor,  $N$ , by 11.8 dB and 15.4 dB equivalently as opposed to the original 10 dB degradation:

$$RBW_{win} = RBW * B_f \text{ (Hz)} \quad (3.23)$$

As can be seen from Figure 3-12 and Figure 3-13, the signal is spread across multiple frequency bins when a windowing function is used. In particular, with the use of a Hanning window, the signal is spread from the main bin (peak) to two adjacent bins. In the case of a flat-top window the signal is spread from the main bin to six adjacent bins.

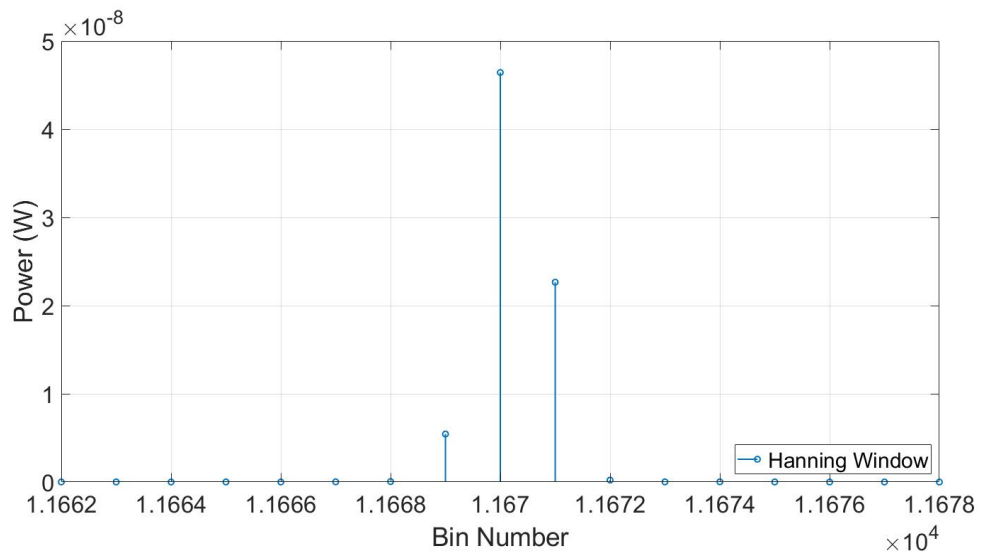


Figure 3-12: Signal spectrum with the use of Hanning window

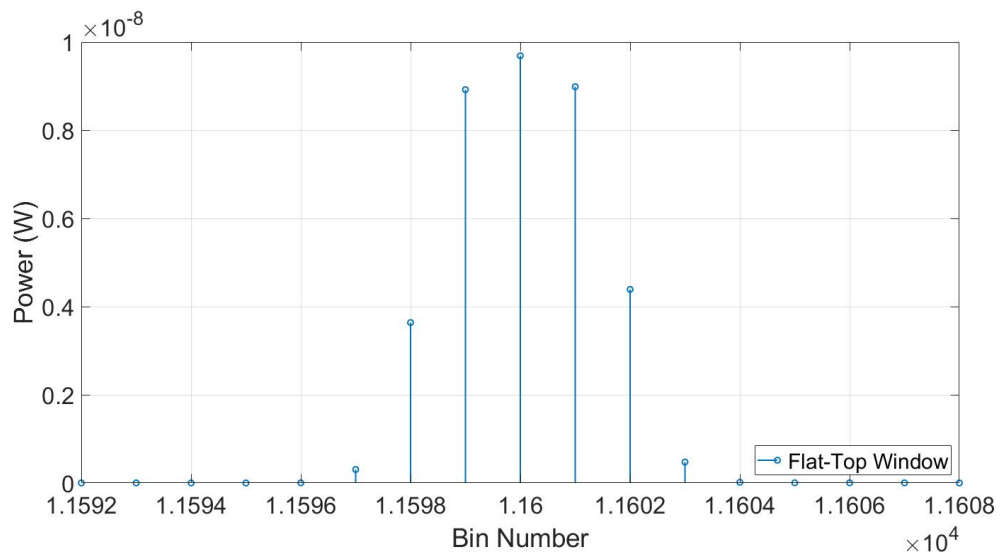


Figure 3-13: Signal spectrum with the use of flat-top window

Once the local oscillator of the USRP is adjusted to that of the incoming IF frequency, the signal is down-converted to baseband. Then the signal is sampled at a frequency of 327.68 kHz. A window function, flat-top in this case, is applied to the digitized samples. An FFT with length 32768 ( $2^{15}$ ) is then used to calculate the signal's power spectrum. This gives a RBW of 10 Hz. Furthermore, the bin with the highest magnitude is identified with the peak detector. The signal captured is centred in the spectrum and in the case that the signal drifts, it is adjusted by calculating the difference between the centre and the highest magnitude bin. The beacon power measurement is then done by summing the centre and adjacent bins according to the chosen windowing function. Concurrently, the surrounding integrated noise at a bandwidth of 100 kHz from the beacon is summed. The integrated received beacon and noise power are recorded at 10 Hz and 1Hz. Once calibrated, the integrated noise measurements can be used to calculate the sky noise temperature and digital radiometry can take place [11]. The described digital signal processing (DSP) block diagram is depicted in Figure 3-14. The DSP algorithm has been written and compiled using Python programming language. A timestamped file is generated with the measured beacon and noise power. The DSP code is executed on a Linux based (Ubuntu 18.04 LTS Bionic Beaver) environment.

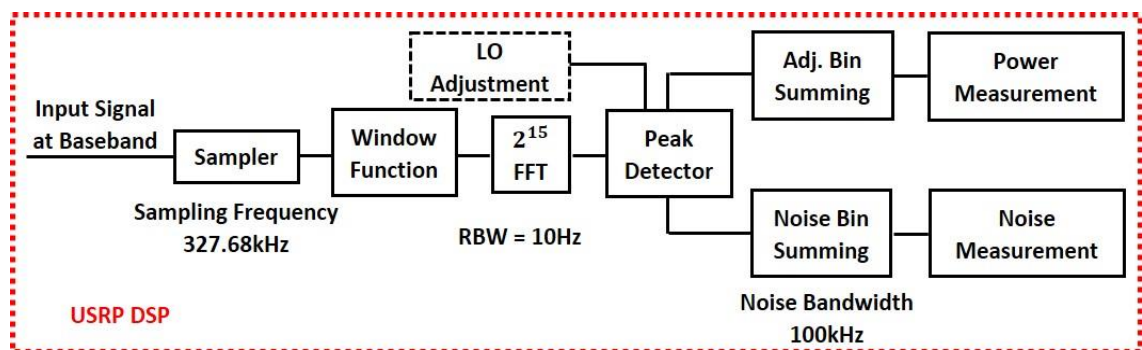


Figure 3-14: USRP DSP block diagram

### 3.4 Experimental Results

With the electrical, mechanical and signal processing in place, the Aldo Paraboni Ka-band beacon signal was first captured during a clear sky day. The captured beacon signal and its spectrum with two different window functions is shown in Figure 3-15. The CNR with the use of a Hanning window is at 38.7 dB while with a flat-top window it is at 35.0

dB. From the link budget calculation in Table 3-7, the CNR calculated is at 41.4 dB with a RBW of 10 Hz. With the use of window functions the windowed RBW,  $RBW_{win}$ , as calculated in (4.2) will have additional losses of 1.8 dB and 5.4 dB for the Hanning and flat-top window respectively. Therefore, the theoretically expected CNR is 39.6 dB and 36.0 dB which is close to the recorded measurements (1 dB less). Furthermore, the theoretical 3.6 dB difference between the different windowing functions is demonstrated experimentally in Figure 3-15.

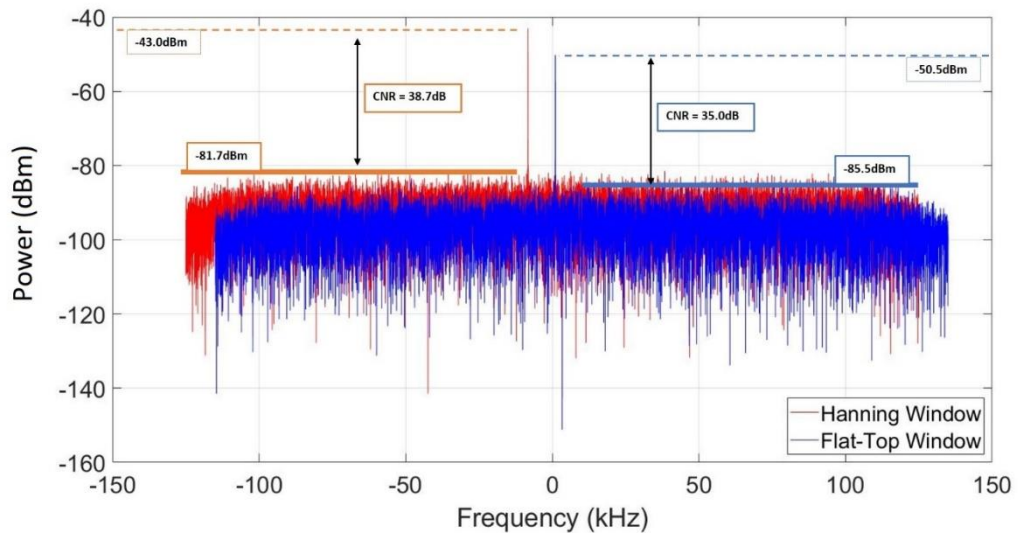
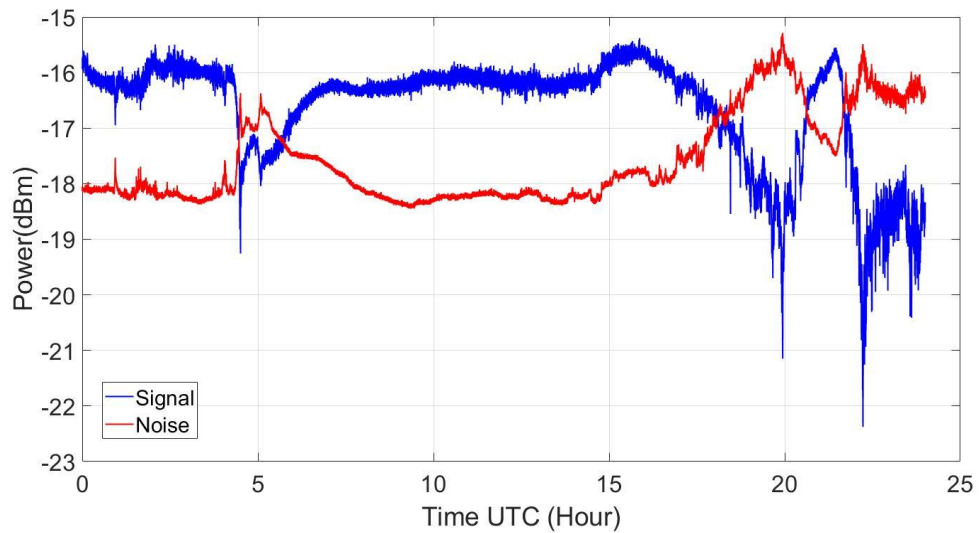


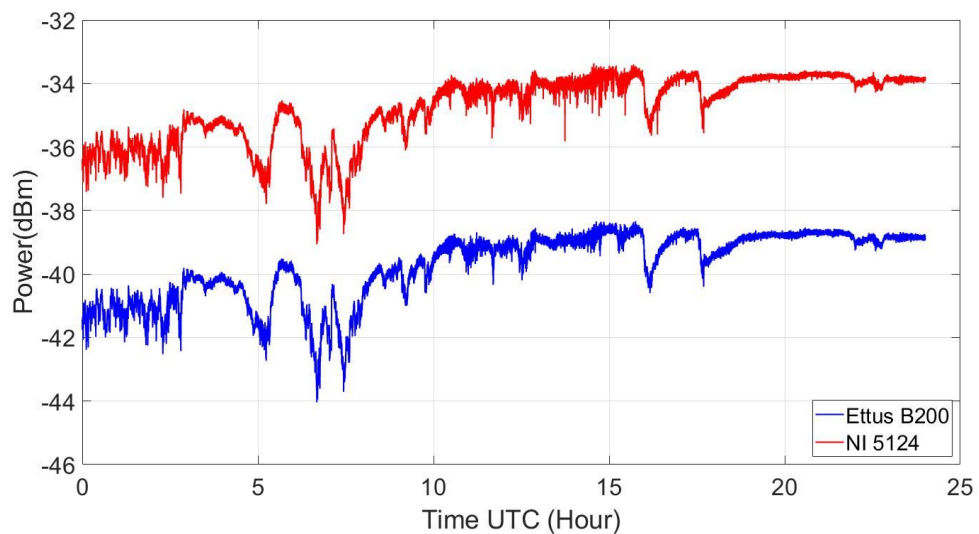
Figure 3-15: Beacon spectrum captured with the use of a Hanning (red) and flat-top (blue) window function

Figure 3-16 plots the captured beacon signal power and the noise around the beacon signal in a bandwidth of 100 kHz. As can be seen, the recorded noise power tracks the events occurring in the sky. For example, sky noise increases during fading at the hours around 5, 20 and 23.



*Figure 3-16: USRP recorded beacon and noise power*

As mentioned earlier, the Ka-band beacon signal and noise are recorded by a terminal built by NASA Glenn Research Centre that uses a National Instruments (NI) 5124 data acquisition card. The recorded beacon and noise power were validated with the recordings from the NASA terminal as shown in Figure 3-17 and Figure 3-18. An offset was applied to Figure 3-17 and Figure 3-18 to illustrate that the Ettus 200 USRP with the digital processing described in Section 3.3 is able to successfully track and record the integrated power and noise. The Nasa terminal is considered the benchmark. Moreover, identical performance was achieved with equipment that costs ten times less than the Nasa terminal. The Ettus B200 and NI 5124 card cost €785 and €9,860 respectively [9], [12].



*Figure 3-17: Beacon power received comparison with the B200 and NI 5124 card*



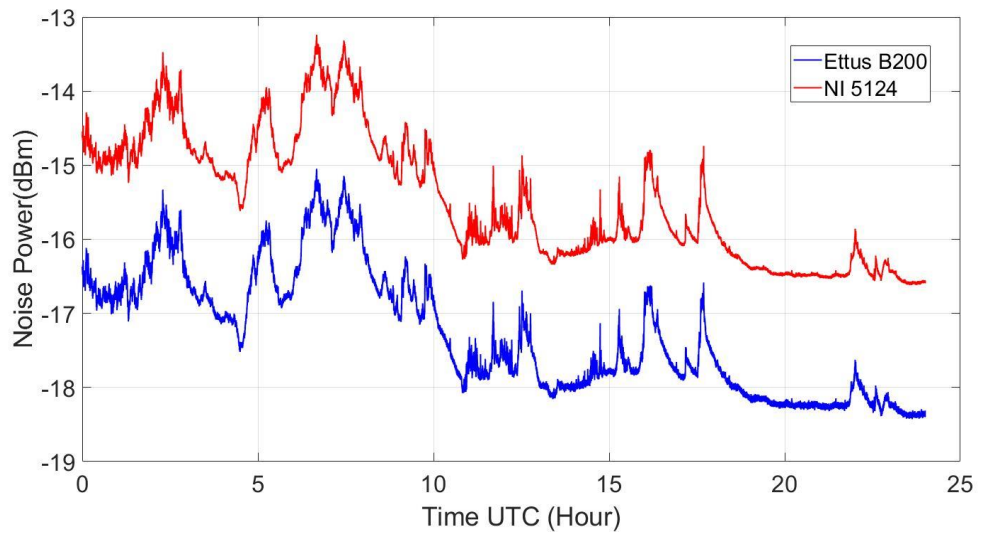


*Figure 3-18: Noise power recorded comparison with the B200 and NI 5124 card*

During deep atmospheric fading there is the possibility of losing the beacon signal. Therefore, the recovery of the beacon signal is important for the continuous operation of the terminal. An experiment was conducted where the input cable was disconnected and reconnected in an effort to see how the terminal would respond to a loss of the beacon signal. Figure 3-19 shows the loss at 16.519 hour and recovery at 16.528 hour of the beacon signal.

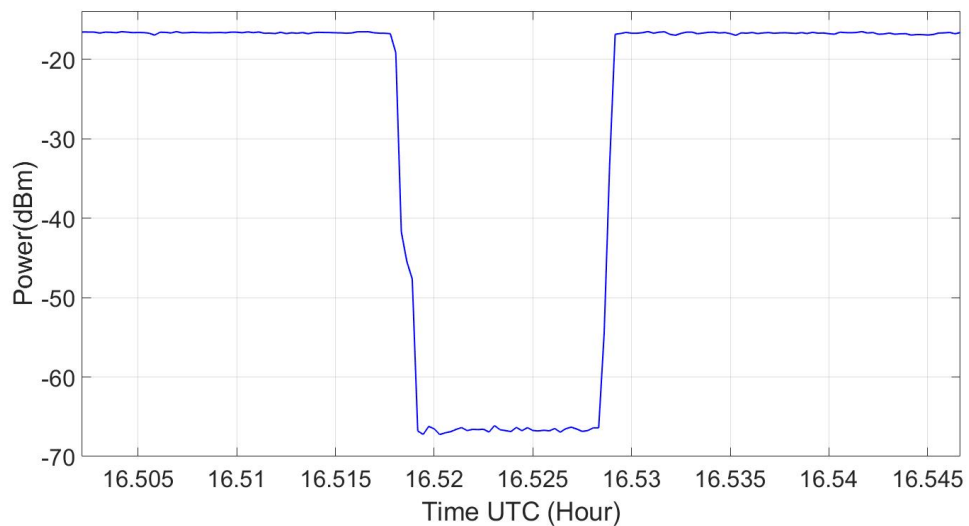


*Figure 3-19: Beacon signal recovery experiment*

### 3.5 Excess Atmospheric Attenuation

A useful propagation parameter is that of the excess atmospheric attenuation. Excess atmospheric attenuation does not take into account the ever-present gaseous attenuation. This can be obtained by calculating a zero-dB reference level from the recorded beacon signal power. The received beacon signal in time,  $S(t)$ , can be expressed as [13]:

$$S(t) = S_{vac}(t) - Att_{gas}(t) - Att_{exc}(t) \text{ (dBm)} \quad (3.24)$$

where  $S_{vac}(t)$  is the signal relative to a vacuum and under normal circumstances will vary slowly due to system imperfections, and  $Att_{gas}(t)$  is the oxygen and water vapour absorption attenuation (gaseous absorption) and is also slowly varying.  $Att_{exc}(t)$  is the attenuation due to rain, clouds and scintillation which has a faster variation compared to the other two quantities. Therefore, the excess atmospheric attenuation in time,  $S_{exc}(t)$ , can be calculated as:

$$S_{exc}(t) = S(t) - Ref_{zero}(t) \text{ (dBm)} \quad (4.25)$$

where  $Ref_{zero}(t)$  is the zero-dB reference level which would include any system variation imperfection and gaseous absorption. The first step is identifying the clear sky segment. This is achieved by first segmenting the data (e.g. in 10-minute segments) and calculating the mean and standard deviation of the segment's received signal. When the criteria are met, the segments are flagged as clear sky segments. Next, the clear sky segments are fitted via a Fourier series process as described in [13]. Figure 3-20 shows the Ka-band recorded beacon signal,  $S(t)$ , for a span of 5 days in blue with the identification of clear sky segments in red. The zero-dB reference level is shown in black. Figure 3-21, shows the approximate excess atmospheric attenuation,  $S_{exc}(t)$  of the five

day

timeseries.

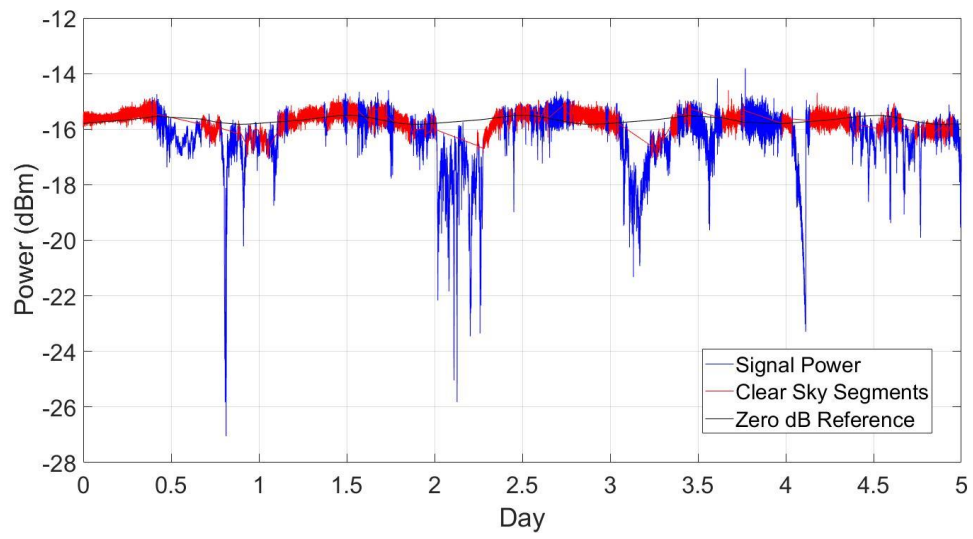


*Figure 3-20: Received beacon signal (blue), identified clear sky segments (red) and zero-dB reference level fitted with Fourier series (black)*

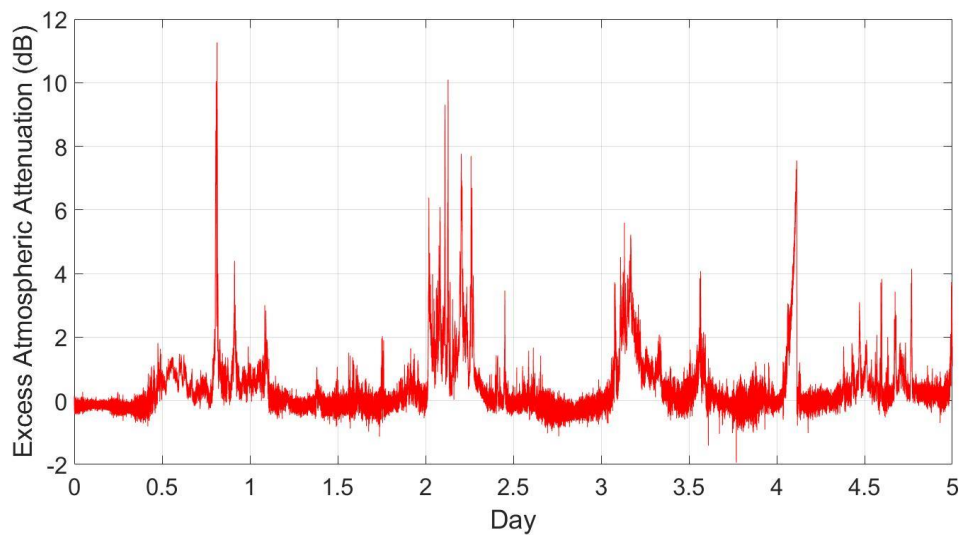


*Figure 3-21: Approximated excess attenuation*

### 3.6 Conclusion

The successful design and implementation of a Ka-band receiver for propagation measurements at Heriot-Watt University has been described. The receiver demonstrated a CNR of 35 dB. The overall design was centred around the idea of using a USRP for capturing the signal and SDR for processing the data in an effort to reduce the cost. This was achieved with the use of a commercial LNB which down-converted the Aldo Paraboni Ka-band signal (19.701 GHz) to 1.451 GHz. Next, the signal did not require further down-conversion because the Ettus B200 USRP was used to capture the IF signal.

The measurements collected are an important part of modelling the atmospheric impairments at the band of operation. With the current setup and measurements, gaseous attenuation can be calculated with the use of the European Centre for Medium-Range Weather Forecasts vertical profiles as described in [14]. Furthermore, the methodology for calculating the excess atmospheric attenuation that was shown, can provide datasets that include cloud and rain attenuation along with scintillation. Also, with the calibration of the integrated noise, atmospheric noise measurements can be executed in an effort to monitor the sky and fading without the need for a beacon [11].

In the case of a new propagation campaign for characterising the atmosphere in W-band for example, the acquired knowledge can be used to design and implement a ground receiver.

## References

- [1] S. Ventouras *et al.*, “Assessment of spatial and temporal properties of Ka/Q band earth-space radio channel across Europe using Alphasat Aldo Paraboni payload,” *Int. J. Satell. Commun. Netw.*, vol. 37, no. 5, pp. 477–501, 2019, doi: 10.1002/sat.1313.
- [2] M. Bergmann *et al.*, “Q/V-band feeder links and flexible bandwidth assignment in future very high throughput satellite (VHTS) communication systems,” in *23rd KA and Broadband Communications*, 2017.
- [3] ViaSat, “VIASAT-2 AT A GLANCE.” [https://www.viasat.com/sites/default/files/media/documents/770853\\_vs-2\\_2019\\_infographic\\_009\\_lores.pdf](https://www.viasat.com/sites/default/files/media/documents/770853_vs-2_2019_infographic_009_lores.pdf).
- [4] D. M. Pozar, *Microwave Engineering*, Second Edi. Wiley, 1998.
- [5] C. A. Balanis, *Antenna Theory - Analysis and Design*, Fourth edi. Wiley, 2016.
- [6] G. Maral and M. Bousquet, *Satellite Communication Systems*. John Wiley & Sons, 1986.
- [7] F. S. Marzano and M. Montopoli, “Millimeter-wave antenna noise temperature due to rain clouds: Theoretical model and statistical prediction,” in *3rd European Conference on Antennas and Propagation (EuCAP 2009)*, 2009, no. 1, pp. 2906–2910.
- [8] F. Machado, E. Vilar, F. P. Fontán, V. Pastoriza, and P. Mariño, “Easy-to-build satellite beacon receiver for propagation experimentation at millimeter bands,” *Radioengineering*, vol. 23, no. 1, pp. 154–164, 2014.
- [9] Ettus, “USRP B200/B210 Bus Series Spec Sheet.” [https://www.ettus.com/wp-content/uploads/2019/01/b200-b210\\_spec\\_sheet.pdf](https://www.ettus.com/wp-content/uploads/2019/01/b200-b210_spec_sheet.pdf).
- [10] Siemens, “Window Types: Hanning, Flattop, Uniform, Tukey, and Exponential,” 2019. <https://community.sw.siemens.com/s/article/window-types-hanning-flattop-uniform-tukey-and-exponential>.

- [11] A. Costouri, J. Nessel, and G. Goussetis, "Validation of a Digital Noise Power Integration Technique for Radiometric Clear Sky Attenuation Estimation at Q-Band," *Trans. Antennas Propag.*, pp. 1–9.
- [12] National Instruments, "PXI-5124," 2019. <https://www.ni.com/en-lb/support/model.pxi-5124.html>.
- [13] S. Ventouras, P. G. Davies, and J. R. Norbury, "Olympus-based propagation measurements in southern UK," *Antennas Propag.*, vol. 1, no. 407, pp. 27–31, 1995.
- [14] J. Nessel, M. Zemba, J. Morse, L. Luini, C. Riva, and A. R. Hardware, "Preliminary Statistics from the NASA Alphasat Beacon Receiver in Milan , Italy," in *9th European Conference on Antennas and Propagation (EuCAP 2015)*, 2015, pp. 1–5.

## Chapter 4

# 4 Atmospheric Noise and Digital Radiometry at Q-Band

### 4.1 Introduction

The trends towards broadband services, high-throughput satellites and reduction of the per Mbps cost drives the use of ever higher frequencies in satellite communications. While the use of Ka-band is now well established, there is an increasing interest in higher bands such as Q/V-bands (40/50 GHz) [1] and W-band [2]. Broad bandwidths available at these frequency bands offer attractive opportunities for exploitation in the feeder links, since they can support high capacity with fewer gateways. Consequently, the cost of the ground segment is reduced while the entire Ka-band becomes available for revenue-raising user links [3]. The aforementioned developments motivate the characterisation of atmospheric propagation effects and their properties at mm-wave frequencies. An early campaign to experimentally characterise atmospheric propagation effects beyond the Ka-band was made with the ITALSAT F1 satellite which carried beacons covering Europe at three bands, i.e. Ka-, Q- and V-band (20, 40 and 50 GHz respectively) [4], [5]. Presently, the Aldo Paraboni payload hosted on-board the ALPHASAT satellite delivers beacons with similar coverage at Ka- and Q-band (19.701, 39.402 GHz) underpinning an ongoing Europe-wide test campaign [6], [7]. Anticipating future needs for characterisation at W-band, ESA is currently making preparations for a beacon at these frequencies in geostationary orbit [2].

While beacons on-board geostationary satellites provide a very accurate methodology to characterise the channel from this orbit, such missions are costly and typically require long developments prior to launching. To this end alternative methodologies are currently explored such as the characterization of W-Band propagation using CubeSats [8] or from purely ground-based observations [9]. In particular, passive cosmic background radiometry represents a popular methodology to characterise atmospheric fading [10].

This technique is based on measuring received noise from a portion of the sky without radio emitters. By virtue of calibrating the received noise, which is a combination of atmospheric emission and cosmic background radiation, atmospheric fading can be estimated without relying on a spaceborne beacon. This methodology delivers its maximum accuracy when the effects of larger atmospheric particles can be neglected, e.g. in the absence of precipitation.

The primary aim of this chapter is to experimentally evaluate the potential of a software defined radio (SDR) receiver to deliver aforementioned passive radiometry measurements and characterize the geostationary channel at the satellite downlink without disrupting nominal operations. This is achieved by virtue of measurements performed with a bespoke terminal designed to receive the Q-band signal from the beacon of the Alphasat Aldo Paraboni payload [11]. By virtue of the SDR setup, where a downconverted image of the received signal is sampled and digitally processed to obtain its spectrum, it is possible to simultaneously record the level of the intended signal (in this case, a CW beacon), as well as the noise in the nearby frequency band. The specific configuration enables an accurate comparison of the atmospheric attenuation derived from the radiometer, with that obtained from the beacon observation. Earlier work such as [12] and [13], concurrently recorded the beacon satellite signal and noise power at Ka- and Q- band in which the calibration of the radiometer in post-processing required the satellite beacon measurements. Furthermore, in [14] and [15] the concurrent recordings helped to monitor events and obtain reference levels to estimate attenuation templates. The proposed configuration has the advantage of offering operational ground stations the ability to monitor fading in real time without additional hardware.

The remainder of the chapter is organised as follows. Section 4.2 outlines the theory underpinning atmospheric propagation and more precisely radiometer measurements. Section 4.3 presents the calibration methods of the radiometer. Section 4.4 presents some details of the system and the performed calibrations. Section 4.5 presents the comparative experimental results between fading obtained from the beacon and the radiometric measurements. Finally, conclusions are presented in Section 4.6.



## 4.2 Atmospheric Propagation of an Electromagnetic Wave

This section is divided into three main subsections. The first subsection refers to the relation between a blackbody and temperature through the Rayleigh-Jeans approximation. The second subsection states the radiative transfer equation. The last subsection describes signal attenuation through the atmosphere and concludes on the relation between atmospheric temperatures and attenuation due to absorption.

### 4.2.1 Blackbody and Temperature Relation

A blackbody is thought of as a perfectly opaque material that absorbs all incident radiation at all frequencies and reflects none. A blackbody is also a perfect emitter. This is because a blackbody is in thermodynamic equilibrium which means that it will emit the same amount of energy it absorbs [16].

The amount of energy it gives off as radiation at different frequencies is the called spectral brightness intensity,  $I_f$ , and can be calculated from Planck's law of blackbody radiation [17]:

$$I_f = \frac{2hf^3}{c^2} \left( \frac{1}{e^{hf/kT} - 1} \right) (\text{Wm}^{-2}\text{sr}^{-1}\text{Hz}^{-1}) \quad (4.1)$$

where,  $h$  is Planck's constant ( $6.63 \times 10^{-34}$  J),  $k$  is Boltzmann's constant ( $1.38 \times 10^{-23}$  JK<sup>-1</sup>),  $c$  is the speed of light in vacuum ( $3 \times 10^8$  ms<sup>-1</sup>),  $f$  is the frequency (in Hz) and  $T$  is the temperature (in Kelvin).

The power of a lossless receiving antenna that is surrounded by a blackbody can be calculated with the use of the spectral brightness intensity with respect to its frequency:

$$P_f = I_f A_r \Omega_s (\text{WHZ}^{-1}) \quad (4.2)$$

where,  $A_r$  is the receiving aperture area that subtends a solid angle  $\Omega_s$ . These two can be obtained with the range,  $R$ , between the source and the receiving antenna aperture as follows:

$$\Omega_s = \frac{A_r}{R^2} (\text{sr}) \quad (4.3)$$

$$\Omega_r = \frac{A_s}{R^2} \text{ (sr)} \quad (4.4)$$

where,  $A_s$  is the source area that subtends a solid angle  $\Omega_r$ . By considering a lossless antenna surrounded by a blackbody with spectral brightness intensity  $I_f$ , having a radiation pattern of  $F(\theta, \varphi)$  and effective aperture  $A_r$ , the differential spectral brightness power  $dP_f$  can be calculated by also taking into account the differential solid angle  $d\Omega$ :

$$dP_f = I_f A_r F(\theta, \varphi) d\Omega \quad (4.5)$$

The total amount of power received by the antenna over a range of frequencies  $f_1$  to  $f_2$  is:

$$P_f = A_r \int_{f_1}^{f_2} \iint_{4\pi} I_f F(\theta, \varphi) d\Omega df \quad (4.6)$$

Keeping in mind that an antenna will only intercept on average half of the energy incident upon its aperture and by using the Rayleigh-Jeans approximation instead of Planck's Law, the blackbody's power can be obtained.

#### 4.2.1.1 Rayleigh-Jeans Approximation

The Rayleigh-Jeans approximation, which essentially is the first term of the Taylor expansion of eq. (4.1) is as follows [16]:

$$I_f \approx \frac{2kT}{\lambda^2} \text{ (WHz}^{-1}\text{)} \quad (4.7)$$

where,  $I_f$  is the approximation of the spectral brightness intensity,  $k$  is Boltzmann's constant,  $T$  is the temperature in Kelvin and  $\lambda$  is the wavelength in meters.

On this basis and considering (4.6), the power intercepted by the antenna, enclosed in a blackbody is [16]:

$$P_{bb} = kTB \frac{A_r}{\lambda^2} \iint_{4\pi} F(\theta, \varphi) d\Omega \text{ (W)} \quad (4.8)$$

Since the normalised radiation intensity  $F(\theta, \varphi)$  over a sphere is [16]:

$$\Omega_p = \iint_{4\pi} F(\theta, \varphi) d\Omega \quad (\text{sr}) \quad (4.9)$$

And the pattern solid angle  $\Omega_p$ , which is the width of the antenna's mainlobe pattern is [16]:

$$\Omega_p = \frac{\lambda^2}{A_r} \quad (\text{sr}) \quad (4.10)$$

Solving (4.8) by substituting (4.10) will yield the power detected by the antenna, enclosed in a blackbody as such [16]:

$$P_{bb} = kTB \quad (\text{W}) \quad (4.11)$$

where  $P_{bb}$  is equal to the Boltzmann's constant  $k$  multiplied by the temperature  $T$  in Kelvin over a bandwidth  $B$ . This equation shows a direct relation between power emitted by a blackbody source and its temperature. Using this equation, the power detected by an antenna that is enclosed in a blackbody can be expressed in temperature and vice versa.

Furthermore, the spectral brightness intensity of a blackbody is the following [16]:

$$I_{bb} = I_f B = \frac{kT}{\lambda^2} B \quad (\text{WHz}^{-1}) \quad (4.12)$$

#### 4.2.2 Radiative Transfer Equation

Radiative transfer theory is very important in understanding how a wave propagates in a medium. The two aspects to be looked at are the absorption and emission from a medium, when a wave propagates through. In free space, the spectral brightness intensity  $I_f$  of radiation is conserved along a ray:

$$\frac{dI_f}{ds} = 0 \quad (4.13)$$

where,  $I_f$  is the spectral brightness intensity and  $s$  is the distance of the source to the antenna.

#### 4.2.2.1 Absorption

By thinking of a ray as a beam of photons, when passing through a medium, some will be absorbed. Therefore, we can introduce the linear absorption coefficient  $\kappa_v$ , which is equal to the infinitesimal probability of photons with frequency  $f$  that will be absorbed ( $dp_f$ ) over a thin slab of thickness  $ds$ :

$$\kappa_v \equiv \frac{dp_f}{ds} \quad (4.14)$$

$$dp_f = \kappa_v ds \quad (4.15)$$

The fraction of specific brightness intensity lost to absorption in the infinitesimal distance  $ds$  along the ray will be:

$$\frac{dI_f}{I_f} = -dp_f = -\kappa_f ds \quad (4.16)$$

Integrating equation (4.16) with the limits of distance  $s_{in}$  (source) to  $s_{out}$  (antenna), we obtain:

$$I_f(s_{out}) = I_f(s_{in}) \exp\left(-\int_{s_{in}}^{s_{out}} \kappa_f(s) ds\right) \quad (4.17)$$

Defining opacity as a fraction of electromagnetic impenetrability, we have:

$$I_f(s_{out}) = I_f(s_{in}) \exp(-\tau_f) \quad (4.18)$$

The above equation is true only for absorption effects.

#### 4.2.2.2 Emission

A medium may also emit photons. In a small volume of  $dsd\sigma$ , the probability of a photon at a frequency  $f$  to be emitted into the solid angle  $d\Omega$  is directly proportional, i.e.:

$$Probability_{emission} \propto dsd\sigma d\Omega$$

The emission coefficient  $e_f$  can also be introduced as:

$$e_f = \frac{dI_f}{ds} \quad (4.19)$$

#### 4.2.2.3 Equation of Radiative Transfer

Combining both the emission and absorption will yield the equation of radiative transfer:

$$\frac{dI_f}{ds} = -k_f I_f + e_f \quad (4.20)$$

#### 4.2.2.4 Kirchhoff's Law of Thermal Radiation

Kirchhoff's law of Thermal Radiation states that:

*“For a body of any arbitrary material emitting and absorbing thermal electromagnetic radiation at every wavelength in thermodynamic equilibrium, the ratio of its emissive power to its dimensionless coefficient of absorption is equal to a universal function only of radiative wavelength and temperature. That universal function describes the perfect blackbody emissive power.”*

Therefore, the following relation can be made:

$$B_f(T) = \frac{e_f(T)}{k_f(T)} \quad (4.21)$$

where,  $B_f(T)$  is the universal function described in Kirchhoff's law and  $e_f(T)$  and  $k_f(T)$  are the emission and absorption coefficient respectively. In order for this equation to be true, the medium has to be in thermodynamic equilibrium. Furthermore, Kirchhoff's law can be applied in both thermal equilibrium and local thermodynamic equilibrium like the atmosphere.

## 4.2.3 Description of Signal Attenuation in the Atmosphere

### 4.2.3.1 Signal Extinction

As the electromagnetic signal propagates through the atmosphere, it experiences scattering and absorption, such that an incoming signal strength will weaken as it propagates. The signal attenuation along a path is also referred to as the extinction of the signal, excluding any free space losses (FSL). This attenuation is caused from scattering and absorption. This can be described by the following terms:

$$A_t = A_{ab} + A_{sc} \text{ (dB)} \quad (4.22)$$

where,  $A_t$  is the total attenuation/extinction along the signal path (excluding FSL),  $A_{ab}$  is the absorption attenuation/extinction and  $A_{sc}$  is the scattering attenuation/extinction. These signal attenuations caused by the atmosphere are also related to the sky noise temperature as described in Section 4.2.4.

### 4.2.3.2 Air Mass

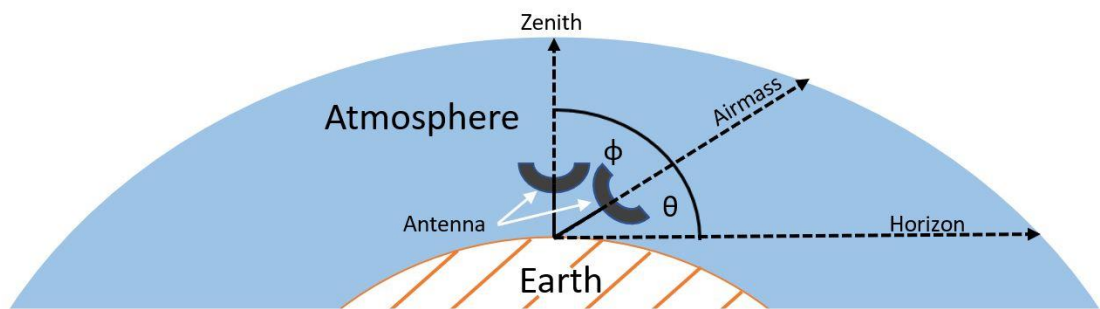


Figure 4-1: Illustration of airmass

Air mass is the optical path length, normalised to that at zenith, that a signal must go through when travelling through the Earth's atmosphere. As the signal goes through the atmosphere, it experiences scattering and absorption. The closer the target is to the horizon, the more air (gases) are needed to be looked through and the more degraded the view gets, as it can be seen in Figure 4-1. Therefore, the longer the path through the

atmosphere, the higher the air mass and consequently the higher the attenuation. Moreover, the air mass at zenith (90° elevation angle) is 1 and increases as the elevation angle decreases.

When the elevation angle  $\theta$ , is large, a good approximation is given by assuming a homogeneous plane-parallel atmosphere (i.e. one for which density is constant and the Earth's curvature is ignored). Air mass can be calculated from the following equation [18][19]:

$$Air\ mass = \frac{1}{\sin \theta} = \frac{1}{\cos \varphi} = cosec \theta \text{ (airmass)} \quad (4.23)$$

where,  $\theta$  is the elevation angle and  $\varphi$  is the zenith angle.

At a zenith angle ( $\varphi$ ) of 60°, the air mass is approximately 2. The Earth is not flat, however, and, depending on accuracy requirements, this formula is usable for zenith angles up to 75°. At greater zenith angles, the accuracy degrades rapidly, with air mass as obtained by equation (4.23) becoming infinite at the horizon; the horizon air mass in the more-realistic spherical atmosphere is usually less than 40 [20].

#### 4.2.3.3 Opacity

Opacity is often referred to as optical depth [16]. It is the quality of lacking transparency or translucence. It is a measure of impenetrability to electromagnetic or other kinds of radiation. As seen from the absorption section on the radiative transfer equation, opacity is linked to the absorption coefficient,  $k_f$  as follows:

$$\tau_f = \int_{S_{out}}^{S_{in}} -k_f(s) ds \quad (4.24)$$

##### 4.2.3.3.1 Link between Air Mass and Opacity

There is a link between opacity and air mass. As discussed previously, air mass is the optical path length through the atmosphere. An air mass of zero is physically impossible since the atmosphere is always present. Nonetheless, an air mass of zero would

theoretically conclude as to not having an atmosphere and therefore, signal attenuation from just free space losses.

Likewise, an opacity of zero would suggest that electromagnetic radiation can penetrate unobstructed. Therefore, an opacity of zero would suggest no attenuation, except for free space losses.

Finally, when plotting a graph of opacity vs air mass, the relation will be linear and when extrapolating the plot, it should start from zero (zero air mass and zero opacity). This relation can help when calibrating a radiometer. This will be discussed in Section 4.3.

Based on the above discussion, the opacity at a zenith angle  $\varphi$  can then be obtained from [21]:

$$\tau(\varphi) = \tau_o \sec \varphi \quad (4.25)$$

where,  $\tau_o$  is the zenith opacity.

#### 4.2.3.4 Fractional Transmissivity, $\sigma$

An absorbing medium in thermal equilibrium, like the atmosphere, will radiate as much incident energy as it absorbs. The efficiency of absorption can be described by the fractional transmissivity,  $\sigma$ , of the atmosphere. A fractional transmissivity of unity means that there is no absorption and a fractional transmissivity of zero that there is absolute absorption, i.e. no transmitted power [22].

##### 4.2.3.4.1 Relation between Transmissivity, Attenuation and Opacity

Transmissivity is the link between opacity and attenuation. The attenuation due to absorption of a signal can be obtained from the transmissivity of the atmosphere as follows [22]:

$$A_{ab} = 10 \log_{10} \left( \frac{1}{\sigma} \right) \text{ (dB)} \quad (4.26)$$



Transmissivity,  $\sigma$ , can be expressed in terms of opacity,  $\tau$ , through the following equation [16]:

$$\sigma = e^{-\tau} = e^{-\tau_o \sec \varphi} \quad (4.27)$$

where,  $\sigma$  is the transmissivity and  $\tau_o$  is the zenith opacity at  $\varphi = 0^\circ$ .

#### 4.2.4 Noise, Temperature and Signal Absorption

The **brightness temperature** of a material  $T_B$ , or in our case the atmosphere, is the equivalent temperature of a blackbody that emits the same spectral brightness intensity,  $I_f$ , as the material under consideration (equation (4.12)) [16].

Brightness temperature is also sometimes referred to as the **sky noise temperature**  $T_r$ . It is called sky noise temperature because the receiving antenna will experience an increase in noise temperature due to the attenuating medium that itself is radiating (because it is in a thermal equilibrium, isotropic) [22].

The **mean brightness temperature**,  $T_m$ , is the physical temperature of the atmosphere/absorbing medium [22]. Available guidelines (ITU-R P.618-13, [23]) provide empirical expressions to obtain  $T_m$  as a function of the surface temperature,  $T_s$ , for clear and cloudy weather, as below:

$$T_m = 37.34 + 0.81 T_s \text{ (K)} \quad (4.28)$$

In addition to the blackbody radiation in the atmosphere, further contribution comes from the cosmic and the galactic radiations. The cosmic radiation is due to the remnants from the Big Bang while the galactic radiation is due to radiation from our galaxy. These are respectively associated with the **cosmic and galactic brightness temperature**,  $T_c$  and  $T_g$  respectively.  $T_c$  brings a contribution to the brightness temperature between 2-3 K. In the following calculations,  $T_c$  will have a constant value of 2.7 K [16], [22]. The galactic radiation varies with frequency, depending on the specific region of the galaxy. The galactic brightness temperature can be ignored for frequencies above 5 GHz and should be considered for frequencies below 1 GHz [16].

The signal with power  $S$ , when passing through the medium/atmosphere will result in an attenuation and a resulting power of  $\sigma S$ , where  $\sigma$  is the fractional transmissivity.

If the medium, has a temperature  $T_m$ , the noise produced by the medium/atmosphere can also be calculated. The brightness temperature,  $T_B$ , is directly linked with the emitted radiation of the medium/atmosphere, since it is in thermal equilibrium.

From the Rayleigh-Jeans approximation, the brightness temperature can be obtained from:

$$T_B(f) \equiv \frac{I_f c^2}{2k f^2} \quad (4.29)$$

Furthermore, solving the radiative transfer equation for a medium in local thermodynamic equilibrium, the atmosphere and the brightness temperature  $T_B$  can be linked to the physical temperature  $T_m$  and opacity  $t_\varphi$ .

The first step is to eliminate the emission coefficient  $e_f$  with:

$$e_f = k_f B_f(T_m) \quad (4.30)$$

where,  $k_f$  is the absorption coefficient and  $B_f(T_m)$  is the universal transfer function with respect to physical temperature  $T_m$ :

$$\frac{dI_f}{ds} = -k_f I_f + k_f B_f(T_m) \quad (4.31)$$

The absorption coefficient  $k_f$  can also be eliminated by multiplying the equation by  $1/k_f$ .

Then, by referring to (4.24) the equation can be re-written as:

$$\frac{1}{k_f} \frac{dI_f}{ds} = -\frac{dI_f}{d\tau} = -I_f + B_f(T_m) \quad (4.32)$$

Both sides of the differential equation are multiplied with  $\exp(-\tau)$  and integrated along the path of the signal from the top of the atmosphere to the ground. The limits of the integrals are from 0 to  $\tau(\varphi)$  where,  $\tau(\varphi)$  is the opacity of the atmosphere at zenith angle  $\varphi$ .

$$\int_0^{\tau(\varphi)} e^{-\tau} \frac{dI_f}{d\tau} d\tau = \int_0^{\tau(\varphi)} [I_f - B_f(T_m)] e^{-\tau} d\tau \quad (4.33)$$

By solving the above equation and neglecting the spectral brightness  $I_f(\tau = \tau(\varphi))$ , as the brightness of emission above the atmosphere is relatively low at high frequencies, the following equation arises:

$$I_f = (1 - e^{-\tau(\varphi)}) B_f(T_m) \quad (4.34)$$

This can therefore be re-written as:

$$I_f = (1 - e^{-\tau_o \sec \varphi}) \frac{2kf^2 T_m}{c^2} \quad (4.35)$$

Combining (4.29) and (4.35) the sky noise temperature/brightness temperature  $T_B$  can be written as:

$$T_B = \frac{I_f c^2}{2kf^2} = T_m [1 - e^{(-\tau_o \sec \varphi)}] \quad (4.36)$$

Reconsidering the transmissivity, (4.27), the brightness temperature  $T_B$ , can be re-written as [22]:

$$T_B = T_m(1 - \sigma) \quad (\text{K}) \quad (4.37)$$

$$\sigma = \frac{T_m - T_B}{T_m} \quad (\text{unitless}) \quad (4.38)$$

Brightness temperature,  $T_B$ , can then be also expressed in terms of attenuation due to absorption,  $A_{ab}$ , and mean brightness temperature,  $T_m$ :

$$T_B = T_m \left(1 - e^{-\left(\frac{A_{ab}}{4.34}\right)}\right) \quad (\text{K}) \quad (4.39)$$

Therefore, the signal attenuation is linked with the fractional transmissivity which in turns, is linked to the brightness temperature,  $T_B$ , and mean brightness temperature,  $T_m$  as follows:

$$A = 10 \log_{10} \left( \frac{T_m}{T_m - T_B} \right) \quad (\text{dB}) \quad (4.40)$$

As mentioned before, there is also a constant cosmic radiation. This permanent radiation  $T_c$  will therefore be included on the attenuation equation as follows [22]:

$$A_{ab} = 10 \log_{10} \left( \frac{T_m - T_c}{T_m - T_B} \right) \quad (\text{dB}) \quad (4.41)$$

The attenuation due to absorption is attributed to the interaction of electromagnetic radiation with gaseous molecules (primarily oxygen and water vapour in the 1-100 GHz range). At thermal equilibrium, energy transitions of these particles lead to emission and absorption of electromagnetic radiation at equal rates. With this assumption, a signal

propagating along a given path in the atmosphere will therefore experience atmospheric (or gaseous) absorption at the same rate [10]. Gaseous absorption dominates fading when, in the radiative transfer equation, the effects of scattering or other absorptive mechanisms of electromagnetic wave from atmospheric particles can be neglected [10]. This typically applies, for example, in the absence of precipitation. In this case, gaseous absorption can be characterised from measured noise power considering the thermodynamics of the atmosphere as briefly outlined next.

The above suggests that the gaseous absorption of the atmosphere can be estimated once values of the atmosphere's brightness temperature,  $T_B$ , are available. The latter can be obtained exploiting radiometric noise measurements. In particular, a lossless antenna enclosed in a blackbody in thermal equilibrium as discussed in (4.11) (which with the above approximation can be assumed to be the atmosphere) will detect the following noise power [16]:

$$P_N = kT_B B \text{ (W)} \quad (4.42)$$

where  $P_N$  is the noise power detected by the antenna over a certain bandwidth  $B$ , with  $k$  being the Boltzmann's constant and  $T_B$  the brightness temperature in Kelvin. Consequently, the noise temperature of a clear sky is proportional to the noise power recorded in an ideal receiver comprising a lossless antenna and noise-free electronics.

For practical receivers, additional considerations are required. The RF electronics generate noise that can be calculated from the noise figure of each component, which can then be converted to an equivalent noise temperature,  $T_r$  [24]. Furthermore, a practical antenna is not lossless but instead is characterized by a noise temperature,  $T_N$ . Moreover, in addition to the main lobe (which observes the desired brightness temperature,  $T_B$ ) the antenna also has side lobes that capture noise from unwanted sources,  $T_{sl}$ . The total gain,  $G$ , of the receiver system must also be taken into account, since gain applies to both the noise and desired signal. With the above considerations, (4.42) for a lossy receiver system becomes [16]:

$$P_N = (T_B + T_{sl} + T_r + T_N)kBG \text{ (W)} \quad (4.43)$$

Rearranging the equation to make brightness temperature the argument:

$$T_B = \frac{P_N}{kBG} - (T_{sl} + T_r + T_N) \text{ (K)} \quad (4.44)$$

Recognising the dependence of the brightness temperature,  $T_B$ , on the measured noise power,  $P_N$ , (4.44) can be written in the format:

$$T_B = aP_N + b \text{ (K)} \quad (4.45)$$

where the coefficients  $a$  and  $b$  stand for:

$$a = \frac{1}{kBG} \text{ (KJ}^{-1}\text{Hz}^{-1}\text{)} \quad (4.46)$$

$$b = -(T_{sl} + T_r + T_N) \text{ (K)} \quad (4.47)$$

### 4.3 Radiometer Calibration

While approximate estimations for the coefficients  $a$  and  $b$  can be obtained by (4.46) and (4.47), more accurate values can be obtained by performing experimental calibration to remove the system's gain, noise and antenna side lobes from the recorded noise power. A suitable method for calibrating the receiver exploits measuring the noise when the antenna is exposed to well-known brightness temperatures [16]. In particular, this method exploits the fact that an electromagnetic absorber covering the receiver antenna acts as an effective blackbody. Consequently, the brightness temperature seen by the antenna is in this case equal to the physical temperature of the absorber. By adjusting the temperature of the absorber to known values and recording the relevant noise power levels it is possible to obtain values for the coefficients  $a$  and  $b$ .

Since the number of unknown coefficients is two, only two temperatures (hot and cold) are required to perform the calibration. In practice this can be achieved by keeping the absorber in ambient temperature ( $T_b^h \approx 300$  K) or immersing it in a e.g. liquid nitrogen ( $T_b^c = 77$  K). After recording the noise power of a hot and cold source,  $a$  and  $b$  can be calculated from [16]:

$$a = \frac{T_b^h - T_b^c}{P_N^h - P_N^c} \text{ (KJ}^{-1}\text{Hz}^{-1}\text{)} \quad (4.48)$$

$$b = \frac{P_N^c T_b^h - P_N^h T_b^c}{P_N^h - P_N^c} \text{ (K)} \quad (4.49)$$

where the superscripts  $h$  and  $c$  stand for hot and cold source respectively.

Another method for obtaining the calibration coefficients is that of a tip curve calibration. A tip calibration exploits the fact that directions closer to the horizon experience longer paths through the atmosphere and consequently are associated with higher attenuation (and thus atmospheric noise) [21]. On the assumption that the atmosphere is homogeneous with constant density, the attenuation,  $A_{ab}$ , at a given elevation angle,  $\theta$ , is proportional to the optical path length at that angle normalised to that at zenith as described by (4.23).

On that basis, the attenuation  $A_{ab}$  at angle  $\theta$  is linked with the attenuation  $A_{ab90}$  at zenith ( $\theta = 90^\circ$ ) according to:

$$A_{ab} = A_{ab90} \operatorname{cosec} \theta = A_{ab90} \times \text{Air mass (dB)} \quad (4.50)$$

Equation (4.50) reveals that the relationship between airmass and attenuation is linear and the associated curve (also referred to as tip curve) crosses the origin. It is noted that although an air mass lower than unity is practically impossible, theoretically this extrapolation is meaningful. In particular, an air mass of zero corresponds to absence of the atmosphere and therefore no attenuation of a signal [16].

During tip calibration the antenna is pointed at different elevation angles, corresponding to different values for the air mass, and the noise power is recorded. An initial estimation of the zenith attenuation,  $A_{ab90}$  in dB, can be calculated by comparing two elevation angles [21]:

$$A_{ab90} = 4.343 \frac{1}{\operatorname{cosec} \theta - 1} \ln \left( \frac{T_{B90} - T_m}{T_B(\theta) - T_m} \right) \quad (4.51)$$

where,  $T_{B90}$  and  $T_B(\theta)$  are the brightness temperature at zenith and at an elevation angle  $\theta$  respectively. The temperatures  $T_{B90}$ ,  $T_B(\theta)$  and  $T_m$  in (4.51) are unknown. Given that, as per (4.45), the relationship between measured noise power and temperature is linear, (4.51) can be rewritten in terms of the associated integrated noise power levels:

$$A_{ab90} = \frac{1}{\operatorname{cosec} \theta - 1} \ln \left( \frac{P_N(T_{B90}) - P_N(T_m)}{P_N(T_B(\theta)) - P_N(T_m)} \right) \quad (4.52)$$

To a first approximation, the mean radiating temperature,  $T_m$ , can be replaced with that of the ambient air temperature  $T_a$ . In turn, the integrated noise power associated with the ambient temperature,  $P_N(T_a)$ , can be replaced with the observation of the brightness of a blackbody at ambient temperature. Therefore, (4.52) can be re-written as:

$$A_{ab90} = \frac{4.343}{\operatorname{cosec} \theta - 1} \ln \left( \frac{P_N(T_{B90}) - P_N(T_a)}{P_N(T_B(\theta)) - P_N(T_a)} \right) \quad (4.53)$$

and a first estimate of the calibration coefficients can be made as:

$$a_{est} = \frac{e^{-A_{ab90}/4.343}(T_c - T_a)}{P_N(T_{B90}) - P_N(T_a)} \quad (\text{KJ}^{-1}\text{Hz}^{-1}) \quad (4.54)$$

$$b_{est} = T_a - a_{est}(P_N(T_a)) \quad (\text{K}) \quad (4.55)$$

Next, we consider that the mean brightness temperature differs from the blackbody observed at ambient temperature

$$\Delta T = T_a - T_m \quad (\text{K}) \quad (4.56)$$

Consequently, the initial estimation of  $a_{est}$  can be used to find more accurate values of  $P_N(T_m)$  as

$$P_N(T_m) = P_N(T_a) - \frac{\Delta T}{a_{est}} \quad (\text{W}) \quad (4.57)$$

The updated calibration coefficients,  $a_{est*}$  and  $b_{est*}$ , and updated atmospheric attenuation at zenith,  $A_{ab90*}$ , can then be obtained by introducing (4.57) into (4.53)-(4.55):

$$A_{ab90*} = 4.343 \frac{1}{\operatorname{cosec} \theta - 1} \ln \left( \frac{P_N(T_{Bo}) - P_N(T_m)}{P_N(T_B(\theta)) - P_N(T_m)} \right) \quad (4.58)$$

$$a_{est*} = \frac{e^{-A_{ab90*}/4.343}(T_c - T_a - \Delta T)}{P_N(T_{Bo}) - P_N(T_a) - \frac{\Delta T}{a_{est}}} \quad (\text{KJ}^{-1}\text{Hz}^{-1}) \quad (4.59)$$

$$b_{est*} = T_a - \Delta T - a_{est*}(P_N(T_a)) \quad (\text{K}) \quad (4.60)$$

In a tip calibration process, the calibration coefficients are estimated for the original approximation  $T_m = T_a$ . Based on this estimation, the tip curve (i.e. attenuation vs. airmass) is then plotted. Typically, the original tip curve does not cross the origin due to the non-zero value of  $\Delta T$  in (4.56). To this end, an initial assumption of  $\Delta T$  is made and the updated calibration coefficients,  $a_{est*}$  and  $b_{est*}$  are calculated. Rapid convergence of the calibration coefficients is achieved by iterating (4.57) - (4.60) with the assumed  $\Delta T$ . The latest calculated calibration coefficients are used in each iteration. The correct calibration coefficients are calculated by adjusting  $\Delta T$  until the tip-curve plot extrapolates to zero.

## 4.4 SDR Receiver

The opportunities and limitations to characterise fading using the aforementioned radiometric approach at the Q-band satellite downlink frequency using a low-cost SDR receiver have been investigated by means of an experimental setup. The latter involves a Q-band receiver mounted on a pointing system shown in Figure 4-2 that tracks the Alphasat satellite using an open-loop system based on ephemeris data. The remainder of this section provides a description of the SDR receiver and its calibration.



*Figure 4-2: Photograph of the beacon receiver*

### 4.4.1 System description

The RF and digital signal processing (DSP) block diagram of the SDR Receiver is shown in Figure 4-3. The receiver captures a linearly polarised signal at Q-band which is down-converted to an intermediate frequency (IF) of 5 MHz, exploiting three-stage mixing. An ultra-stable 10 MHz reference oscillator is used across the three down conversion stages. The hardware is in a thermally insulated housing whose internal temperature is recorded. The signal is digitized at the 5 MHz IF frequency using a 12-bit National Instruments 5124 data acquisition (DAQ) card, which samples at a rate of 11.111 MHz.

The time-domain sampled signal is converted in the frequency domain exploiting a Fast Fourier Transform (FFT) on  $2^{20}$  time domain samples, leading to a resolution of 10.6 Hz. Then, a digital 50 KHz, 10<sup>th</sup> order Type 2 Chebyshev bandpass filter is applied to isolate



the beacon signal and the resulting spectrum is digitally resampled by a factor of 32 to reduce processing time as shown in Figure 4-3. A novel digital routine enables tracking any frequency drift of the beacon signal (nominally at 39.402 GHz) together with its peak power level [25]. Moreover, the Quinn-Fernandes Nessel (QFN) routine centres the filter accordingly. This routine is a variant of the QFN frequency estimator [26] which uses an *a priori* information window on the frequency that the beacon is expected to appear, resulting in faster detection. This allows minimisation of scalloping losses as the QFN estimator interpolates the FFT and the total power of the beacon is recorded.

A typical image of the decimated spectrum detected by the SDR receiver is shown in Figure 4-5. The received beacon power is recorded at 10 Hz and 1 Hz. These are then used in conjunction with atmospheric data provided by the European Centre for Medium-Range Weather Forecasts (ECMWF) vertical profiles and weather station data to produce a reference level such that the gaseous absorption and excess attenuation can be estimated [13]. ECMWF data are available for every six hours on a regular latitude/longitude grid with 0.125 x 0.125 spatial resolution. The ECMWF vertical profile data (temperature, humidity, pressure) are processed with the well-known mass absorption models by Liebe *et al.* [27] and Rosenkranz [28] and the total path attenuation composed from the oxygen, water vapour and cloud path attenuation are thereby obtained for the site. Identification of non-rainy periods is made from the weather station data, and in conjunction with the ECMWF data, a daily averaged reference attenuation level can be estimated. Once the reference attenuation level has been calculated for each day, it is subtracted from the power measurement time series to produce the total atmospheric attenuation (including gaseous losses). Example of calibrated time series with the above approach can be seen in Figure 4-4 and in [11], [29], [30].

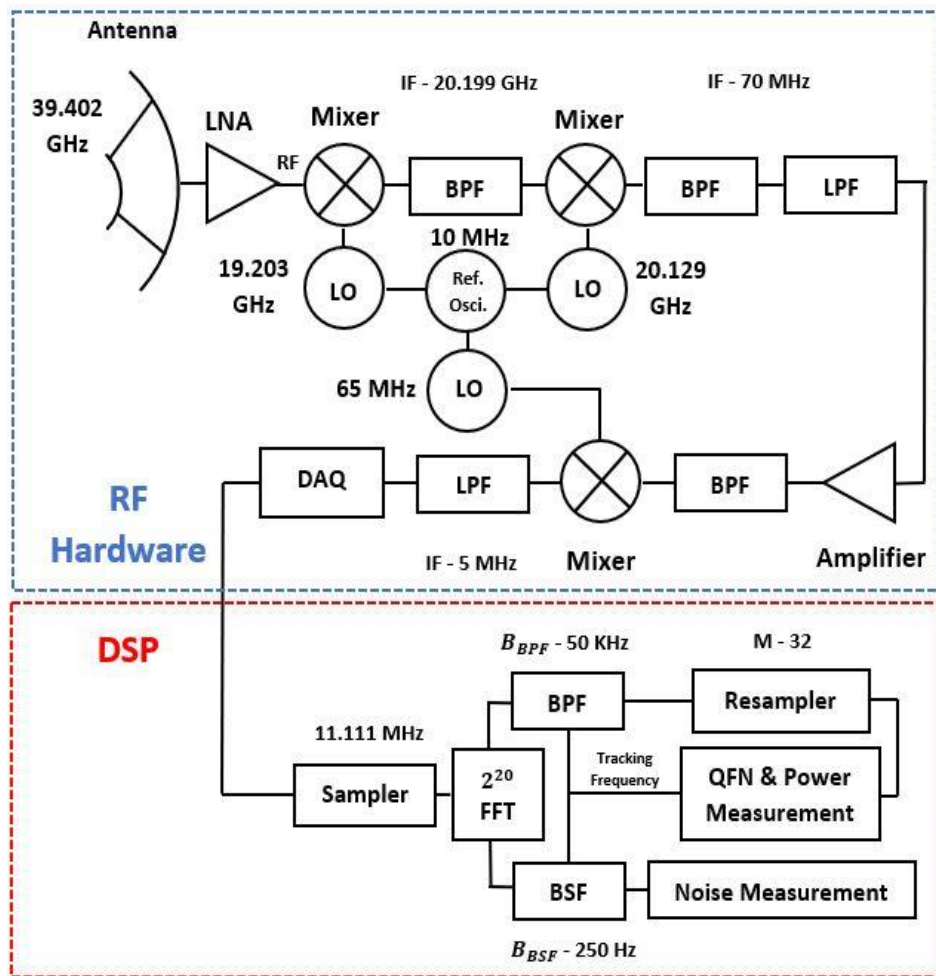


Figure 4-3: Beacon receiver RF hardware (top) and DSP (bottom) block diagram

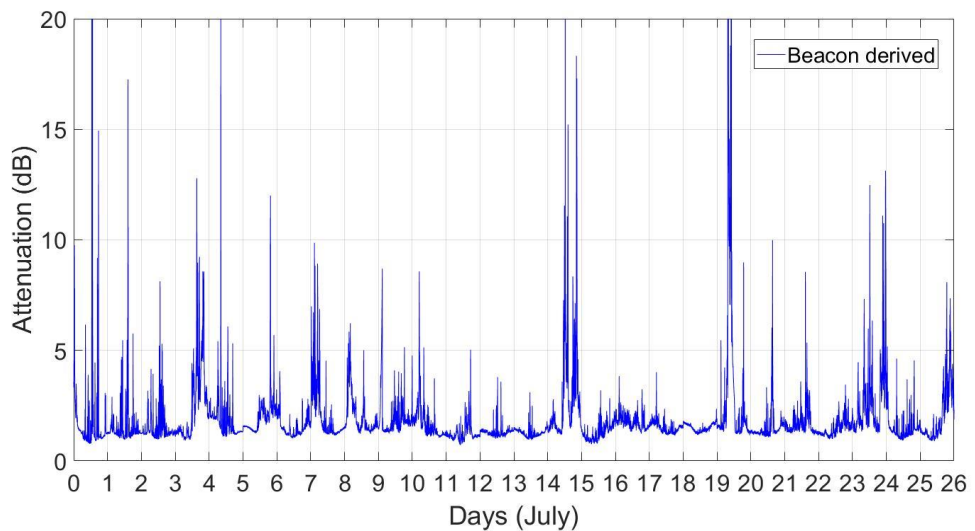


Figure 4-4: Atmospheric attenuation for July 2016.

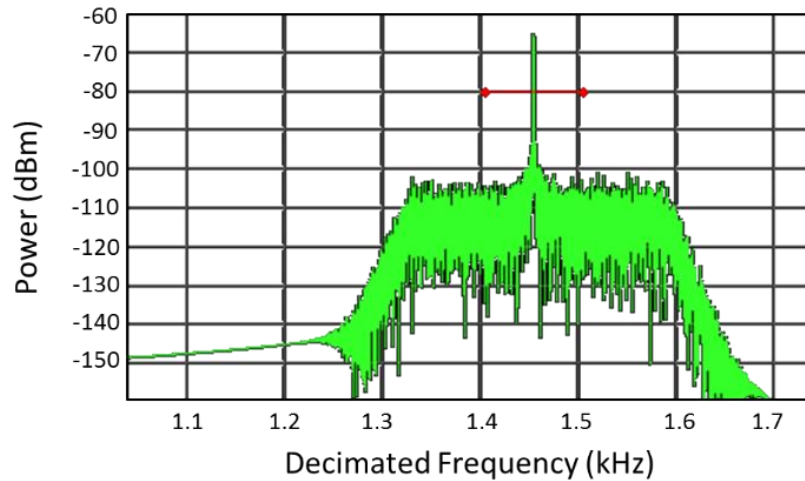


Figure 4-5: Decimated IF spectrum with beacon signal present

A digital 10<sup>th</sup> order Type 2 Chebyshev bandstop filter with a rejection bandwidth of 250 Hz is concurrently applied on the spectrum resulting from the FFT as shown in Figure 4-3. The centre of the digital bandstop filter is defined by the QFN frequency estimation of the beacon signal. This operation enables one to virtually suppress the beacon signal from the received spectrum, thus allowing the integration of the noise power measurement over the full IF bandwidth of 1 MHz. A Type 2 Chebyshev filter, unlike a Type 1, has a flat bandpass response. An instance of the bandstop filter response is plotted in Figure 4-6. It is noted that the Aldo Paraboni beacon signal is specified to have very stable phase noise and an unmodulated continuous wave signal (theoretically no bandwidth), hence the choice of the narrow bandwidth notch filter. The integrated noise power is logged with the same frequency as the beacon signal.

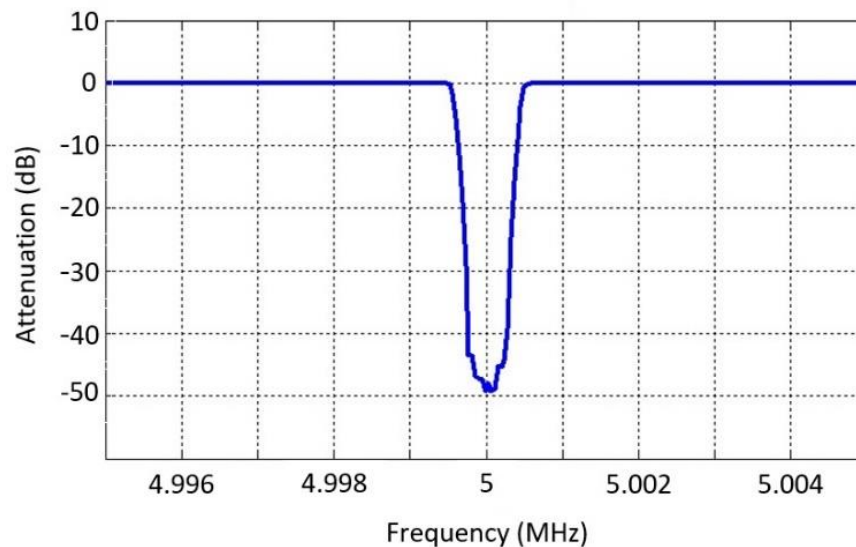
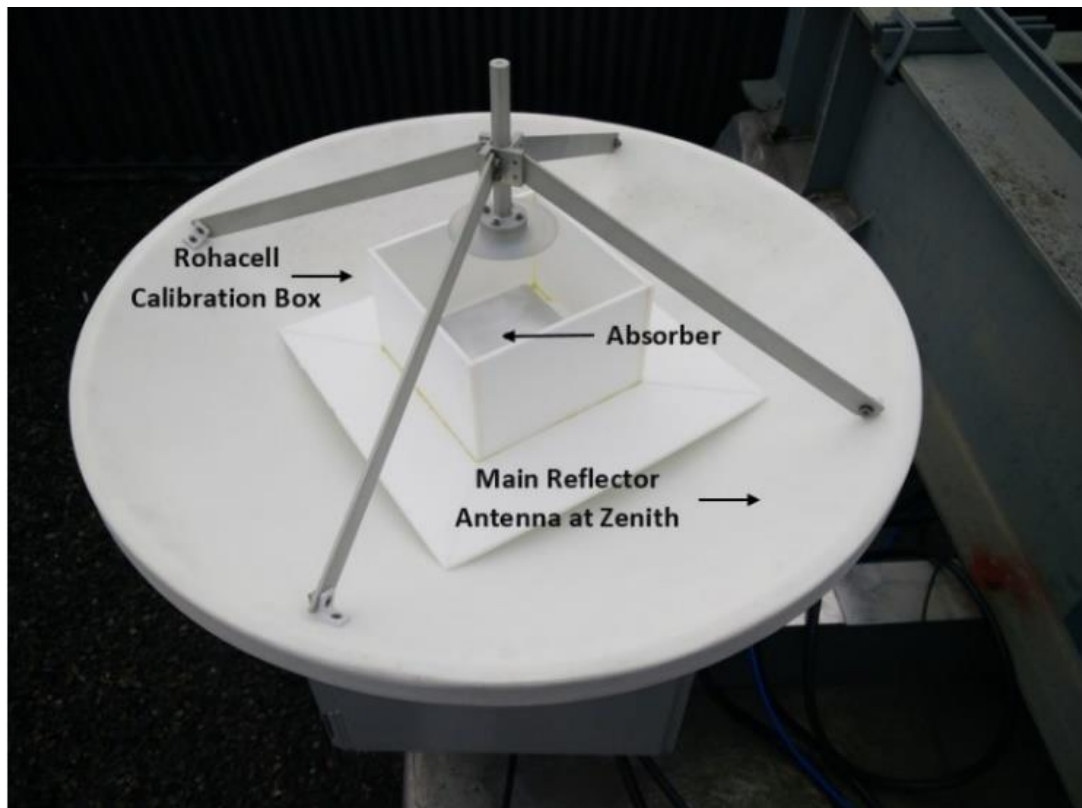


Figure 4-6: Digital notch filter response for measuring the noise power of the beacon

#### 4.4.2 Calibration

In order to convert the measured noise into attenuation, the hot-cold calibration methodology is initially applied. A radar absorbing material (RAM) with sharp 5 mm tall pyramidal and total tile dimensions of 100 ×100 mm injection moulded conductive plastic, with reflection below 45 dB at 40 GHz, was used during calibration [31]. A cuboid box was built to host the RAM absorber using Rohacell (relative dielectric permittivity of 1.05) and hence was largely RF transparent. The calibration box was of sufficient dimensions to be accommodated on the dish while the RAM absorber fully covered the antenna feed as it can be seen in Figure 4-7. Throughout the calibration, the antenna was pointed to zenith for easy access as well as providing a level plane for the calibration box to rest upon, Figure 4-7. The two temperatures that were used in the calibration are the ambient air during the procedure (hot temperature measured at 280 K) and liquid nitrogen, which has a boiling point of 77 K. The ambient air temperature during the calibration was recorded from a nearby weather station (a building south of the receiver at a distance of approximately 70 m) at one-minute intervals.



*Figure 4-7: Reflector at zenith to accommodate the calibration box during the hot-cold calibration*

In order for the absorber to first acquire the ambient (hot) temperature, it was left outdoors under the shade for an hour. The absorber was then placed at the bottom of the box and the first measurement was recorded. In order to then obtain the cold source calibration, liquid nitrogen was introduced in the host Rohacell box, Figure 4-7. During the first attempt it was not possible for the absorber to acquire the cold temperature as it started floating in the liquid nitrogen. A second attempt was made with the addition of an aluminium block on top of the absorber in order to add weight. The second attempt was successful and this can be seen in Figure 4-8 where the integrated noise power time series during the calibration process is shown. Liquid nitrogen was added twice, as the first time the liquid was boiled and evaporated within minutes due to the addition of the aluminium block.

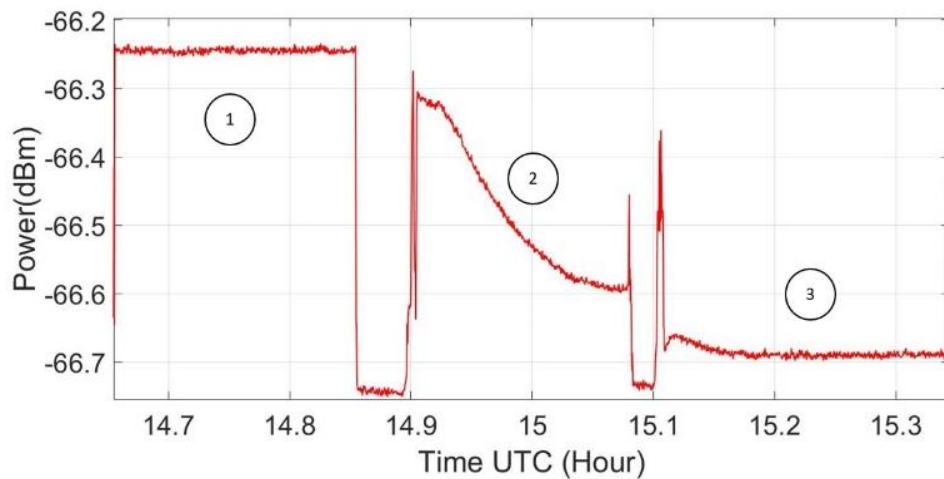


*Figure 4-8: Noise power recorded during the hot-cold calibration*

A breakdown of the different phases during the calibration are given from the numbered bullet points below. Each number corresponds to the circled numbers in Figure 4-8.

1. Noise Power with Absorber at Air Temperature
2. Noise Power with Absorber immersed in Liquid Nitrogen (Failed attempt)
3. Noise Power with Absorber immersed in Liquid Nitrogen (Successful attempt)

The absorber was covering the antenna for about 11-15 minutes during the calibration. The noise power data during the calibration was averaged for 10 minutes. These averaged measurements are plotted in Figure 4-9. From this data, the calibration coefficients,  $a$  and  $b$ , can be obtained using (4.48) & (4.49):

$$a = 8.79 \times 10^9 \text{ (KJ}^{-1}\text{Hz}^{-1}\text{)}$$

$$b = -1807 \text{ (K)}$$

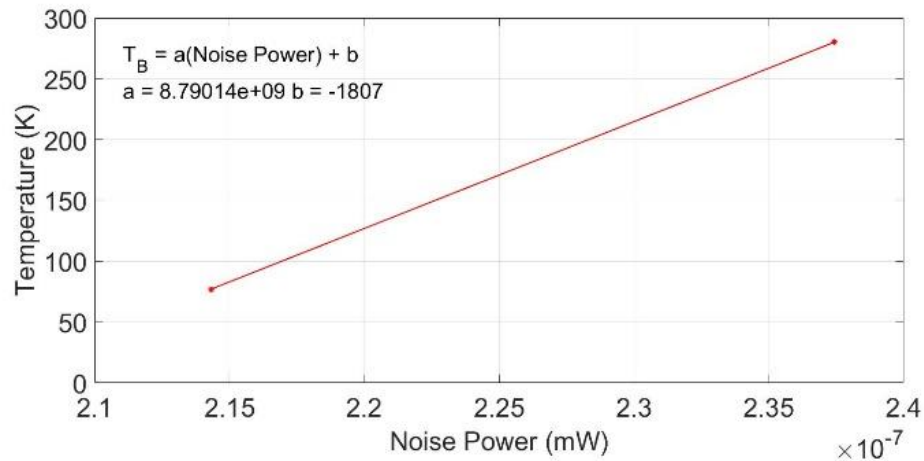


Figure 4-9: Hot-Cold calibration plot

The tip-curve calibration described in Section 5.3 was performed during a clear sky day. The receiver antenna elevation angle was tipped at elevation angles of 15°, 20°, 30°, 45°, 60° and 90° and the channel noise was recorded. The ambient temperature target measurements recorded in the hot-cold experiment were used in the first approximation of the coefficients and attenuation. Figure 4-10 shows the results of the initial and corrected calibration coefficients.  $\Delta T$  was adjusted to satisfy the assumption of no attenuation at an airmass of zero, and the corrected coefficients are obtained as:

$$a = 8.98 \times 10^9 \text{ (K J}^{-1}\text{Hz}^{-1}\text{)}$$

$$b = -1841 \text{ (K)}$$

Furthermore, receiver gain variations due to temperature can impact the accuracy of the radiometer and can be compensated by performing a temperature calibration. To combat gain variation, in the work of [32] and [33], a reference noise source was added between the antenna and low noise block via a coupler. Due to hardware limitations, such a calibration has not been performed. Nonetheless, to mitigate such errors, as mentioned in Section 5.4 the receiver is thermally insulated. Furthermore, the temperature variation of the low noise amplifier was observed to be stable with  $\pm 2^\circ\text{C}$  variations from the mean temperature.

The corrected coefficients obtained from the tip-curve calibration have been used to obtain the brightness temperature in the work described in the remainder of the chapter.

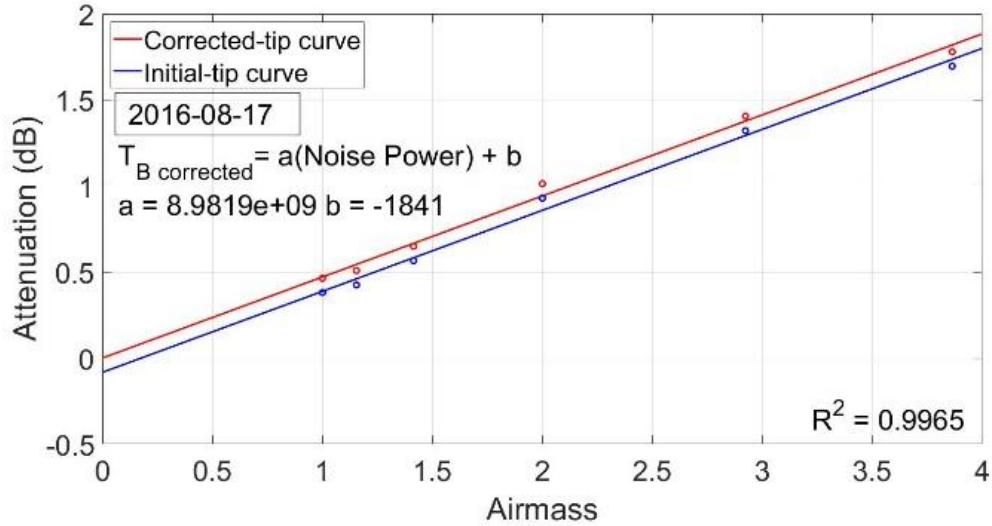


Figure 4-10: Tip curve calibration, corrected-tip and initial-tip in red and blue line respectively. Coefficient of determination ( $R^2$ ) is 0.9965

## 4.5 Experimental Results

The tip-curve calibration performed in Section 5.3 is next applied to the measurement of atmospheric fading at Q-band. In order to enable concurrent measurements from the beacon and radiometric signals, the receiver was pointed to the Alphasat satellite.

In order to confirm the efficacy of the digital filtering in suppressing beacon signal power from being injected into the integrated noise, an experiment is conducted. In particular, measurements of the integrated noise are recorded when pointing the receiver at two different positions; while pointing at the ALPHASAT and while pointing at a small angle away from the satellite during clear sky. The results are plotted in Figure 4-11, where the measurements taken at the two positions of the receiver are marked. As shown, there is a small level of additional noise (approximately 0.03 dB) recorded when the receiver points to the beacon. This increase is attributed to leakage of the beacon signal into the integrated noise.

In order to remove this contribution, the additional noise source was modelled as a temperature increase [13] as the sun's radiation in [34] was modelled as a contribution to

brightness temperature. Furthermore, considering that the temperature and power are linearly related:

$$P_N(\alpha) = P_N(\text{away}) + P_N(\text{sat})e^{-Att/4.343} \quad (5.61)$$

where,  $P_N(\alpha)$  is the noise power measurement when tracking the satellite beacon,  $P_N(\text{away})$  is the noise power measurement when pointing away from the satellite beacon,  $P_N(\text{sat})$  is the satellite signal noise contribution in the absence of atmospheric attenuation and  $Att$  is the path attenuation. The path attenuation,  $Att$ , during the measurement period was obtained from the ECMWF data. Once this bias is obtained,  $P_N(\text{sat})$ , is subtracted from the noise power measurements.

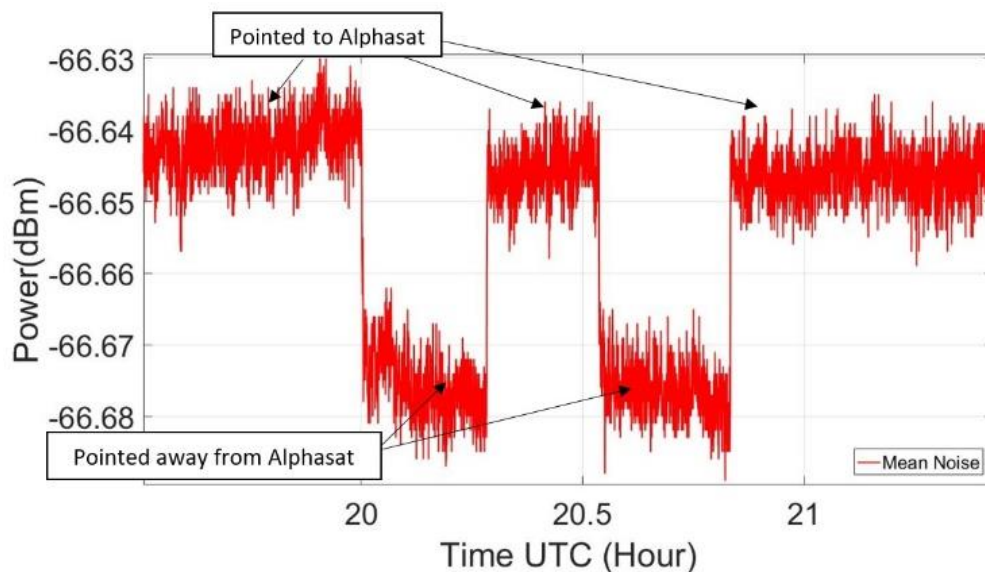


Figure 4-11: Noise power recorded when pointed towards and away from Alphasat beacon

With noise bias from the beacon removed, estimations of the brightness temperature of the sky can be calculated from the integrated noise with the method described in the previous section. To check for any gain variations caused from temperature fluctuations, the estimated brightness temperature and received beacon power were plotted during a clear sky segment, Figure 4-12. Mild temperature fluctuations during clear sky are expected to have minor changes on the estimated brightness temperature and received beacon power assuming no gain variations. The estimated brightness temperatures,  $T_B$ , mean brightness temperature,  $T_m$ , atmospheric absorption,  $A_{ab}$  and beacon signal at the different hours are reported in Table 4-1. Reported temperatures in Figure 4-12 (orange) and Table 4-1 from the nearby weather station were used to calculate  $T_m$  using (4.28).



$A_{ab}$  was calculated using (4.41). A fluctuation of  $T_B$  and therefore  $A_{ab}$  can be seen in the period between hour 4 and hour 8 in which the temperature increased by  $2.4^\circ\text{C}$ . The difference in atmospheric absorption between hour 1 and hour 5 is 0.1 dB which can also be seen at the beacon signal. This indicates that the radiometer is operating as expected with no noticeable gain variations since integrated noise power and brightness temperature decreases with an increasing received beacon power.

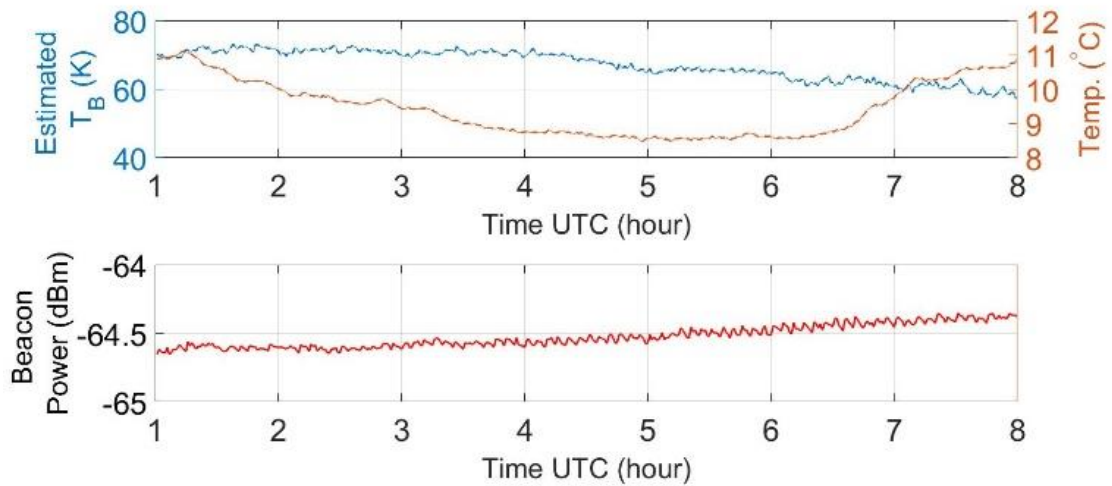


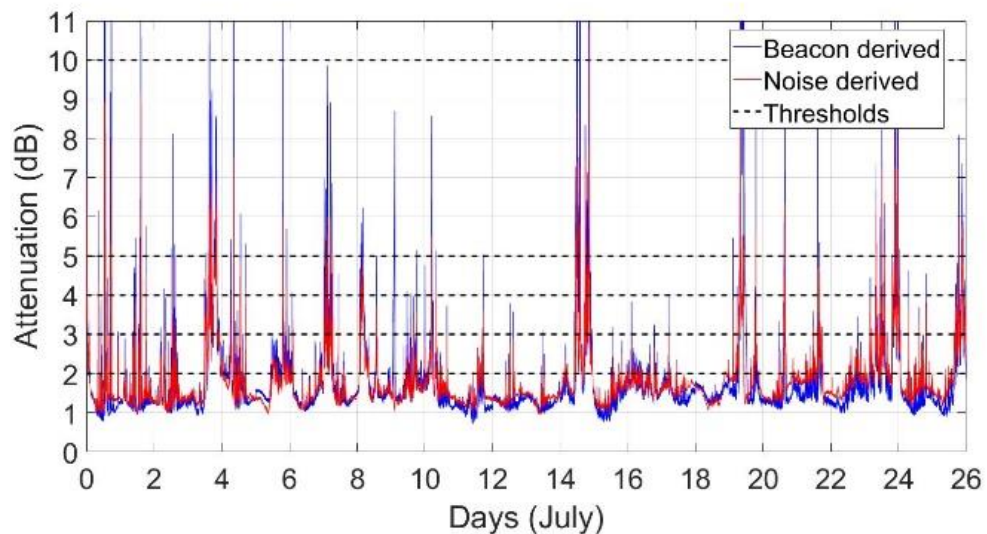
Figure 4-12: Estimated brightness temperature (blue) with temperature (orange) superimposed top and receiver beacon power (bottom) during a clear sky segment

Table 4-1: Radiometer atmospheric absorption in clear sky throughout clear sky segment

Hour	Temp ( $^\circ\text{C}$ )	$T_B$ (K)	$T_m$ (K)	$A_{ab}$ (dB)	Beacon (dBm)
1	10.9	70.19	267.42	1.278135	-64.65
2	10.0	69.71	266.69	1.271645	-64.61
3	9.42	70.05	266.22	1.2818	-64.6
4	8.74	69.52	265.67	1.273174	-64.61
5	8.55	65.26	265.52	1.180657	-64.57
6	8.62	64.40	265.57	1.161759	-64.52
7	9.75	60.68	266.49	1.077923	-64.46
8	10.91	57.82	267.43	1.013918	-64.38

The noise derived attenuation shown in Figure 4-13 (in red) for a period of 26 days in July 2016 is obtained by the method described previously. For comparison, Figure 4-13 (in blue) also plots the beacon derived fading over the same period, which for the rest of the work is assumed to be the reference fading value. It should be noted that the beacon

and noise power measurements were averaged at one-minute intervals prior to the derived attenuations. The basis of averaging the measurements was to improve the resolution of the radiometer and the accuracy of the beacon power measurements. Also, the mean radiating temperature,  $T_m$ , was calculated as described previously. Consequently, the error of the radiometric measurement is then quantified by the difference from the beacon derived measurement. A first visual inspection indicates an overall good agreement between the two curves, at least for low fading values. In order to further quantify this observation, Figure 4-14 plots the difference (in dB) between the two sets of measurements. The mean value of this curve is 0.18 dB with a standard deviation of 0.13 dB. Moreover, the cumulative distribution function (CDF) curve of this data shows values less than 1 dB, for 97.0% of the time. This indicates that the probability to obtain a radiometric measurement of the fading with error less than 1 dB is 0.97. Similar analysis indicates that the radiometric measurement can provide an accuracy in excess of 0.5 dB a probability of 0.937.



*Figure 4-13: Atmospheric attenuation for July 2016. In blue the atmospheric attenuation derived through power measurements, in red derived through the noise power measurements and in black different thresholds*

Since it is theoretically expected that the radiometric measurements would be more accurate at the low fading regime, the accuracy of the radiometric estimations is next quantified when measurements over a certain fading threshold are excluded. In particular, thresholds of fading at 10 dB, 5 dB, 4 dB, 3 dB and 2 dB are considered. The difference (in dB) between the two sets of measurements for a threshold are obtained. Any values

exceeding the set threshold are not considered. Figure 4-14 (in blue) illustrates the difference (in dB) between the radiometric and beacon derived attenuations for a threshold value of 3 dB.

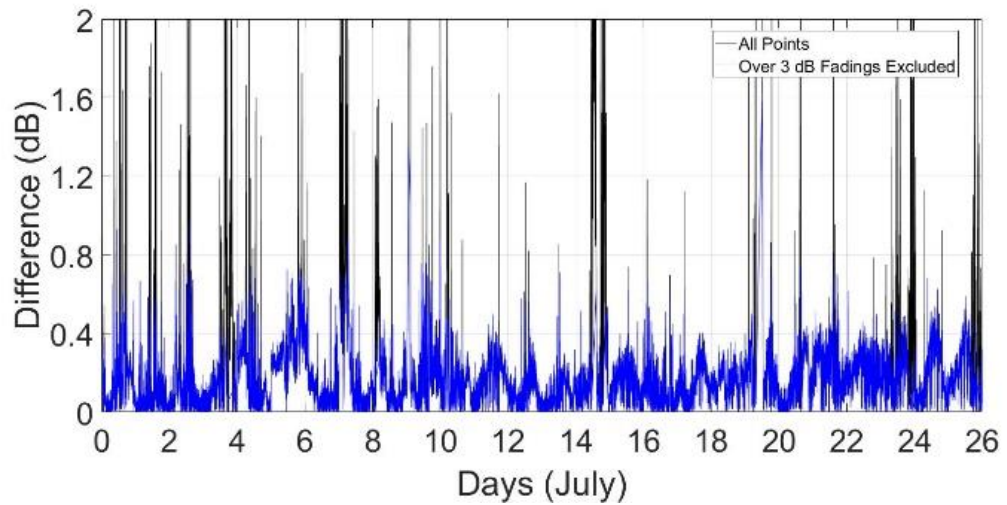


*Figure 4-14: Beacon derived and noise derived attenuation difference with all points included (black) and with over 3 dB fading excluded (blue)*

It is noted that in practice, the low fading regime is of particular interest for the operation of satellite feeder links in the Q/V-band and beyond. This is due to the limited offerings in power amplification technologies at these frequencies [35], which are likely to limit the fade margins of the gateway links compared to lower frequency bands. Indeed, in place of large fade margins, Q/V-band feeder links increasingly rely on site diversity [36] as a means to combat fading.

Consequently, a similar analysis is performed for the different threshold values. The CDF for the difference between the two sets of measurements when different threshold values are considered are plotted in Figure 4-15 (using the tip-curve derived coefficients). Table 4-2 provides some summary results indicating the probability as a percentage for the radiometric measurement to deliver valid results within error margins of 0.5 dB and 1 dB for different fading estimation ranges. As shown, when targeting to obtain fading readings up to 5 dB, the probability of the error to be below 1 dB is 0.991. This probability reduces to 0.976 when fading up to 10 dB is targeted. It is noted that although in this study the beacon derived fading is considered as a reference, in practice there is some uncertainty also with this approach. This is indicated by, for example, the standard deviation of the beacon derived fading over typical bright sky conditions being of the order of 0.25 dB. Moreover, calibration of any gain variation from the receiver would

yield improved results and strengthen the accuracy for the use of a standalone radiometer for monitoring fading.

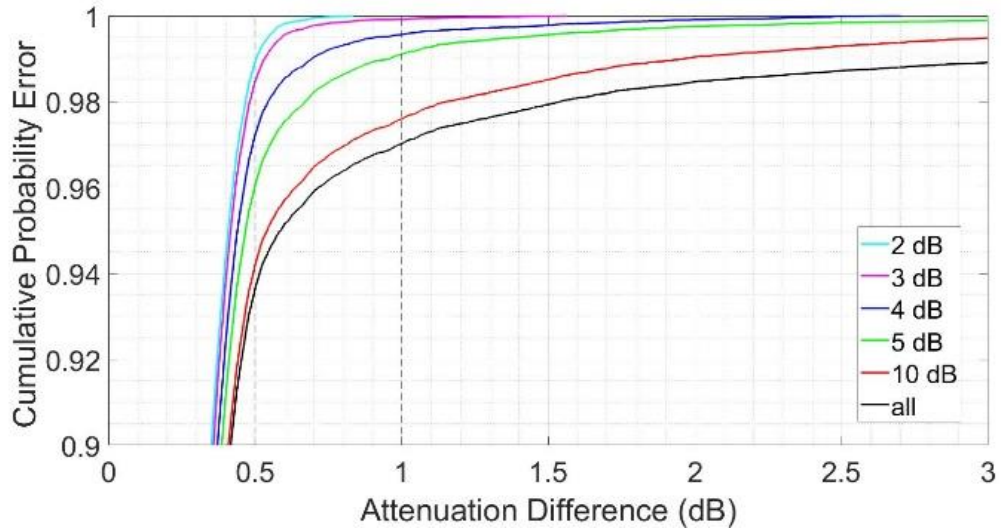


Figure 4-15: CDF of the attenuation difference between the power derived and noise derived attenuation for July 2016 including all points (black) and the shown thresholds (tip-curve calibration coefficients)

Table 4-2: The CDF of  $\leq 0.5$  dB and  $\leq 1$  dB for all points and different fading thresholds (tip-curve calibration coefficients)

Fading Thresholds	CDF	
	$\leq 0.5$ dB	$\leq 1$ dB
None	93.7%	97.0%
$\leq 10$ dB	94.2%	97.6%
$\leq 5$ dB	96.1%	99.1%
$\leq 4$ dB	97.2%	99.6%
$\leq 3$ dB	98.5%	99.9%
$\leq 2$ dB	99.0%	100.0%

The hot-cold calibration coefficients have not been used throughout the work to estimate the atmospheric fading as a tip-calibration offers lower error caused due to calibration [37]. Nevertheless, Figure 4-16 shows the CDF for the difference between the two sets of measurements when different threshold values are considered using the hot-cold calibration coefficients. Table 4-3 provides some summary results indicating the probability as a percentage for the radiometric measurement to deliver valid results within error margins of 0.5 dB and 1 dB for different fading estimation ranges. As shown, when targeting to obtain fading readings up to 5 dB, the probability of the error to be below 1 dB is 0.983. This probability reduces to 0.965 when fading up to 10 dB is targeted. In any case, excluding fading region of 2 dB and 3 dB, the probability error using the hot-cold calibration experiment increases for a range of 0.4% - 3.0%.

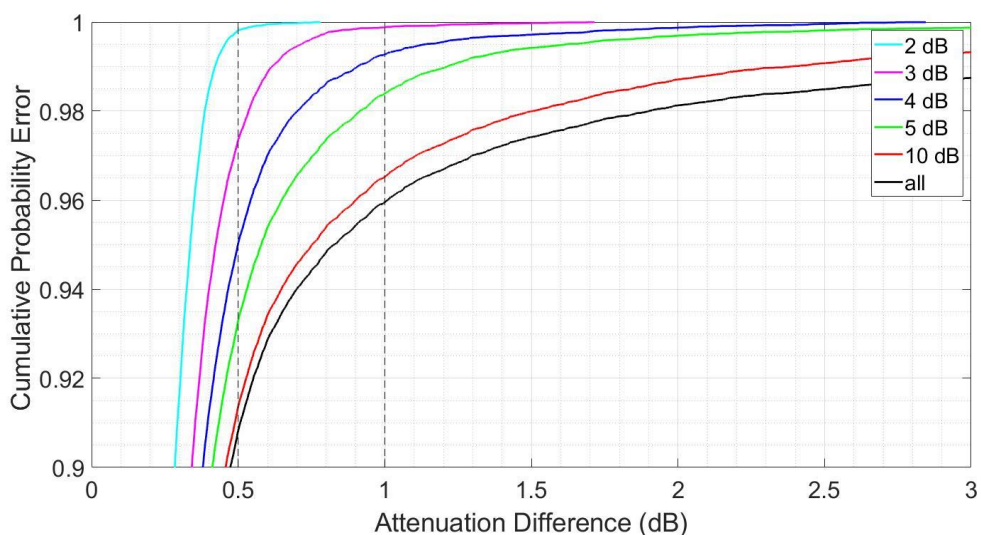


Figure 4-16: CDF of the attenuation difference between the power derived and noise derived attenuation for July 2016 including all points (black) and the shown thresholds (hot-cold calibration coefficients)

Table 4-3: The CDF of  $\leq 0.5$  dB and  $\leq 1$  dB for all points and different fading thresholds (hot-cold calibration coefficients)

Fading Thresholds	CDF	
	$\leq 0.5$ dB	$\leq 1$ dB
None	90.7%	95.9%
$\leq 10$ dB	91.3%	96.5%

$\leq 5$ dB	93.2%	98.3%
$\leq 4$ dB	94.9%	99.2%
$\leq 3$ dB	97.3%	99.9%
$\leq 2$ dB	99.8%	100.0%

## 4.6 Discussion and Conclusion

A Q-band SDR-based terminal installed at Heriot-Watt University receiving the Aldo Paraboni beacon was used to evaluate the potential of using digital noise power integration as an estimate for passive radiometry. Radiometric measurements of the atmosphere were derived from the calibrated integrated noise and the results were compared against concurrent beacon derived measurements. The beacon and radiometric derived measurements indicated a good agreement, particularly in the low fading regime. Indicatively, and assuming the beacon derived measurement as a reference, the error probability of the SDR radiometer delivering error being in excess of 1 dB for fading up to 5 dB is of the order of 1% with the tip-curve calibration coefficients. As expected, the use of the hot-cold calibration coefficients degraded the probability error by up to 3%. It should be noted that due to technology constraints future gateway systems operating in the Q/V-band and beyond are likely to operate at lower fade margins compared to existing systems up to Ka-band. According to prevailing standards [32], propagation impairment mitigation techniques (PIMT) such as adaptive coding and modulation will be deployed with a very fine granularity for the fading. Indicatively, the entire spectrum of available coding rates for 16APSK modulation extends over a signal to noise ratio of about 6 dB [33]. Consequently, these findings indicate potentially significant gains in the application of PIMT during deployment, while dispensing the need for additional costly instrumentation (e.g. a dedicated radiometer) by virtue of enabling built-in radiometric observations within the existing receiver hardware.

## References

- [1] H. Fenech, A. Tomatis, S. Amos, J. S. Merino, and V. Soumholphakdy, "An Operator's Perspective on Propagation," in *8th European Conference on Antennas and Propagation (EuCAP 2014)*, 2014, pp. 3349–3352.
- [2] A. Costouri *et al.*, "European W-Band Propagation Campaign Development," in *12th European Conference on Antennas and Propagation (EuCAP 2018)*, 2018.
- [3] M. Aloisio, P. Angeletti, F. Coromina, and R. De Gaudenzi, "Exploitation of Q/V-band for future broadband telecommunication satellites," *2012 IEEE 13th Int. Vac. Electron. Conf. IVEC 2012*, pp. 351–352, 2012, doi: 10.1109/IVEC.2012.6262191.
- [4] B. R. Arbesser-rastburg, S. Member, and A. Paraboni, "European Research on Ka-Band Slant Path Propagation," in *Proceedings of the IEEE*, 1997, vol. 85, no. 6, pp. 843–852.
- [5] S. Ventouras, S. A. Callaghan, and C. L. Wrench, "Long-term statistics of tropospheric attenuation from the Ka / U band ITALSAT satellite experiment in the United Kingdom," *Radio Sci.*, vol. 41, pp. 1–19, 2006.
- [6] A. P. A. Vernucci, L. Z. E. Colzi, A. Martellucci, E. S. A. E. Keplerlaan, and A. G. Noordwijk, "New satellite experiment in the Q/V Band for the verification of fade countermeasures based on the spatial non-uniformity of attenuation," in *2nd European Conference on Antennas and Propagation (EuCAP 2007)*, 2007, pp. 555–555.
- [7] S. Ventouras *et al.*, "Large Scale Assessment of Ka / Q Band Atmospheric Channel Across Europe with ALPHASAT TDP5 : The Augmented Network," in *11th European Conference on Antennas and Propagation (EuCAP 2017)*, 2017, pp. 1480–1484.
- [8] ESA-ESTEC, "Statement of Work: Cubesat-based w-band channel measurements," 2016.
- [9] ESA-ESTEC, "Statement of Work: Characterization of w-band propagation channel

- through groundbased observations,” 2018.
- [10] J. E. Allnut, *Satellite-to-Ground Radiowave propagation*. 2011.
- [11] J. Nessel, J. Morse, M. Zemba, C. Riva, and L. Luini, “Performance of the NASA Beacon Receiver for the Alphasat Aldo Paraboni TDP5 Propagation Experiment,” in *2015 IEEE Aerospace Conference*, 2015, pp. 1–8.
- [12] C. J. Kikkert, B. Bowthorpe, and O. J. Teong, “Improvements to a DSP Based Satellite Beacon Receiver and Radiometer,” in *Second International Conference on Information, Communications & Signal Processing*, 1999, pp. 7–10.
- [13] J. Nessel, N. Glenn, M. Zemba, and N. Glenn, “Design and Preliminary Results from Edinburgh , UK , Alphasat Q-band Propagation Terminal,” in *22nd Ka and Broadband Communications Conference, Cleveland, Ohio*, 2016.
- [14] A. Z. Papafragkakis, A. D. Panagopoulos, and S. Ventouras, “Combined beacon and noise satellite propagation measurements using software defined radio,” in *11th European Conference on Antennas and Propagation (EuCAP 2017)*, 2017, pp. 2356–2360, doi: 10.23919/EuCAP.2017.7928502.
- [15] A. Rocha, S. Mota, and F. Jorge, “Propagation campaign at Q-band and Ka-band using the Alphasat and Ka-Sat satellites,” in *12nd European Conference on Antennas and Propagation (EuCAP 2018)*, 2018, pp. 904–5.
- [16] D. G. L. Fawwaz T. Ulaby, *Microwave Radar and Radiometric Remote Sensing*. The University of Michigan Press, 2014.
- [17] A. P. L. George B. Rybicki, *Radiative Processes in Astrophysics*. 1985.
- [18] Y. Han, E. R. Westwater, and S. Member, “Analysis and Improvement of Tipping Calibration for Ground-Based Microwave Radiometers,” *IEEE Trans. Geosci. Remote Sens.*, vol. 38, no. 3, pp. 1260–1276, 2000.
- [19] P. Würfel, *Physics of Solar Cells: From Basic Principles to Advanced Concepts*, 2nd Editio. 2009.
- [20] F. Kasten and A. T. Young, “Revised optical air mass tables and approximation formula,”



- Appl. Opt.*, vol. 28, no. 22, pp. 4735–4738, 2000.
- [21] C. Mätzler, “Ground-based observations of atmospheric radiation at 5, 10, 21, 35, and 94 GHz,” *Radio Science*, vol. 27, no. 3, pp. 403–415, 1992, doi: 10.1029/91RS03052.
- [22] J. E. Allnut, *Satellite-to-Ground Radiowave Propagation*, 2nd Editio. IET, 2011.
- [23] ITU-R, “Propagation data and prediction methods required for the design of Earth-space telecommunication systems,” *Recomm. ITU-R P.618-13*, vol. 12, pp. 1–24, 2015.
- [24] D. M. Pozar, *Microwave Engineering*, Second Edi. Wiley, 1998.
- [25] M. J. Zemba, J. R. Morse, and J. A. Nessel, “Frequency estimator performance for a software-based beacon receiver,” *IEEE Antennas Propag. Soc. AP-S Int. Symp.*, pp. 1574–1575, 2014, doi: 10.1109/APS.2014.6905113.
- [26] B. G. Quinn, “A fast efficient technique for the estimation of frequency: Interpretation and generalisation,” *Biometrika*, vol. 86, no. 1, pp. 213–220, 1999, doi: 10.1093/biomet/86.1.213.
- [27] M. G. C. H. J. Liebe, G. A. Hufford, “Propagation modelling of moist air and suspended water/ice particles at frequencies below 1000GHz,” *AGARD, Atmos. Propag. Eff. Through Nat. Man-Made Obs. Visible to MM-Wave Radiat.*, pp. 08–32, 1993.
- [28] P. W. Rosenkranz, “Water Vapor Microwave Continuum Absorption: A comparison of measurements and models,” *Radio Sci.*, vol. 33, no. 4, pp. 919–928, 1998.
- [29] J. Nessel, M. Zemba, J. Morse, L. Luini, C. Riva, and A. R. Hardware, “Preliminary Statistics from the NASA Alphasat Beacon Receiver in Milan , Italy,” in *9th European Conference on Antennas and Propagation (EuCAP 2015)*, 2015, pp. 1–5.
- [30] M. Zemba, J. Nessel, C. Riva, L. Luini, and G. Goussetis, “NASA’s alphasat propagation terminals: Milan, Italy, and Edinburgh, Scotland,” *Int. J. Satell. Commun. Netw.*, vol. 37, no. 5, pp. 502–512, 2019, doi: 10.1002/sat.1296.
- [31] TK Instruments, “Space qualified Tessellating TeraHertz RAMs.” <http://www.terahertz.co.uk/tk-instruments/products/tesselatingterahertzram>.
- [32] C. J. Kikkert and O. P. Kenny, “A digital signal processing based Ka band satellite Beacon

- Receiver / Radiometer,” *2nd Int. Conf. Signal Process. Commun. Syst. ICSPCS 2008 - Proc.*, 2008, doi: 10.1109/ICSPCS.2008.4813688.
- [33] J. M. Riera, A. Benarroch, P. Garcia-Del-Pino, and J. M. Garcia-Rubia, “Simultaneous beacon and radiometer propagation measurements in the Ka-band,” in *5th European Conference on Antennas and Propagation (EuCAP 2011)*, 2011, pp. 3958–3962.
- [34] G. Brost, K. Magde, and W. Cook, “Radiometer Based Measurements of Slant-Path Attenuation in the V / W Bands,” in *13th Specialist Meeting on Microwave Radiometry and Remote Sensing of the Environment (MicroRad 2014)*, 2014, pp. 118–123.
- [35] J. Moron *et al.*, “A novel high-performance V-band GaN MMIC HPA for the QV-LIFT project,” in *24th Ka Broadband Communication Conference*, 2018, pp. 1–6.
- [36] Standard, “ETSI EN 302 307-2,” 2014.
- [37] G. Maschwitz, U. Löhnert, S. Crewell, T. Rose, and D. D. Turner, “Investigation of ground-based microwave radiometer calibration techniques at 530 hPa,” *Atmos. Meas. Tech.*, vol. 6, no. 10, pp. 2641–2658, 2013, doi: 10.5194/amt-6-2641-2013.

# Chapter 5

## 5 Conclusions and Future Work

### 5.1 Thesis Summary and Conclusions

The thesis contributions are related towards future design of Very High Throughput Satellite (VHTS) systems which will require larger bandwidths to satisfy future demand on fast and reliable broadband connections. To achieve these, along with the VHTS, gateway feeder links and user links will migrate to higher frequency bands [1]. An option would be the exploitation of the Q/V-band (40/50 GHz) but the number of required gateways may be such that the cost of the ground segment exceeds the cost of the satellite [2]. Therefore, the use of a higher band such as W-band which offers a larger bandwidth, could potentially reduce the cost of the ground segment.

With increasing frequency, satellite channels are more prone to atmospheric impairments. Therefore, in the case of exploiting W-band, propagation studies should be performed ahead of time. Previous and ongoing propagation campaigns such as the ITALSAT, OLYMPUS and Alphasat have greatly contributed toward our understanding and current ITU-R models. This has been highlighted in Chapter 1 where the current ITU-R models were reviewed, and their shortcomings reported. For instance, cloud and rain attenuation models have been modelled up to 50 GHz and would require further studies and perhaps individual campaigns to build our understanding. Further gaps that need to be filled in the ITU-R models are those on depolarisation and scintillation which are available up to 55 GHz and 20 GHz, respectively.

Another important contextual information is that of the upcoming VHTS system satellites that promise to push the boundaries in terms of throughput and availability. A number of existing and upcoming satellites able to deliver high throughputs have been mentioned in Chapter 1. An example would be the Viasat satellite family that has almost doubled its throughput since 2011 (up to 260 Gbps) and is planning on quadrupling that with the launch of their latest satellite (Viasat-3) in 2021-2022. The Q/V Lift project in Europe is currently testing Q/V-bands as feeder links for the next generation systems. ESA is also

launching campaigns (e.g. W-band CubeSat) in an effort to further improve our understanding of the propagation effects at higher frequencies.

During the last decades, the push towards higher frequency use on satellite communications has been in the agenda of both industry and research. With these premises, the development of a campaign to model propagation effects at higher frequency was imminent. These efforts are reported in Chapter 2. This was an ESA funded project in which a satellite payload was developed and designed (in software) with commercially available components for propagation studies. The geostationary payload consists of three bands at Ka-, Q- and W-band at 19 GHz, 38 GHz and 76 GHz, respectively. Several specifications including payload coverage, polarisation, output power, phase noise, mass and DC power consumption were met with satisfactory margins.

The three-band payloads were designed to have a European coverage area with an EIRP of 60 dBm for the lower bands (Ka- and Q-band) and 53 dBm for the premier W-band. These ensure a margin of at least 1 dB from the requirements. The lower band utilises linear polarisation while W-band was designed to produce circular polarisation. The phase noise mask specified was satisfied with a 10 dB margin. Furthermore, the mass and DC power consumption of the payloads were kept under 22 Kg and 100 W respectively.

Aside from the technical and engineering contributions of the design and development of the payloads, the feasibility of such a campaign was also reported. Section 2.5 reports several trade-offs and considerations on the maturity of commercially available mm-wave European technology. Moving forward with the campaign, ESA must finalise requirements such as the coverage, EIRP, polarisation switching, mass and power consumption. The section presents the several trade-offs such as the coverage, EIRP, mass, power consumption and cost as well as the availability of several components. These considerations are critical when finalising the proposed designs. Subsequently, realisation of such a campaign with a geostationary payload for propagation studies would pave the way for a deeper understanding of the atmospheric propagation impairments at higher frequencies. This would provide the opportunity to have well informed system design and fade mitigation techniques [1].

In the case of realisation of a W-band propagation campaign, ground receivers to capture the signal and study the atmospheric effects will be needed. Currently there is a large study with the Aldo Paraboni propagation payload that is experimentally characterising

the spatial and temporal atmospheric impairments across Europe [3]. This data is used for the development and testing of fade mitigation techniques. Therefore, the collection of atmospheric measurements is of great significance.

Chapter 3 reports on the design, development and implementation of a ground receiver for propagation measurements as well as the processing of data. The chapter provides a comprehensive guide on the designing of a Software Defined Radio (SDR) receiver which utilises an Ettus B200 Universal Software Radio Peripheral (USRP). The combination of these technologies has been on the rise the last few years as it is inexpensive compared to traditional analog receivers. One of the main differences is the use of digital techniques that mimic hardware components. Furthermore, fast computing and advanced analog-to-digital converters allow sampling the received signal at a higher frequency. This reduces the down-conversion complexity and cost. Consequently, cost is not a limiting factor in participating in a propagation campaign.

The custom designed receiver is tracking the Aldo Paraboni payload and is currently at the lowest elevation angle receiver in Europe. Fading and atmospheric impairments at a lower elevation angle are more severe and therefore it is important to collect the data. The receiver demonstrated a measured carrier to noise ratio of 35 dB and can therefore track deep atmospheric fading. Moreover, the operation is validated and directly compared to an expensive analog-to-digital converted from National Instruments. The results are more than encouraging towards the use of this new technology (USRPs and SDRs) as it can offer an additional inexpensive alternative. A methodology to obtain the excess atmospheric fading from the recorded timeseries of the receiver was also demonstrated. The designed receiver operates at Ka-band but, the know-how acquired can be applied for implementing a receiver at W-band.

The study of the atmospheric absorption and fading due to absorption of a channel has been traditionally done with radiometry [4]. Radiometers are able to measure the sky noise (brightness temperature) and translate that to atmospheric fading due to absorption. Essentially, radiometry could be used to monitor the sky and act as an input to fade mitigation techniques. Chapter 5 presents the theory on atmospheric radiometry followed by the implementation of a digital radiometry at Q-band with the use of SDR. The reported findings are also validated; which was lacking from previous work around the topic. With the use of digital receivers through SDR, several researchers showed the possibilities of converting conventional receivers to digital radiometers but none has

qualitatively validated the findings. The chapter explores different calibration methodologies (hot-cold and tip-curve calibration) and reports on the validity and accuracy by comparing the recorded data with that from a propagation beacon.

It is noted that the error probability of the SDR radiometer delivered an error less than 1 dB for fading up to 5 dB of the order of 1%. Consequently, these findings reflect potentially significant gains in the application of fade mitigation techniques during deployment, while dispensing with the need for additional costly instrumentation (e.g. a dedicated radiometer) by virtue of enabling built-in radiometric observations within the existing receiver hardware.

## 5.2 Future Work

The topics discussed in the thesis have possible future work and are listed below:

- In Chapter 2, the proposed three-frequency propagation payload with the premier W-band has a few trade-offs that in the future should be considered ahead of the final development. These include the beacon coverage, since as of now it only covers Europe with the possibility to cover the tropics. The margins of the payloads can be relaxed to accommodate a change in coverages. Furthermore, certain components need to be packaged while others need to be designed, manufactured and tested ahead of the campaign. This includes components such as the filters, antennas and redundancy switches.
- In Chapter 3, the Ka-band receiver is quite new in terms of propagation studies. It has been operating for just over a year and the data collected need constant monitoring. In the future, excess attenuation for a year could be produced. This can provide a useful statistic on the atmospheric fading and duration throughout a year. Due to time limit constraints, this was not possible. Furthermore, the noise measurements could be calibrated in an effort to implement digital radiometry and monitor the sky. Such a (radiometry) terminal could be mounted on a separate tracker that monitors the sky adjacent to the gateway's channel path. Realtime information on the condition of the sky could feed as an input to a gateway switching scheme.

- In Chapter 4, the fading timeseries that have been shown could potentially be used to do link level characterisation for a Q-band channel. SDR and USRPs can be used as the digital signal processing tool and RF hardware respectively. A voltage-controlled attenuator can act as the channel fading in real-time. To simulate a satellite channel, the baseband signal standard for satellites, DVB-S2 can be used. It offers a number of coding and modulation schemes for different atmospheric scenarios. Adaptive coding and modulation according to the fading can be studied to maximise the channel throughput.

## References

- [1] A. Costouri *et al.*, “European W-Band Propagation Campaign Development,” in *in 12th European Conference on Antennas and Propagation (EuCAP 2018)*, 2018.
- [2] H. Fenech, S. A. A. Hirsch, and V. Soumpholphakdy, “VHTS Systems : Requirements and Evolution,” pp. 2409–2412, 2017.
- [3] S. Ventouras *et al.*, “Assessment of spatial and temporal properties of Ka/Q band earth-space radio channel across Europe using Alphasat Aldo Paraboni payload,” *Int. J. Satell. Commun. Netw.*, vol. 37, no. 5, pp. 477–501, 2019.
- [4] A. Costouri, J. Nessel, and G. Goussetis, “Validation of a Digital Noise Power Integration Technique for Radiometric Clear Sky Attenuation Estimation at Q-Band,” *Trans. Antennas Propag.*, pp. 1–9.